Czech Technical University in Prague

Faculty of Biomedical Engineering

Doctoral Thesis

November 2023

Ing. Kateřina Žambochová

Czech Technical University in Prague

Faculty of Biomedical Engineering
Department of Natural Sciences

Interaction of fluorescent nanodiamonds with cells investigated by interferometric scattering microscopy techniques

Doctoral Thesis

Ing. Kateřina Žambochová

Kladno, November 2023

Ph.D. Programme: *Biomedical and Clinical technology*

Supervisor: ***Ing. Dalibor Pánek, Ph.D.***

This work was conducted in a full-time Ph.D. study at the Department of Natural Sciences of Faculty of Biomedical Engineering of Czech technical University in Prague together with Center for Molecular Spectroscopy and Dynamics of Institute for Basic science of Korea University.

Candidate: Ing. Kateřina Žambochová
Faculty of Biomedical Engineering, CTU in Prague
nám. Sítná 3105, 272 01 Kladno, Czech Republic

Supervisor: Ing. Dalibor Pánek, Ph.D.
Faculty of Biomedical Engineering, CTU in Prague
nám. Sítná 3105, 272 01 Kladno, Czech Republic

Abstract

Single nanoparticle imaging, moreover, its quantitative characterisation or tracking have always been a challenge especially when using optical methods. Here, a fluorescence combined interferometric scattering (iSCAT) method in combination with theoretical modelling and data processing accomplishes all those challenges and offers a close insight into nanoparticle-cell interaction. In this work, iSCAT is used for size quantification of dielectric nanoparticles in range from 100 nm down to 10 nm. Although it is a fully optical method, the interferometric aspect allows to go beyond the diffraction limit. An axial three-dimensional profile of interferometric scattering from a single particle contains information about nanoparticle's exact location, its material properties or size. A theoretical model was then developed to unravel the detected scattering signal from a single particle to calculate its size. The size measurement was carried out with polystyrene beads and subsequently fluorescent nanodiamonds (fND). Characterized fNDs were used in further investigation of their interaction with living cells. This investigation uncovered different pathways of 10 nm and 100 nm fNDs during the uptake mechanism as well as their pathway inside the cell. A single particle tracking method with fluorescence combined iSCAT was developed along the way which allows to track even as small nanoparticles as 10 nm in long timescales up to several hours. Both introduced methods are versatile techniques offering future development and perspective in nanoparticle characterisation and optical bioimaging.

Abstrakt

Zobrazování jednotlivých nanočástic natož jejich kvantitativní charakterizace a trasování byly vždy výzvou především v optických zobrazovacích metodách. Zde prezentovaná interferometrická rozptylová mikroskopie (iSCAT) kombinovaná s fluorescenční detekcí a s využitím teoretického modelování a zpracování dat splňuje všechny tyto výzvy a nabízí bližší pohled na interakci mezi nanočásticemi a živými buňkami. V této práci je iSCAT použit pro kvantifikaci velikosti dielektrických nanočástic v rozsahu od 100 nm do 10 nm. Přestože se jedná o plně optickou metodu, interferometrie v tomto případě umožňuje překročit difrakční limit. Axiální trojrozměrný profil jedné částice detekován touto interferometrickou technikou obsahuje informace o přesné poloze nanočástice, jejích materiálových vlastnostech a velikosti. Teoretický model byl následně vyvinut pro rozluštění detekovaného rozptylového signálu z jedné částice za účelem výpočtu její velikosti. Měření velikosti bylo provedeno s polystyrenovými kuličkami a následně fluorescenčními nanodiamanty (fND). Charakterizované fND byly použity při dalším zkoumání jejich interakce s živými buňkami. To odhalilo různé mechanismy endocytózy a chování uvnitř buňky pro 10 nm a 100 nm fND. Zároveň s tím byla vyvinuta metoda pro trasování jednotlivých částic pomocí iSCAT mikroskopie kombinované s fluorescenční detekcí, která umožňuje sledovat i tak malé nanočástice jako 10 nm v dlouhých časových intervalech až několika hodin. Obě představené metody jsou všestranné techniky perspektivní v charakterizaci nanočástic a optickém biozobrazování a vybízejí k budoucímu vývoji.

Declaration

I declare that this thesis has been composed solely by myself and that it has not been submitted, in whole or in part, in any previous application for a degree. Except where states otherwise by reference or acknowledgment, the work presented is entirely my own.

Acknowledgements

I could not have undertaken this journey without my supervisor Ing. Dalibor Pánek, Ph.D. . I would like to thank him for his guidance, inspiring ideas and feedback that made this possible. I would also like to express my appreciation to doc. RNDr. Vlastimil Fidler, CSc. for his kind help and support with my research abroad. My deepest gratitude goes to prof. Minheang Cho who provided me the opportunity to work with his excellent team and offered many valuable advice and lessons. I would like to extend my sincere thanks to prof. Seok-Cheol Hong, Il-Buem Lee and Jin-Sung Park for their most appreciated help and assistance and provided knowledge and expertise.

My special thanks go to my fellow researchers and friends Tomáš Parkman, Lucie Dubovská and Dorota Kossowska for their never ending moral and emotional support and keeping my spirit high throughout the years.

Lastly, I am grateful for my family who provided a safe environment for me to be able to do this work and whose belief in me kept me motivated during this process.

This work was financially supported by Czech Technical University foundation SGS17/201/OHK4/3T/17 and the Institute for Basic Science IBS-R023-D1. It was also partially supported by an NRF grant 2022R1A2B5B01002343 and the Global Research and Development Center Program 2018K1A4A3A01064272 through the NRF of Korea (S.-C.H.).

Table of Contents

1 Introduction

Starting from observing the stars by telescopes to imaging small structures by optical microscopes, diffraction has always been in question. There was a time when diffraction was thought to be the ultimate limiting factor to the spatial resolution of light microscopes. The first diffraction image was calculated by George Biddell Airy in 1835[1]. It was an image of a star as a point source seen by circular aperture of a telescope. The first clear mention about diffraction limitation of optical systems came much later from Émile Verdet in 1869 who based his theory on telescope viewing angle ω and came to a conclusion that $1/(2\omega)$ is the limitation to optical imaging. However, the most widely known work discussing the limiting role of diffraction was published by Ernst Abbe in 1873[2]. It clearly stated his theory that the optical resolution would always be limited by half-wavelength of blue light. Nevertheless, he admits that there might be way for improvement beyond those limits.

Independently on Abbe's work, Hermann von Helmholtz published his work on the same topic and matching results just one year later. In addition to Abbe's work, Helmholtz supported this theory with mathematical proofs. Another significant contribution to the topic came from Lord Rayleigh[3] who expanded the theory to various shapes of the objects and apertures. He is the author of well-known Rayleigh criterion[4] for the minimum resolvable detail given by zero distance between the first intensity minimum of one diffraction pattern and first intensity maximum of another.

The effort to surpass this diffraction limit led to development of new methods. One of the first methods with enhanced resolution but not yet transcending the diffraction limit were scanning near field optical microscopy (SNOM) using high spatial frequencies to image fine details, total internal reflection (TIRF) imaging with help of evanescent light field near cover slip to image thin layer of sample with suppressed background, confocal microscopy where a pinhole enables axial sectioning and increases lateral resolution, or methods using structured illumination[5].

Diffraction limit was finally exceeded by use of fluorescent methods. Stimulated emission depletion (STED) microscopy developed by Hell and Wichmann[6] is able to minimize a size of a fluorescent point under diffraction limit by selective depletion of fluorescence in the area while keeping the central point active. Another such technique is RESOLFT (reversibly saturable/switchable optical fluorescence transitions) microscopy

first introduced by Hell and Kroug[7]. RESOLFT uses switchable fluorescence molecules similarly to STED and inhomogeneous illumination. The resolution of those techniques can go down to less than 10 nm[8], [9]. This concept of switchable optical states was later used in other techniques like DSOM (dynamic saturation optical microscopy)[10], PALM (photoactivation localization microscopy)[11], FPALM (fluorescence photoactivation localization microscopy)[12] or STORM (stochastic optical reconstruction microscopy)[13], [14].

Optical techniques have always been popular to use in biological applications. All those enhancements gradually led to better resolution, three-dimensional (3D) imaging, multi-colour imaging and distinguishing different parts of organisms, tissues and cells[15]. It became widely used in microbiology, biotechnology, nanoscience, pharmaceutical or medical research. One of the most relevant topics these days is interaction of nanomaterials and biological systems. Nanomaterials already have a broad usage in industry and everyday products. In biomedicine, especially nanoparticles could be used for drug or contrast agent delivery into cells or as optical probes. However, this kind of biomedical applications is mostly still in the phase of research. The mechanism of interaction of nanomaterial with biological system is different from bulk material and it can show unexpected results as nano-dimension brings new properties to the material. Specific properties of nanomaterials can generate a specific response of biological system starting with interaction of nanoparticle with biomembrane and further behaviour inside the cell. The size, shape, surface characteristic and functionalisation of nanoparticle or characteristic of the environment may play a significant role in nanoparticle and cell interaction.

Knowledge of interaction between nanoparticles and cell structures is important regarding to new applications of nanomaterials, *e.g.*, imaging in living systems, biosensors, drugs delivery or toxicity analysis.[16] However, imaging in living systems has always been a challenge, especially imaging and tracking cells in vivo. For those purposes a suitable combination of biocompatible label and imaging techniques needs to be decided on. In this work, fluorescent nanodiamonds (fNDs) were selected as a suitable candidate for bioimaging purposes due to their biocompatible and inert nature, bright fluorescence, photostability and high refractive index. Considering those properties, a combination of interference scattering (iSCAT) microscopy, a relatively new and very promising technique, with fluorescence detection can enable unambiguous label free imaging of cell structures and long-term tracking of nanoparticles in real time.

The iSCAT characteristics such as high sensitivity, homodyne detection and unlimited observation time[17]–[19] are desired features for bioimaging or nanoparticle characterisation applications. In this work, both nanoparticle characterisation and subsequently fND interaction with living cells are successfully explored by iSCAT.

Under certain set of conditions, the iSCAT signal from a nanoparticle is proportional to the volume of the particle[20], [21] which was proven for example for metallic nanoparticles[22] or proteins.[20], [21] Here, a new approach to nanoparticle size evaluation is reported. This approach aims to be more universal, highly sensitive and accurate and consider all possible factors for wider variety of nanoparticles and iSCAT setups. The presented method considers material properties of the scatterers and all other involved materials, illumination and optical setup properties and optical aberrations that all contribute to the iSCAT signal. Besides, it is not limited by only Rayleigh scattering and goes beyond its limit where the scattering becomes asymmetric.[23]

Because small scatterers far below the Abbe diffraction limit are used, it is not possible to obtain images of the actual shape of a nanoparticle. Thus, the method is based on determining of the vertical position of the scattering dipole of a nanoparticle placed on the cover glass calculated by rigorous theoretical model. It is demonstrated that the height of this dipole quantitatively correlates with the radius of its source.

The size measurement method is based on theoretical model and optical imaging of single nanoparticle. Similar models were presented for different purposes too, for example, to localize metallic nanoparticles,[24] to study metallic nanoparticles by photothermal microscopy[25], [26] or to study different scattering properties between dielectric and metallic nanoparticles.[27] The difference here is, that none of them adapted these theoretical models for quantitative measurement of nanoparticle size as presented in this work.[23]

After successfully characterizing fNDs with iSCAT, it was used for single particle tracking (SPT) in living cells and uncovering new findings in SPT and fND-cell interaction. Here, the combination of iSCAT with fluorescence detection came in handy when localizing even the smallest (10 nm) fNDs which opened door to unique observation of such small nanoparticle's fate inside the cell. The long-term tracking feature of iSCAT in real time enable to record short- and long-time scale events during fND-cell interaction and offered deeper insight into SPT and its data analysis. The internalization rate of bare and coated fNDs was studied. Then, the events before and after internalization were

recorded showing distinct differences in fND behaviour of different sizes or functionalization.

A SPT method using fluorescence combined iSCAT for long-term observation of nanoparticles in living cells was developed including data processing and evaluation. This method is intended for wider and further use in studying living cells by iSCAT.

1.1 Aims of the thesis

The main goal of the thesis was to develop a rigorous technique for characterization of fluorescent nanodiamonds and studying their interaction with living cells.

The partial objectives to achieve this goal were:

1. *Construction of fluorescence combined iSCAT microscope*
   To upgrade an iSCAT microscopy setup with fluorescence detection and set it for simultaneous detection of fND by both fluorescence and iSCAT channels.
2. *Development of theoretical model for nanoparticle characterization*
   To write a theoretical model in MATLAB that will detect, localize and characterize nanoparticle size by iSCAT microscopy and to prove the functionality and accuracy of the model on measured data.
3. *Establishing a method for single particle tracking in living cells by iSCAT*
   To update the iSCAT setup for long-term measurement of living cells, establish the recording conditions and suitable timescales for capturing various events of fND and cell interaction and write a MATLAB script for data processing.
4. *Studying endocytosis of fNDs and their fate in the cell*
   To record and analyse different stages of fND interaction with living nonphagocytic cells with different sizes or functionalization of fNDs.

1.2 Organization of the thesis

This thesis describes a process of development of a method for nanoparticle characterization and single particle tracking in living system using iSCAT microscopy as an imaging technique and presents new findings about fND-cell interaction obtained thanks to that method.

First, the theoretical section (Chapter 2) introduces all the fundamental methods used, sets them in context of this work and their state of art and describes the principles in order

to understand the later results. The methods include super-resolution microscopy techniques (2.1) of which the interferometry-based microscopies are highlighted, iSCAT microscopy (2.2) and diffraction theory (2.3), single particle tracking SPT (2.4) and finally interaction of nanoparticles (2.5) and specifically fNDs (2.6) with cells, in the same order as the practical part was conducted and results are presented.

Chapter 3 describes the iSCAT experimental setup in detail and gives closer information on the used materials, i.e., fND samples (3.2) and sample preparation for cellular experiments (3.3).

The results are divided into two main chapters, the iSCAT microscopy for nanoparticle size characterization (Chapter 4) introducing the developed theoretical model (4.2) showcasing the model on measured data of reference particles (4.3) and fNDs (4.4) by iSCAT. And imaging fNDs in cells (Chapter 5) including the tracking software development (5.5) and interaction of fNDs with U2OS cells (5.6 - 5.7).

The final Chapter 6 summarizes the results and evaluates the accomplishment of the thesis aims.

2 State of art and theoretical background

This chapter covers the basic principles that interconnect throughout this work.

2.1 Resolution in optical microscopy

The fundaments of microscopy are to capture and visualize objects and events in small scales. From imaging cells to single molecules, each microscopic method has its own advantages and limitations. In case of light microscopy, we use visible light (380 nm – 700 nm) as a source. The relatively non-invasive nature and easy accessibility and handling of visible light source makes light microscopy a very attractive method of imaging. Still, the resolution limit and sensitivity achievable by visible light were the main obstacles until recently.

2.1.1 Resolution and sensitivity

The challenge to visualize small scale structures comes down to dealing with resolution, sensitivity and specificity.[28] In this work, we are mostly dealing with (a) sensitivity and (b) resolution.

(a) The main challenge is to reach shot noise sensitivity and the best precision which depends on detecting a weak signal and distinguishing it from the imaging background or noise.[28], [29] Sensitivity can be understood as signal to noise ratio

$$SNR = \frac{P_{signal}}{P_{noise}} , \quad (1)$$

where P is a power of a signal, or as a contrast

$$I_{contr} = \frac{P_{max} - P_{min}}{P_{max} + P_{min}} . \quad (2)$$

There were several ways used to supress the background signal in the past, i.e., placing the observed object in vacuum,[30] using frequency modulation spectroscopy and measuring absorption spectra at cryogenic conditions,[31] or the most widespread approach by using fluorescence. Another purely optical approach with high contrast is dark-field microscopy[32] which detects scattered light from a transparent specimen that results in higher contrast between areas with different refractive index in the final image. It can be often used instead of fluorescence microscopy resulting in comparable image quality.[33] Nevertheless, imaging single molecules with dark-field microscopy proves still more challenging than using fluorescent dyes due to difficulty of separating weak scattering signals of single molecule from the background signal.[28]

Until this day there are two main methods how to reach shot noise sensitivity (i) eliminating image noise coming from illumination fluctuations by combining speckle-free laser with widefield detection[34] and (ii) subtracting background by image postprocessing.

(b) The resolution of optical microscopy is in principle given by the diffraction limit of visible light.[35] Abbe diffraction limit is defined as [35]

$$d = \frac{\lambda}{2n \sin\theta} = \frac{\lambda}{2NA} \quad , \tag{3}$$

where λ is wavelength, n refractive index of the medium where the light travels, θ is half-angle of the light cone entering the lens and NA is the numerical aperture of the lens. As for optical microscopy, this limit can be improved by applying interferometric or fluorescence techniques.

2.1.2 Interference-based microscopy

The first type of microscope using interference phenomenon was phase-contrast microscope[36] where the phase shift originates in the transparent sample while the light passes through and then the transmitted light is detected. Later, the differential interference contrast (DIC) microscopy was invented[37], [38] that uses two slightly displaced light beams that travel alongside each other through transparent sample to image areas with different refractive indexes. Although, the image quality of these

approaches was lower compared to dark-field imaging at the time, further development of illumination and detection techniques sustained these methods till this day mainly as label free cellular imaging techniques.[39], [40]

Reflection based schemes proved to be more eligible for the detection of small structures. In reflection scheme of interference microscopy, only small portion of incident light is reflected back and interferes with the back-scattered light from the sample. Because most of the incident light passes through the sample but the scattering from subdiffraction limit structures is the same in both directions, we obtain more signal from the sample compared to the reference in the back scattered/reflected direction of detection.

There have been several implementations of the reflection based interferometric microscopy, nonetheless, the principle is the same. The sample is placed on the transparent substrate, e.g. cover glass, the incident beam is then partially scattered at the sample, partially reflected at the interface between sample and substrate and the rest of the light is transmitted. The back-scattered and reflected signals are then collected with the same objective lens used for illumination. The detected intensity I_{det} is given by

$$I_{det} = |E_r + E_s|^2 = |E_{inc}|^2(|r|^2 + |s|^2 + 2|r||s|cos\phi) \ , \qquad (4)$$

where E_r is the reference field reflected from the cover glass, E_s is the scattered field from the sample, E_{inc} is the incident filed, r is the field reflectivity and $s = |s|e^{i\phi}$ is the scattering amplitude with relative phase ϕ between reflected and scattered fields.

2.2 Interferometric scattering microscopy (iSCAT)

2.2.1 State of art in iSCAT microscopy

The phenomena of interference or scattering are central principles of some already well-known microscopic techniques like differential interference contrast, phase-contrast or dark-field microscopy. The reflection interference microscopy also called reflection contrast microscopy[41]–[45] can be considered as the first precursor of iSCAT microscopy. Reflection interference microscopy was initially used for quantitative measurements on cells,[41], [46], [47] lipid bilayers[48] or phospholipid vesicles.[49] Later, coherent light source was used which significantly enhanced the contrast.[50] Interferometric scattering techniques then reached sensitivity to image particles of diameter down to 5 nm as demonstrated for gold nanoparticles[51] and been able to track

single virions without any labeling.[52] The first report that used the term interferometric scattering (iSCAT) microscopy in 2009 also introduced imaging background removal method which was a significant improvement in sensitivity and precision of the method.[53]

For a long time iSCAT technique was used mainly for single particle tracking (SPT) due to its sensitivity, nanometre precision and label-free approach. First successful attempts for SPT were carried out in background-free, well-controlled, model synthetic systems like tracking virus particle[53] or gold nanoparticles (GNP)[54], [55] on supported lipid bilayers, lipids and proteins on giant unilamellar vesicles[56] or just detecting and imaging single proteins,[20], [57], [58] GNP,[59] microtubules and actin filaments in clear substrate[57], [60] and tracking metallic nanoparticles attached to motor proteins on the filaments.[60]–[62] Imaging and tracking nanoparticles in living cells is significantly more challenging due background coming from the complicated cell structures. First SPTs performed on living cells studied diffusion of intracellular vesicles[63] and membrane proteins labelled with GNPs.[62], [64] Other studies took interest in distinguishing and imaging inner cell structures like cytoplasmic organelles[65] or focal adhesions[66] since iSCAT microscopy enables label-free live cell imaging in real time with no need of staining or fixation.

In principle, the iSCAT imaging is sensitive to the difference in optical properties within the sample and any change in those properties, *e.g.*, refractive index, can be ideally detected and quantified.[28] Mass photometry[20], [21] well demonstrates the quantification of protein mass from its iSCAT contrast. Recently, the potential of nanoparticle volume quantification was expanded, and it was demonstrated that it is possible to measure volume of nanoparticles made of different materials with nanometre accuracy in a range of sizes from tens to hundreds of nanometres by iSCAT.[23]

Recently, different modalities of iSCAT microscope were introduced: Fluorescence combined iSCAT microscope that utilizes the advantages of both fluorescence and iSCAT detection,[18], [23], [66] Polarization-selective iSCAT microscopy for imaging orientation of non-spherical nanoparticles,[67] Remote focusing for 3D imaging in iSCAT microscopy[17] and resonant scattering enhanced iSCAT microscopy for resonant sensing and possible development of iSCAT spectroscopy.[68]

2.2.2 *Principle of iSCAT microscopy*

In iSCAT microscopy, a sample on the transparent substrate is illuminated by incident light that is then partially reflected from the glass and partially scattered by the sample. The reflected and scattered fields are collected by an objective lens and propagate along common path to the detector which minimizes the influence of external perturbations.[28] Although, the iSCAT microscope can have both reflection or transmission (also called coherent brightfield (COBRI) microscopy)[63], [69] configurations, the reflection mode is more beneficial for imaging smaller structures and objects since the incident light is only weakly reflected and does not overpower weak scattering of the subdiffraction object.[28]

The iSCAT signal (Figure 1) is result of the interference between the scattered field E_s by the object or structure in the sample and the reference field E_r that is the incident beam reflected from the interface between the cover glass and the sample (Eq (4)). For convenience, Eq (4) can be also written as

$$I = |E_r|^2 + |E_s|^2 + 2|E_r||E_s|\cos\phi \ , \tag{5}$$

where I is the total intensity at a given point in the detected iSCAT image.

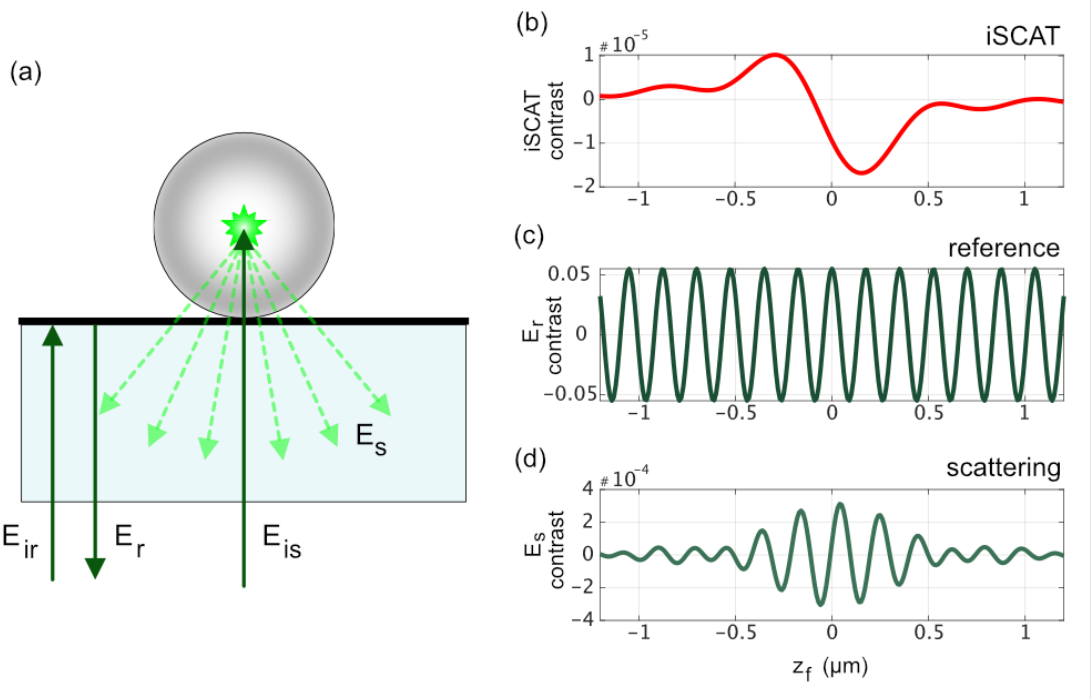

Figure 1: (a) Scheme of electric fields that generate iSCAT signal at the sample: incident beam that is scattered by the object E_{is}, back scattered field E_s, incident beam that is reflected from the cover glass E_{ir}, and reflected reference field E_r. The detected iSCAT signal (b) is then interference between reference filed E_r (b) and scattered field E_s (c). (b-d) Simulation of signals: detected contrast along the focus area, i.e. z axis (z_f).

For the subwavelength nano-objects ($D \ll \lambda$) the amount of scattered light by nanoparticle depends on its scattering cross-section as

$$\sigma_s = |s|^2 \propto \frac{8}{3}\pi^2|\alpha|^2(\lambda)^{-4} \ , \tag{6}$$

where s is complex scattering amplitude, the unitless scattering coefficient defined as ratio between scattered field E_s and incident field E_i, α is particle polarizability and λ is the illumination wavelength. The particle polarizability is further proportional to the nanoparticle volume as

$$\alpha = 3V\frac{n_s^2 - n_m^2}{n_s^2 + 2n_m^2} \ , \tag{7}$$

where V is volume and n_s and n_m are refractive indexes of scattering object and surrounding medium, respectively, which implies that scattering intensity is proportional to object volume. In purely scattering microscopy, i.e. dark-field, the signal $|E_s|^2$ decreases with a square with object volume while in interferometric scattering the signal $2|E_r||E_s|\cos\phi$ scales linearly with object volume, which makes interferometric technique more sensitive for detecting smaller and weakly scattering objects.[28], [70] However, compared to fluorescence detection, the rejection of background signals in iSCAT is more challenging.[60]

The iSCAT signal is often quantified and described as normalized intensity or iSCAT contrast, which is defined as

$$c = \frac{I - I_r}{I_r} = \frac{2E_sE_r\cos\phi}{I_r} = 2\frac{E_s}{E_r}\cos\phi \ , \tag{8}$$

where $I_r = |E_r|^2$.[59], [71]

There is number of advantages of iSCAT imaging. It is label-free and solely optical technique using visible light spectrum, there is no risk of degradation of the signal or photobleaching as opposed to fluorescence imaging, thus the observation time is not limited. Again, compared to fluorescence imaging, there is lack of saturation in iSCAT imaging. While the lifetime of fluorescent dyes limits the speed of image collection, iSCAT on the other hand is linear process and faster rate of illumination yields in higher

scattering signal.[71] The acquisition rate is only limited by the detector speed in this case.[54], [56], [59]

2.3 Diffraction theory in optical microscopy

In real conditions, the detected image of an object by an optical microscope is always affected by the point spread function (PSF) of the optical system. In general, the image formation can be expressed as[72]

$$I(x) = \int_{\mathbb{R}^3} o(t)h(x;t)\mathrm{d}t\,, \tag{9}$$

where $o(t)$ is the object and $h(x;t)$ is the PSF. The PSF of an optical imaging system can be described by diffraction theory. The diffraction formula that gave the base to majority of PSF theoretical models is the Fresnel-Kirchhoff integral approximated for the object and the detector being far distant from the aperture[72]

$$h(x_d) = \frac{-i}{q\lambda} e^{ikz} e^{i\frac{k}{2z}(x^2-y^2)} \iint h(\xi,\eta,0) e^{-i\frac{k}{z}(x\xi+y\eta)} d\xi d\eta\,, \tag{10}$$

where x_d is the imaged point, q is the distance of the detector from the aperture, λ is the wavelength, k is the wavenumber, x and y are coordinates of the point on the detector and ξ and η are coordinates of the aperture.

A successful theoretical model should reproduce the PSF of a point source, e.g. single particle, imaged by an optical system. Such PSF model could be derived using either a vectorial or scalar approach. The most general description of system's PSF can be directly derived from Maxwell's equations. The vectorial models are derived from Maxwell's equations using some approximations but still offering rigorous PSF models applicable to most optical imaging systems. The most significant vectorial PSF models were developed by Richards and Wolf,[73], [74] Török et al.[75]–[77] and Hell et al.[78] More approximated models focusing more specifically on certain aberrations of optical systems are scalar models. The most popular scalar model is Gibson and Lanni's model,[79] other scalar models focus purely on aberrations due to defocus, i.e., Born and Wolf's[80] or Hopkins'[81] model.

2.3.1 Scalar PSF theory

In the past, first introduced scalar models were derived from the diffraction theory of light and used the approximation of the Fresnel-Kirchhoff integral for the propagation of the spherical wave through an aperture.[72] The most popular scalar diffraction model by Gibson and Lanni[79] is computationally simpler and practically convenient as it directly introduces the experimental conditions as input parameters.[82], [83] It calculates the imaging aberration from the optical path difference (OPD) between the design and experimental conditions of the layers between the objective and sample.[79]

The Gibson & Lanni model accounts for aberrations caused by mismatch of refractive indexes and thicknesses among the layers in the optical path which are the immersion medium, the cover glass and the sample.[22] These imaging aberrations can be described by the OPD between the real experimental conditions and the design conditions as illustrated in the Figure 2.[79] The OPD is given by

$$OPD = [ABCD] - [PQRS]\,, \tag{11}$$

which is the difference between the beam pathway in the real experimental conditions including the sample layer [ABCD] and the beam pathway in design conditions [PQRS].[22], [79] Now, if we want to express the OPD in our desired parameters for all layers (immersion medium, cover slip, sample) we can express it from the Snell's law of diffraction as[72]

$$\begin{aligned}\Lambda(\theta, z, z_p, \tau) = z_p\sqrt{n_s^2 - n_i^2\, sin^2\,\theta} + t_i\sqrt{n_i^2 - n_i^2\, sin^2\,\theta} - \\ t_i^*\sqrt{n_{i*}^2 - n_i^2\, sin^2\,\theta} + t_g\sqrt{n_g^2 - n_i^2\, sin^2\,\theta} - t_g^*\sqrt{n_{g*}^2 - n_i^2\, sin^2\,\theta}\,,\end{aligned} \tag{12}$$

where θ is the angle between the ray propagation and the optical axis under which the ray is entering the objective lens; n_i, n_{i*}, n_g, n_{g*}, n_s are refractive indexes and t_i, t_i^*, t_g, t_g^* are the thicknesses of the immersion medium (i), cover glass (g) and sample (s), z_p is the thickness of the sample if the sample lays directly on the cover glass. The asterisk * marks the design parameter.

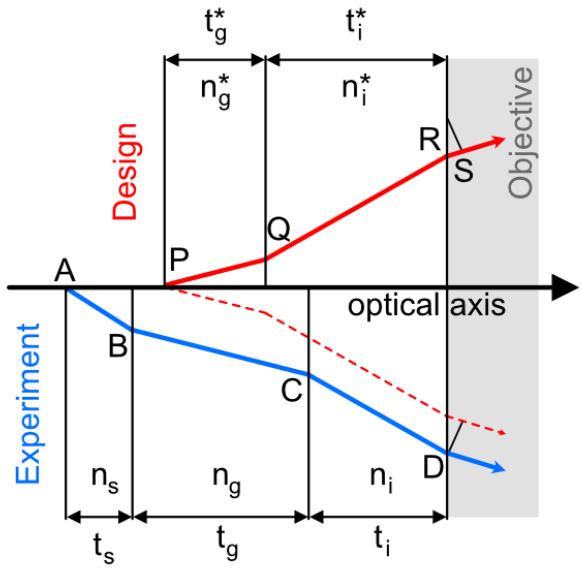

Figure 2: Depiction of the optical path of rays ABCD under experimental conditions and PQRS under design conditions.

The PSF model is acquired in 3D space. To capture the 3D scan, the sample stage is axially moving while the objective lens stays static or opposite. Either way, the distance between the stage and the objective is changing which means that the immersion oil layer thickness changes too. In that case it is easier to express how the parameter t_i depends on the focal setting of the optical system as proposed by Gibson & Lanni[79]

$$t_i = n_i \left(\frac{-z_f}{n_i} + \frac{t_g^*}{n_g^*} - \frac{t_g}{n_g} + \frac{t_i^*}{n_i^*} - \frac{z_p}{n_s} \right), \tag{13}$$

where the $z_f = z - z_p$ with z as a coordinate of the focal plane, which implies that the imaged object is best focused at $z_f = 0$. By inserting that into Eq (12) we get the final expression for OPD

$$\Lambda(\theta, z, z_p, \tau) = \left(z_p - z + n_i \left(-\frac{z_p}{n_s} - \frac{t_g}{n_g} + \frac{t_g^*}{n_g^*} + \frac{t_i^*}{n_i^*} \right) \right) n_i \cos\theta + z_p \sqrt{n_s^2 - n_i^2 \sin^2\theta} + t_g \sqrt{n_g^2 - n_i^2 \sin^2\theta} - t_g^* \sqrt{n_{g*}^2 - n_i^2 \sin^2\theta} - t_i^* \sqrt{n_{i*}^2 - n_i^2 \sin^2\theta}\,. \tag{14}$$

In the perfect system when the experimental conditions match with the design ones the aberrations would be caused only by defocus and the diffraction would follow the 3D Airy distribution pattern[80], [82] given by

$$h(x, y, 0; 0) = \left| A \int_0^1 J_0(k_0 r NA\rho)\rho d\rho \right|^2 , \tag{15}$$

where the A is an amplitude, J_0 is a Bessel function of the first kind, k_0 is the wave number in vacuum, r is the distance from the observation point to the point on the aperture, NA is numerical aperture and ρ is the normalized radius of the back focal plane. In the Gibson & Lanni model this expression Eq (15) is expanded by the phase term $\Phi(\rho, z; z_p, \tau) = k_0 \Lambda(\rho, z; z_p, \tau)$ including the OPD as

$$h(x, y, 0; 0) = \left| A \int_0^1 e^{i\Phi(\rho, z; z_p, \tau)} J_0(k_0 r NA\rho)\rho d\rho \right|^2 . \tag{16}$$

This expression (Eq (16)) can be approximated for integrating over an angular aperture in the immersion oil instead of the radius of exit pupil as[72]

$$h(x; x_p, \tau) = \left| A \frac{n_i^2}{NA^2} \int_0^\alpha e^{ik_0 \Lambda(\theta, z; z_p, \tau)} J_0(k_0 r n_i \sin\theta) \sin\theta \cos\theta \, d\theta \right|^2 , \tag{17}$$

which is usually more convenient when modelling microscope PSF.

2.3.2 Vectorial PSF theory

The vectorial diffraction theory is generally considered more accurate as it can describe the vectorial nature of light including polarization and nonparaxial field. The original vectorial theory by Wolf and Richards was significantly more complex than scalar theory but it provided highly accurate ray tracing method for radiating dipole in a focused beam.[73], [74] The vectorial approach goes beyond the paraxial approximation and describes the light as an electromagnetic wave and calculates the electromagnetic field vectors.[72], [84]–[86] It deals with the x, y, and z components of the electromagnetic field vector, each of which needs to satisfy the corresponding wave equation.[85] Solving

the wave equation, we get vectorial diffraction integrals that describe the diffracted electric field.[87]

$$I_0(x;x_p,\tau)=\int_0^{\alpha}B_0(\theta,x;x_p,\tau)\left(t_s^{(1)}t_s^{(2)}+t_p^{(1)}t_p^{(2)}\frac{1}{n_s}\sqrt{n_s^2-n_i^2\sin^2\theta}\right)\mathrm{d}\theta \quad (18)$$

$$I_1(x;x_p,\tau)=\int_0^{\alpha}B_1(\theta,x;x_p,\tau)\left(t_p^{(1)}t_p^{(2)}\frac{n_i}{n_s}\sin\theta\right)\mathrm{d}\theta \quad (19)$$

$$I_2(x;x_p,\tau)=\int_0^{\alpha}B_2(\theta,x;x_p,\tau)\left(t_s^{(1)}t_s^{(2)}-t_p^{(1)}t_p^{(2)}\frac{1}{n_s}\sqrt{n_s^2-n_i^2\sin^2\theta}\right)\mathrm{d}\theta \quad (20)$$

where t_s and t_p are the Fresnel transmission coefficients for orthogonal (s) and parallel (p) polarizations and

$$B_m(\theta,x;x_p,\tau)=\sqrt{\cos\theta}\sin\theta\,J_m(krn_i\sin\theta)e^{ik\Lambda(\theta,z;z_p,\tau)}\,. \quad (21)$$

The detected electric field is[72]

$$e=\begin{bmatrix}-iA(I_0+I_2\cos(2\varphi))\\-iAI_2\sin(2\varphi)\\-2AI_1\cos\varphi\end{bmatrix}, \quad (22)$$

where φ is azimuth angle around the optical axis. The PSF is then integrated over φ as

$$h(x;x_p,\tau)=\frac{1}{2\pi}\int_0^{2\pi}\frac{1}{16\pi}|e|^2=\frac{|A|^2}{16\pi}(|I_0|^2+2|I_1|^2+|I_2|^2)\,. \quad (23)$$

2.3.3 Combining scalar and vectorial approach

The early Wolf's vectorial model was later reformulated for more general use. For example, Török and Varga[87] modified the model for the electromagnetic waves that are focused through a stratified medium with mismatched refractive indices and it was shown[75], [82] that such vectorial ray tracing technique can be used together with the OPD as described by Gibson and Lanni. Likewise, the polarization ray tracing technique[88] using generalized Jones matrices and Debye-Wolf integral, which is used in this work to model PSF of iSCAT microscope (4.2), also share such similarities to ray tracing in geometrical optics.[87], [88] Therefore, it is possible to use the Gibson and

Lanni's expression for OPD as a phase term and conveniently utilize it with appropriate vectorial models.

In Török and Varga's vectorial model, they describe the electric field in the focal region by tracing electric vector and its components in spherical polar coordinates that propagates through lens and *N*-layer medium.[75], [76], [82], [89] The result of their derivation returns three electromagnetic field Cartesian components that are defined as

$$e_{3x} = -i(E_0 + E_2 \cos 2\varphi) \tag{24}$$

$$e_{3y} = -i(E_2 \sin 2\varphi) \tag{25}$$

$$e_{3z} = -2E_1 \cos \varphi \tag{26}$$

where the integrals E_0, E_1, and E_2 are in this case

$$E_0 = A\frac{n_i^2}{NA^2}\int_0^{\alpha} e^{ik_0\Lambda} J_0(k_0 r n_i \sin\theta)\sqrt{\cos\theta}\sin\theta\,(1+\cos\theta)e^{ik_0 n_i z\cos\theta}\mathrm{d}\theta \tag{27}$$

$$E_1 = A\frac{n_i^2}{NA^2}\int_0^{\alpha} e^{ik_0\Lambda} J_1(k_0 r n_i \sin\theta)\sqrt{\cos\theta}\sin\theta\,(\sin\theta)e^{-ik_0 n_i z\cos\theta}\mathrm{d}\theta \tag{28}$$

$$E_2 = A\frac{n_i^2}{NA^2}\int_0^{\alpha} e^{ik_0\Lambda} J_2(k_0 r n_i \sin\theta)\sqrt{\cos\theta}\sin\theta\,(1-\cos\theta)e^{-ik_0 n_i z\cos\theta}\mathrm{d}\theta \tag{29}$$

which are the integrals defining the electric filed for circularly polarized light, where *A*, $J_{0,1,2}$, k_0, and *r* are the amplitude, the Bessel function of the first kind with the subscript defining its order, the wavenumber in a vacuum, and the distance $r = \sqrt{x^2 + y^2}$ from the detection center to a point on the image plane with coordinates *x* and *y*, respectively. The phase term, $k_0\Lambda(\theta, z; z_p, \tau)$, is defined by the wavenumber of the illumination/scattered light k_0 and OPD. The calculated PSF is given as the integration performed over an angular aperture in the immersion oil with $\alpha = \sin^{-1}\frac{NA}{n_i}$.[79]

2.4 Single particle tracking

Single particle tracking (SPT) is a powerful method to study intracellular dynamics, transport in membranes[90] or inside cells,[91] dynamics of motor proteins[92] and mapping structures[93] providing information not only about the object itself but its surrounding environment as well. The most widely used is fluorescence-based SPT that

has the key advantage of easy background rejection and use of molecular-sized labels.[94] However, its it has some limitations like photobleaching and blinking that result in short observation time and poor statistics in processes with fast dynamics. Additionally, saturation limit restrains the number of emitted photons and so integration times are typically longer than several milliseconds which greatly limits the spatiotemporal resolution.[28], [59]

Scattering labels can be a possible alternative to fluorescent labels. Scattering based microscopies like iSCAT does not face those limitations of fluorescence methods. Scattering signal does not bleach, blink or saturate which enables unlimited observation time and high speed and high precision tracking. On the other hand, weaker scattering of small nanoparticles and scattering background may be an obstacle when imaging especially in live cells. It is possible to increase the signal from small scatterer by increasing the laser power, but that option is limited in living cells due to phototoxicity of laser light. This limitation can be then addressed by background subtraction methods[95] and using larger labels. Although, the general rule in cell imaging is that the smaller probe the better,[59] so far it was proven that the smallest possible label to track by iSCAT was 40 nm GNP in living cell[93] and 10 nm GNP in vitro.[59]

To this date, most attention was paid to GNPs in cellular tracking by iSCAT. However, highly scattering and biocompatible fNDs have a potential to exceed the metallic nanoparticle detection limit and improve the SPT by iSCAT.

2.4.1 Particle tracking in iSCAT microscopy

Reaching high spatiotemporal resolution is especially important to be able to observe fast and momentary events,[64], [96] e.g., endocytosis that can arise in a scale of milliseconds.[97]–[99] iSCAT microscopy enables nanometre precise tracking with sub-millisecond temporal resolution[19], [54], [100] that can reach up to microsecond resolution with accordingly fast camera.[56] This case, however, applies for detection with minimal well controlled background. Reaching such resolution in complex, highly scattering and time varying systems like living cells is more challenging.

Imaging subdiffraction objects in optical microscopy returns only finite-size PSF limited by diffraction limit which is in order of 200 nm for visible light.[28] It is possible to localize the object position more accurately by finding the centre of mass of the PSF, for example, by fitting it with Airy PSF function or two-dimensional (2D) Gaussian

function. For high NA microscopes like iSCAT, Gaussian function fitting is more suitable[101] and most often used. For shot-noise-limited detection, it is possible to reach few nanometre localization precision for number of detected photons $N_p > 10^4$.[102]

The particle is fitted and localized in every frame which finally reveals the whole trajectory. The trajectory can be then analysed. The parameters that are usually extracted from the trajectory data are for example distance, velocity,[103] step size,[104] diffusion coefficient D,[105] mean square displacement (MSD)[106] or the probability distribution of squared displacements (PDSD).[107]

2.4.2 Mean square displacement analysis

One of the quantitative ways to describe nanoparticle motion is MSD analysis. MSD is a measure of particle's position deviation during its diffusion from the initial position over time. Two-dimensional MSD accounts for particle motion in x and y axes and it is defined as

$$MSD = \langle \Delta r^2(t) \rangle = \frac{1}{N} \sum_{i=1}^{N} [(x_i(t) - x_0(t_0))^2 + (y_i(t) - y_0(t_0))^2] \,, \qquad (30)$$

where N is number of samples to be averaged, coordinates ($x_i(t_0)$, $y_i(t_0)$) represent the initial particle position and coordinates ($x_i(t)$, $y_i(t)$) is position of the particle at the time t. The particle motion is often interpreted from a plot of MSD dependence on time t (Figure 3).[108]

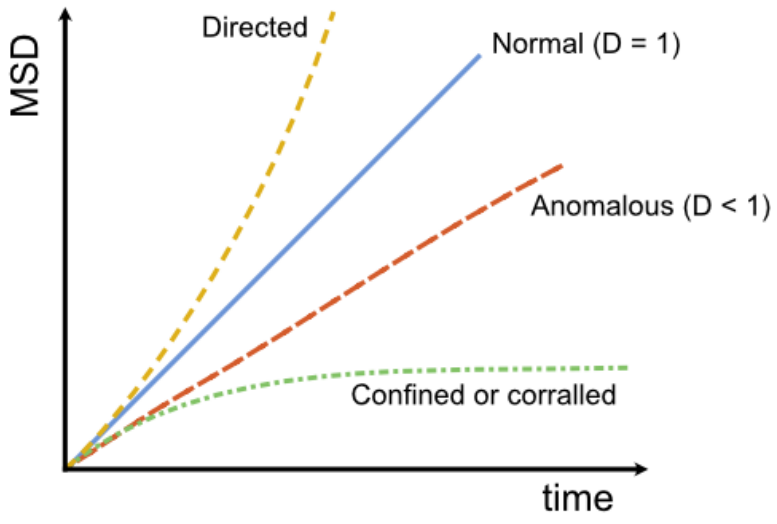

Figure 3: Examples of MSD plots of different types of diffusion

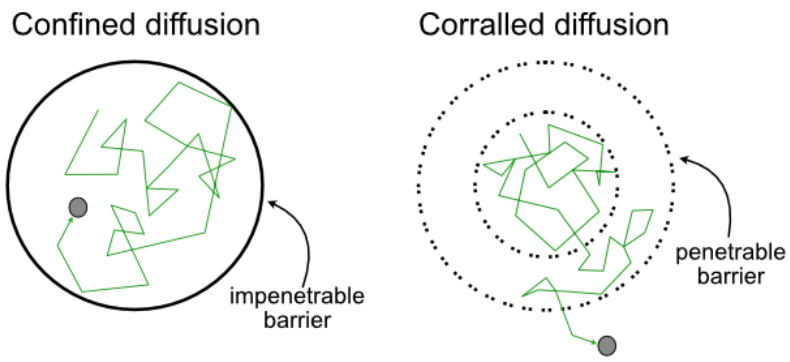

Figure 4: Difference between confined and corralled diffusion

The tracked particle can undergo several types of motion such as normal diffusion, anomalous diffusion, confined diffusion, corralled diffusion, directional motion or immobile, and each of them can reflect on the MSD curve shape. We can classify the mode of motion by fitting the MSD curve with appropriate fitting function:

$$MSD = 4Dt \tag{31}$$

is formula for normal diffusion, *i.e.*, Brownian motion, where D is diffusion coefficient, and the MSD curve is linear with time. Brownian motion occurs when particle moves freely without any restrictions or influence from its surroundings.

$$MSD = 4Dt^{\alpha} \tag{32}$$

represents anomalous diffusion, where α is a parameter that distinguishes the mode of motion between sub-diffusion ($\alpha < 1$, more spatially confined motion) and superdiffusion ($\alpha > 1$, motion with fast jumps). Anomalous diffusion takes place when a particle is constricted by some obstacle during free diffusion. For example, when particle is diffusing along the cell membrane and is caught up in various pits during its motion or when cytoskeleton is restraining particles from free motion in the cytoplasm.

$$MSD = 4Dt + (vt)^2 \tag{33}$$

stands for directed motion with diffusion, where *v* is speed of the directional motion. This type of motion can occur for example with active transport in the cell.[109] Directed motion is connected to active transport in cells.

$$MSD = \langle r_C^2 \rangle \left(1 - A_1 e^{-4A_2 \frac{Dt}{\langle r_C^2 \rangle}} \right) \tag{34}$$

Describes confined motion, where r_C is the radius of the confinement of and A_1 and A_2 define the confinement geometry. Confined motion takes place when a particle is trapped in one area, e.g. diffusion inside a vesicle. (Figure 4)

The most data points of MSD analysis are obtained for the short time-lags *t* and with increasing time of the trajectory measurement less data points are available.[110] This means that for long time-lags the uncertainty of MSD analysis is higher.[111] Therefore, only the first ~ $\frac{1}{4}$ of data points are typically used for MSD motion evaluation.[108], [110]

The trajectory of the nanoparticle interacting with the cell provides not only information about the interaction itself but also reveals information about the surroundings, cell structure and cell behaviour.

2.5 Interaction of nanoparticles with cells

The interaction of nanoparticles with cells refers to all the processes from the first contact, interaction with the outer membrane, internalization, transport and interactions inside the cell, to excretion of the nanoparticle.

According to particle's type, size and surface functionalization it can enter the cell by various mechanisms. The uptake mechanisms can be

(a) Phagocytosis which is an uptake mechanism mostly used for the larger micrometre-sized particles, dead cells, cell debris or pathogens.[112], [113] The internalization starts with formation of membrane protrusions. The protrusions close around the particle and create a vesicle inside the cell called phagosome.

(b) Pinocytosis and macropinocytosis is actin-controlled process also used for uptake of large particles and extracellular fluid.[112] The internalization is performed by membrane extensions that form vesicles called macropinosomes (0.2 – 5 μm large)[114] and enclose extracellular fluid and particles.[112], [113], [115]

(c) Clathrin dependent endocytosis is receptor-specific mechanism. Clathrin is a protein that coats membrane pits on the cytosolic side of the plasma membrane.[116] Those pits are spots of endocytosis when a particle is bound to the receptor protein on the membrane. The clathrin assembly engulfs the particle and creates a clathrin coated vesicle.[112] This uptake mechanism is mostly triggered by viruses[117], [118] and most frequent mechanism of ND uptake where the hydrophobic or electrostatic interaction initiate the uptake.[114], [119]
(d) Calveolin dependent endocytosis is similar process to clathrin-mediated endocytosis where the calveolin coats the membrane pits and forms vesicles called calveolae with diameter 50-80 nm.[120], [121]
(e) Receptor mediated endocytosis is process purely based on receptor-ligand binding without clathrin or calveolin forces.[117]
(f) Non-specific endocytosis can occur for large particles with some provided force.[122]–[126] This process can be harmful to the cell.[112]
(g) Translocation is a process when small particles or molecules cross the membrane by diffusion.[112]

If the goal is to observe the endocytosis itself or speed up the uptake process of the nanoparticle, the internalization rate can be accelerated by several mechanisms. It can be accomplished (i) by environment conditions, where the most suitable conditions for cellular uptake are 37 °C, atmosphere with 5 % of CO_2[119] and medium of pH 7.4, (ii) by coating the nanoparticle with polymer, where well received polymers by cells are, *e.g.*, PEG (polyethylene glycol) or PG (polyglycerol)[127], or (iii) by mechanical stimulation of the cell by cyclic strain[128]. There were also attempts to accelerate the internalization rate by chemical stimulation of the cell by Ca^+ or glucose[129], however, in that case no endocytosis rate increase was observed.

2.6 Fluorescent diamond nanoparticles

Fluorescent nanodiamonds (FND) have received a great attention with development of nanoscience and imaging techniques due to their excellent physical and chemical properties and multiple of potential applications.[130]

Imaging in living systems has always been a challenge, especially imaging and tracking cells in vivo. For those purposes, labels with specific properties are required. Fluorescent dyes can be problematic because of fast photobleaching. Good alternative to

fluorescent dyes became inorganic nanoparticles such as iron oxide nanoparticles or quantum dots (QD).[131] However, those are potentially toxic and mostly water-insoluble.[132], [133] Now, carbon-based fluorescent nanoparticles became a suitable option for stable fluorescent probes in bioimaging applications because of their photostability without photobleaching or blinking, bright fluorescence, good biocompatibility and easy surface functionalization.[134]–[136] As a downside, the intrinsic number of fluorescent centres in a nanodiamond is relatively low[137] and the concentration of the centres decreases nonlinearly with decreasing crystal size[138]. An additional benefit of those particles is the high index of refraction,[138] which gives rise to light scattering even for very small particles. Combination of these properties allow long-term observation in living cells.

FNDs are sp3 nanocarbon allotropes.[131] The nitrogen-vacancy (N-V) defects as fluorescent centers[139] give FNDs the extraordinary photophysical properties. N-V centres embedded in the crystal matrix emit red fluorescence at 550-800 nm when exposed to green-yellow light,[136], [140] a broad emission spectrum (spectral width >200 nm), and a long fluorescence lifetime (>10 ns).[130] Colour centres $(N\text{-}V)^0$ and $(N\text{-}V)^-$ are produced by high-energy radiation damage that creates defects in the diamond matrix which is followed by annealing that activates the defect centers.[130], [131], [136] When it comes to the toxicity, study of FNDs showed that FND is highly biocompatible material and does not cause any oxidative stress responses in vivo.[134], [141] Another advantage of FNDs in bioimaging is that NV centres emit fluorescence in the range of 550-800 nm while most of the biomolecules typically absorb at wavelengths 300-500 nm.[136] Especially, the negatively charged centre $(N\text{-}V)^-$ is of particular interest. The $(N\text{-}V)^-$ centre absorbs strongly at 560 nm and emits fluorescence at ~700 nm which is at the window for convenient bioimaging.[137] However, the intrinsic amount of $(N\text{-}V)^-$ in ND is relatively low, which restricts its bioimaging applications especially when FNDs for bioimaging should be small (~25 nm or less).[137] The concentration of N-V centres increases nonlinearly with crystal size[138] and their distribution is not homogenous in individual ND particles.[142]

NDs can be useful as drug and gene delivery vehicles,[134], [143] light scattering labels with their high refractive index and unique Raman scattering, FNDs can be applied as markers for imaging[138] for example for real-time sensing of ion channels, as a chemical sensors, for tracing neuronal processes or revealing the relation between particle shape and their intracellular fate.[142]

2.6.1 Interaction of nanodiamonds with cells

It has been observed that NDs can be successfully internalized in many types of cells. The internalization process can be spontaneous, or to trigger different types of internalization processes drugs can be used or the surface of ND can be functionalized.

The factors that affect the uptake mechanism are size, shape and surface chemistry like charge and functional groups. The preferential way of internalization of NDs smaller than 100 nm is clathrin-mediated endocytosis.[119], [144], [145] ND surface has naturally negative charge and the interaction with cell membrane is therefore most probably an electrostatic interaction.[146] Amine functionalization or transferring grafting are ways used to change the ND surface to positive charge.[146] Positively charged NDs are then most likely internalized by receptor-mediated endocytosis.[146] Other internalization pathways can be also triggered by polymer coatings such as poly-ethyleneimine (PEI) or poly-allyleamine hydrochloride (PAH).[144], [145]

It was observed that inside the cells the NDs do not enter the nucleus and are mostly located at the perinuclear cytoplasm.[119] Additionally, there is difference between small and larger particles which links to their uptake mechanism. The small particles were found to be free in cytoplasm, but the larger particles were enclosed inside intracellular vesicles.[16], [144], [147]

3 Materials and methods

3.1 Fluorescence combined iSCAT microscopy setup

The simplified schematics of the fluorescence-combined iSCAT microscope is pictured in Figure 5.

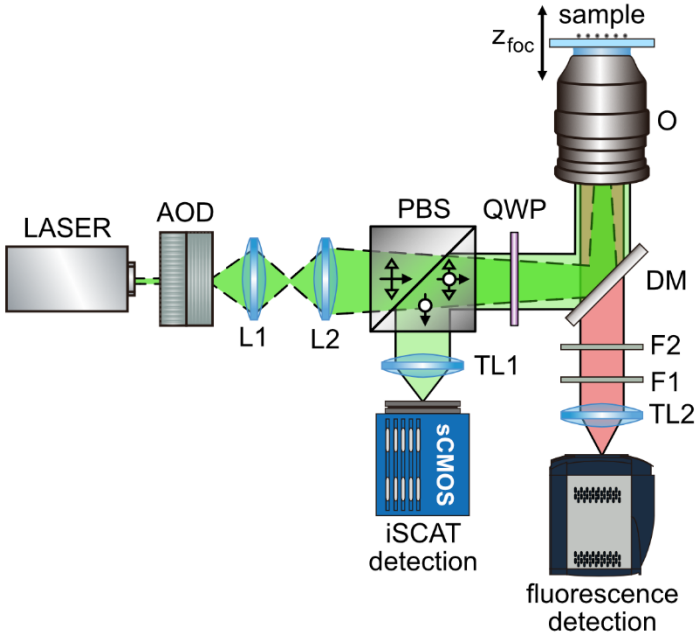

Figure 5: Fluorescence combined iSCAT microscope. The green dashed-outlined beam pathway marks the incident beam to the sample, the green solid-outlined beam pathway is then the scattered light traveling to the sCMOS detector, the red beam shows fluorescence from NPs. Optical elements in the setup are acousto-optic deflector (AOD), lenses (L1, L2, TL1, TL2), polarizing beam splitter (PBS), quarter-wave plate (QWP), objective (O), dichroic mirror (DM), notch filter (F1), and emission filter (F2).[23]

The incident 532 nm laser beam (OBIS-FP-532LX, Coherent, USA) is steered in X and Y directions by the acousto-optic deflector (AOD, DTS-XY400-532, AA Optoelectronics Ltd, France) for accurate wavefront shaping. The laser beam is then filtered and projected through the 4f telecentric lens system (L1 and L2, AC254-500-A, Thorlabs, USA), the polarizing beam splitter (PBS, CCM1-PBS25-532, Thorlabs, USA), and the quarter-wave plate (QWP, WPQ10M-532, Thorlabs, USA) onto the back-focal plane of the objective lens (O, PLAPON60XO, oil-immersion, NA = 1.42, Olympus, Japan) and sample.[23]

iSCAT detection pathway: The back-scattered light from the sample is reflected by the dichroic mirror (DM, Di03-R532-t1-25′36, Semrock, USA) and sent through a lens (TL1, same as L1) onto the sCMOS detector (pco-edge 4.2, PCO, Germany).

Fluorescence detection pathway: The emitted fluorescence from the sample is directed through a lenses (TL2, same as L1), a notch filter (F1, NF03-532E-25, Semrock, USA) and an emission filter (F2, FF01-709/167-25, Semrock, USA) to block the stray light and leakage of the excitation beam, on the EMCCD detector (iXon897, Andor, UK).

The iSCAT and fluorescence signals of the same area are detected simultaneously (Figure 7). The sample is held by the high precision XYZ-piezo stage (P-545.3C8S, Physik Instrumente, Germany). The back-scattered signal from a nanoparticle was recorded by moving the sample stage along its z-axis over a range of focal depth 6 µm with the center at the vertical position of the nanoparticle (Figure 6). The step of z-axis scanning was typically smaller or comparable to the object size, *e.g.*, for 40 nm nanoparticle the step size was 10 nm. The laser power had to be adjusted for each measurement to avoid the oversaturation of scattering or fluorescence signals. All other parameters were set to be the same for most measurements to acquire comparable data.

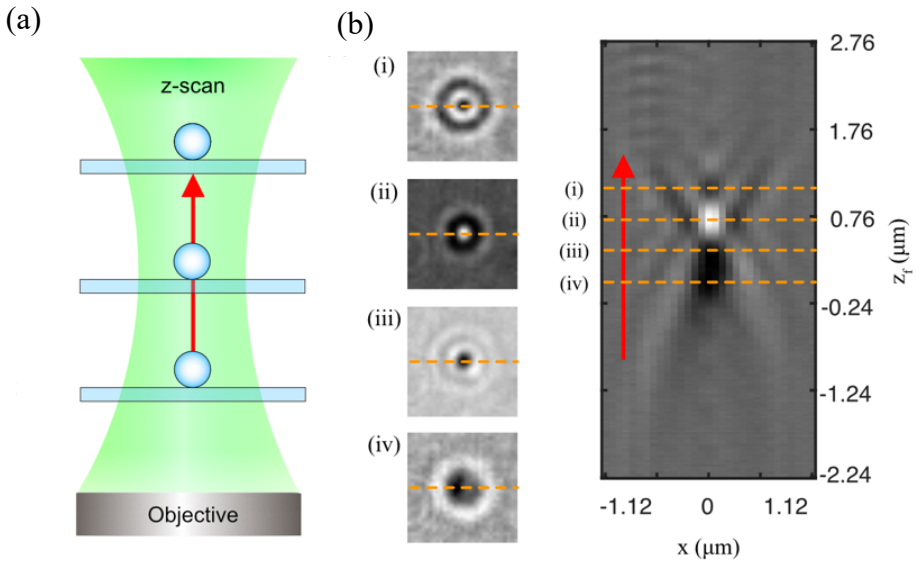

Figure 6: (a) Schematics of z-scanning in a direction of the red arrow by moving the sample stage and (b) representative example of axial variation of iSCAT image of a nanoparticle (diameter 120 nm) created by z-scanning. (i-iv) are x-y plane ROI corresponding to positions marked by orange dashed line in the x-z plane view.[23]

The experimental setup and its modifications were also described in several published works (reference [17], [23], [65], [66]).

3.1.1 Measurement of the iSCAT contrast and fluorescence from nanoparticles

The iSCAT signal results from the interference between the scattered field from the sample and the reference field reflected from the cover glass surface. The total iSCAT intensity at the detector is given by Eq (5).

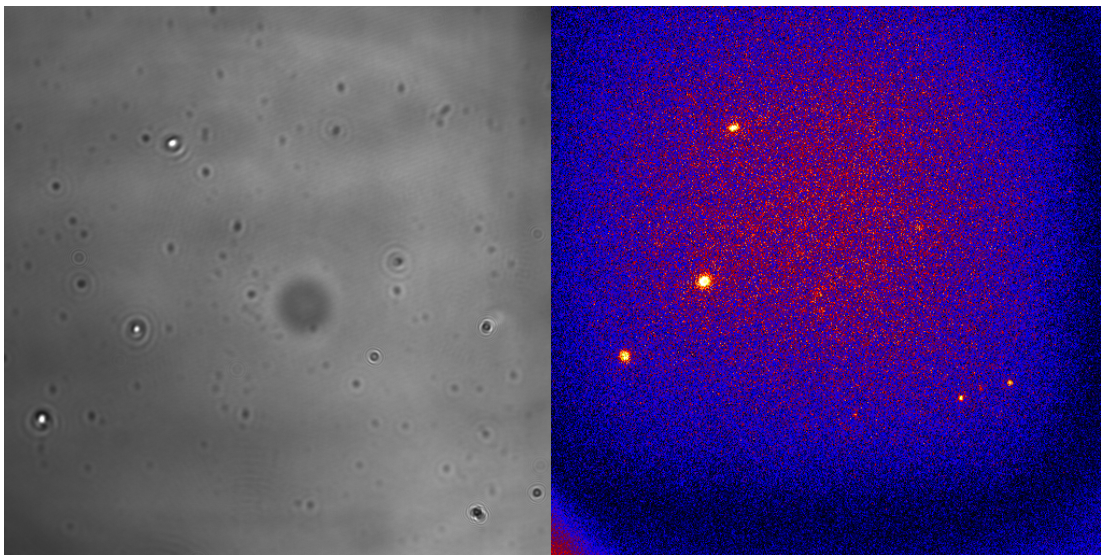

Figure 7: Simultaneous detection of iSCAT (left) and fluorescence (right) image. Size of the detection window is 40 µm / 1024 pixels for iSCAT and 62 µm / 512 pixels for fluorescence detection

The image-acquisition-based iSCAT microscope enables to detect spatial intensity distribution. The spatial intensity distribution of a diffraction-limited spot, *e.g.* nanoparticle, corresponds to the PSF of the microscope. The Figure 6 b) shows the example of PSF images of a particle at different focal depths. The region of interest (ROI) for analysing the particles (Figure 6 b) i-iv) was chosen to be 7×7 pixels with centre at the position of the particle to capture the whole iSCAT image of a nanoparticle and get the least amount of the surrounding noise at the same time.[23] This image was fitted at each z-position with a 2D Gaussian function:

$$\mathrm{PSF}(x,y) = A \cdot \exp\left(-\left(\frac{(x-x_0)^2}{2s_x^2} + \frac{(y-y_0)^2}{2s_y^2}\right)\right) + B\,, \qquad (35)$$

where A is the amplitude, B is the intensity offset that refers to the background in the image, x_0 and y_0 are the coordinates of the centre of ROI and the nanoparticle, and σ_x and σ_y are the widths of the 2D Gaussian function. If we apply this to Eq. (5), we get $|E_S|^2 +$

$2|E_R||E_S|\cos\phi = PSF(x_0, y_0) - B$ and $|E_R|^2 \cong B$.[23] After normalization and background subtraction the signal at the centre is

$$I_{\exp}(x_0, y_0) = \frac{A}{B} = (|E_S|^2 + 2|E_R||E_S|\cos\phi)/|E_R|^2 , \quad (36)$$

which is referred to as iSCAT scattering contrast.

The fluorescence contrast (I_{fl}) was calculated as the ratio of the amplitude (A) and background offset (B), that is, $I_{fl} = A/B$.[23]

3.2 Nanoparticle samples

Throughout this work, two polystyrene (PS) bead samples of sizes 40 nm and 100 nm (FluoSpheres™ Carboxylate-Modified Microspheres, fluorescent (540/560), F8792/F8800, ThermoFisher Scientific, USA), and 120 nm latex bead sample (Aldehyde/Sulfate latex bead, 4%, 0.1 μm, A37287, Lifetechnologies, USA) were used mostly for reference measurements.

The fND samples used for the experimental work were both commercial fND samples purchased from Sigma-Aldrich (35 nm) with 1–4 NV^- centres per particle, and laboratory-made fND samples of various sizes (10 nm, < 50 nm, and ~ 150 nm) with broad size distribution.

The laboratory made fND samples were prepared as follows: they were purified from commercial ND powder (Microdiamant Switzerland, MSY 0-0.25 and MSY 0-0.1) and irradiated with 16.6 MeV electron beam (1.25×10^{19} electrons/cm^2) from MT-25 microtron. These ND samples were then annealed at 900°C for 1 hour in an argon atmosphere, followed by oxidation at 510°C for 4 hours at atmospheric pressure in a Thermolyne 21100 tube furnace. The sizes of fNDs were determined with nanoparticle tracking analysis (NTA) (NanoSight LM10, Malvern Panalytical, UK) or transmission electron microscopy (TEM) (Tecnai G2 20, FEI Company, USA).

3.2.1 Diamond nanoparticle samples characterization by commercial methods

Because most of fND samples in this work were laboratory made and because ND do not typically form round shapes, their size and shape were defined by commercially known methods first which helped with understanding our experimental results later. The methods for characterization of such small particles with irregular shape was transmission

TEM and NTA. The TEM offers very precise measurement of the size as well as the insight into nanoparticle shape, whereas the NTA can measure the size of hundreds of nanoparticles at the same time and provides highly statistical size distribution data.

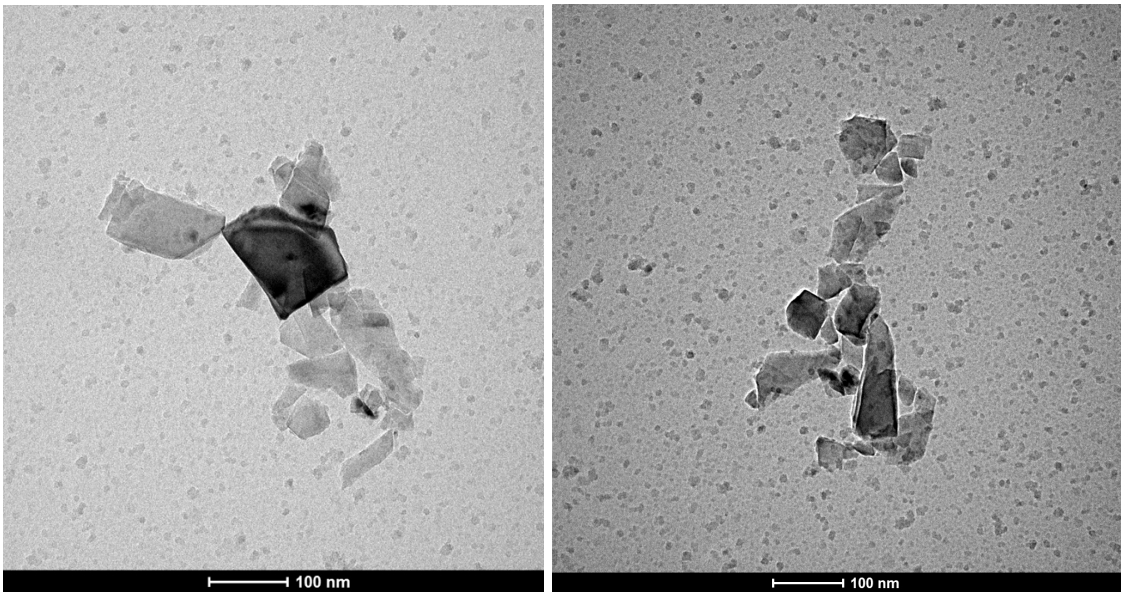

Figure 8: TEM images of fNDs, large variation of sizes and shapes can be observed. Scale bar 100 nm

The TEM images showed that the fNDs have, as expected, non-spherical irregular shape (Figure 8). The measured average aspect ratio, which is the ratio between the width and the height of the particle, was in average 1.7 in all the fND samples. Due to the complex fND shape, the diameter of individual fNDs in the TEM images was evaluated by Feret diameter. Feret diameter is calculated from the two-dimensional 2D projection or an outline of a measured object. It is an averaged distance between two parallel tangential lines over all directions around the object.[148], [149] The software ImageJ was used for the Feret diameter calculation. The shape of the fNDs imaged by TEM, the shape outline used for the Feret diameter calculation and the calculated size distribution are in the Figure 9: (a) for the smallest fND sample the Feret diameter was $D_{TEM} = 11 \pm 7$, (b) the purchased fND sample had sizes in a range $D_{TEM} = 65 \pm 19$, (c) laboratory made fND sample with reportedly particle size < 50 nm had $D_{TEM} = 24 \pm 8$, and (d) the largest fND sample also had the largest size distribution $D_{TEM} = 107 \pm 64$.

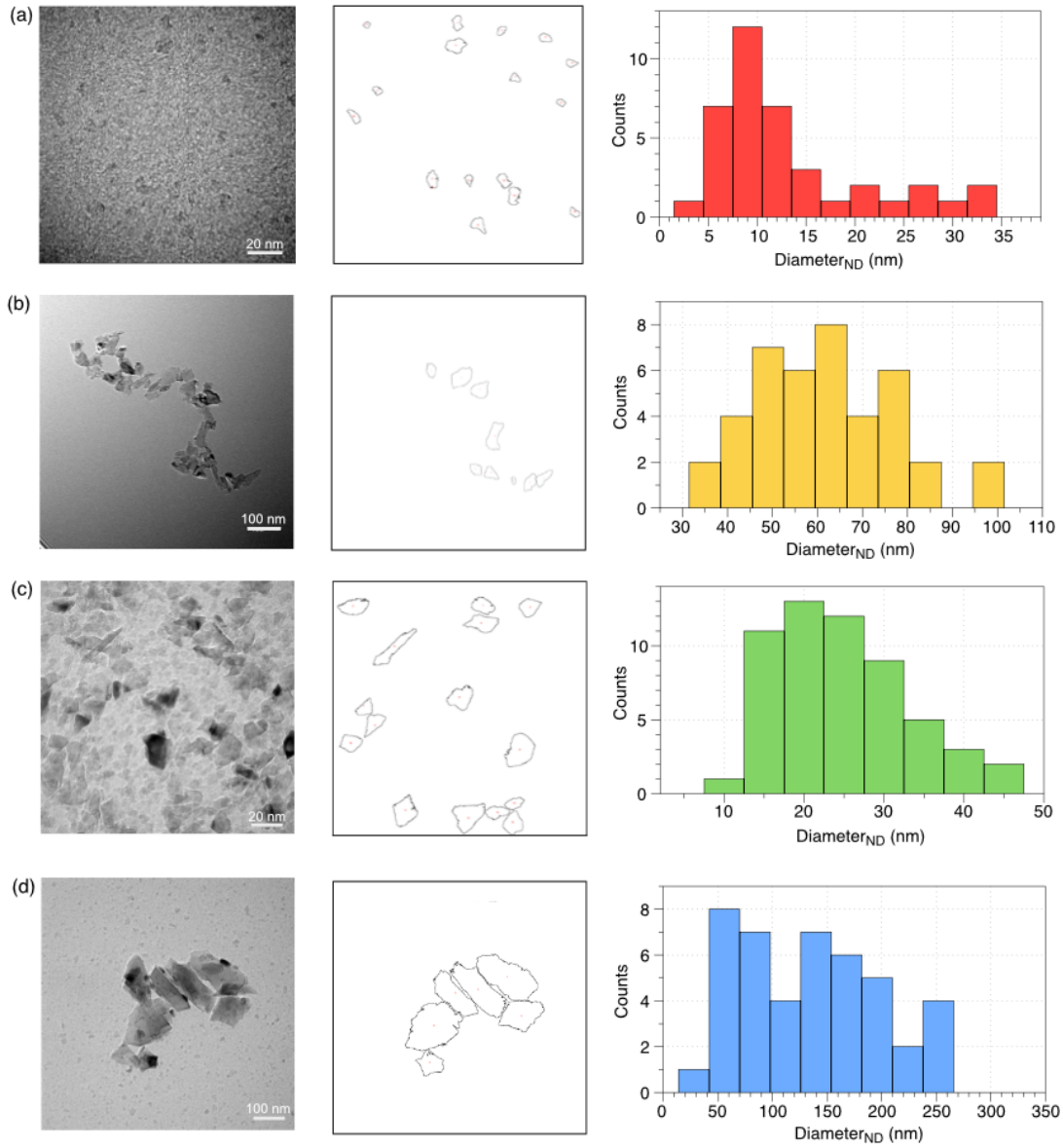

Figure 9: The four groups of fND samples are (a) 10 nm laboratory made fNDs (b) Sigma-Aldrich purchased fNDs (c) <50 nm laboratory made fNDs and (d) ~ 150nnm laboratory made fNDs. First column are representative TEM images used to analyse the Feret diameter of the fND, second column are the outlines of well distinguishable fNDs created by ImageJ and used for the Feret diameter calculation and the third column are histograms of the obtained fND diameters

The NTA method measures the diffusion coefficient of the particles in the solution which is directly connected to the particle size as

$$Dt = \frac{K_B T}{3\pi\eta d} t \,, \tag{37}$$

where D is the diffusion coefficient, t is time, K_B is Boltzmann constant, T is the temperature, η is viscosity and d is diameter of the diffusing particle. The results of NTA

measurement are in Figure 10. The method failed for the smallest fNDs because it is smaller than the size limit for reliable measurement on NTA which is ~ 60 nm with 642 nm excitation that was used. The peak value for the < 50 nm fND sample is 50 nm, for the ~ 65 nm fND sample is 77 nm peak value and for the ~150 nm fND sample the peak value is 140 nm. Same as for the TEM measurement, it was confirmed that the size distributions are large for each sample.

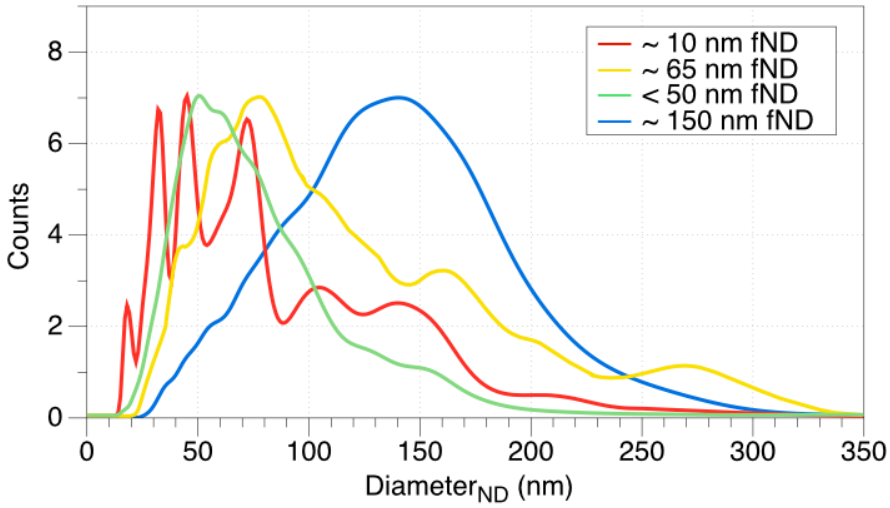

Figure 10: fND sizes measured by NTA. The measurement of the 10 nm fND sample failed due to the sensitivity of the NTA method which is not suitable to measure such small particles. The fND samples correspond to Figure 9.

3.2.2 Sample preparation for iSCAT characterization

PS and latex beads were first sonicated for 10 minutes and diluted from a stock solution. Diluted samples were pipetted into ibidi channels (µ-Slide I Luer, 80167, ibidi, Germany). Due to the electrostatic forces the negatively charged beads adhere to the glass surface. The excess solution was immediately washed out with deionized water to prevent overloading the glass surface with beads.

Dispersed fNDs in deionized water (0.1 mg/ml) were sonicated for 15 minutes first to break potential clusters. Sonicated fND samples were pipetted (50 µl) into glass chambers made of two cover glasses and a double-sided tape. The fND solution was left to evaporate overnight. After evaporation, the sample chamber was carefully loaded with water and sealed to avoid drying. Most fNDs stay attached on the glass surface after the drying step and adding water does not disrupt that bond.

3.2.3 Preparation of PEGylated nanodiamonds

PEG coating on fNDs was prepared according to "grafting to" method[150]. First, the carboxyl groups were created on the fND surface by oxidation: 0.1 g of fNDs was mixed with 90 ml of H_2SO_4 (98%) and 30 ml of HNO_3 (68%), Mixture was sonicated at 25 °C and 40 kHz for 30 minutes. Next, it was stirred in oil bath at 80 °C for 7 days. After cooling down, the mixture was centrifugated and the solid residue was washed with deionized water until reaching neutral pH. Precipitate was collected and dried under vacuum at 60 °C. Next step was PEG conjugation on the COOH groups: 0.1 g of fND-COOH was refluxed in 30 ml of toluene and 10 ml of $SOCl_2$ on rotary evaporator under vacuum. After, 1 g of polyethyleneglycol monoethylether (mPEG) and 0.5 ml of triethylamine (TEA) was added to the nanoparticles. Mixture was heated to 100 °C and stirred for 24 hours under nitrogen atmosphere. After cooling down, the mixture was centrifuged at 700 rpm for 30 minutes and the solvent was removed. Precipitate (fND-PEG) was collected by washing it five times with methanol and letting it dry in vacuum at 60 °C overnight.

3.3 Sample preparation for cellular imaging

Human osteosarcoma U2OS cells were used for the cell and fNDs interaction experiments. The cell cultures were prepared by proliferation from the original cell culture purchased by ThermoFisher Scientific. The new culture was prepared from the original or previously used cell culture when the growth of the cells covered approximately 70 % of culture dish bottom surface. Then the growth medium was removed and 10 ml of HBSS (Hanks' Balanced Salt Solution) to wash the cells from the medium. The HBSS was removed after 1 minute and 2 ml of trypsin was added to detach the cell from the culture dish bottom. The culture dish was placed in the incubator for 5 minutes. Afterwards, 2 ml of RPMI medium was added and the cells in solution were centrifuged for 1 minute. The supernatant after centrifugation was removed and 1 ml of RPMI was added. Finally, the cells were pipetted into petri dish with PDL coating for the observation under the iSCAT microscope. For low concentration of the cells, 3 µl was pipetted into 300 µl of RPMI in the petri dish. For high concentration of the cells, 10 µl was pipetted into 300 µl of RPMI in the petri dish. The rest of the cells was saved for next cell cultivation (100 µl in 10 ml of RPMI – 400 times diluted).

4 Determination of nanoparticle size by axial profiling of interferometric scattering microscopy

This chapter was published as: Žambochová, K. *et al*. Axial profiling of interferometric scattering enables an accurate determination of nanoparticle size. *Optics Express* 31(6), 10101, (2023).[23]

4.1 Introduction

Interferometric scattering (iSCAT) microscopy has undergone significant development in recent years. It is a promising technique for imaging and tracking nanoscopic label-free objects with nanometre localization precision. The current iSCAT-based photometry technique allows quantitative estimation for the size of a nanoparticle by measuring iSCAT contrast and has been successfully applied to nano-objects smaller than the Rayleigh scattering limit. Here we provide an alternative method that overcomes such size limitations. We take into account the axial variation of iSCAT contrast and utilize a vectorial point spread function model to uncover the position of a scattering dipole and, consequently, the size of the scatterer, which is not limited to the Rayleigh limit. We found that our technique accurately measures the size of spherical dielectric nanoparticles in a purely optical and non-contact way. We also tested fluorescent nanodiamonds (fND) and obtained a reasonable estimate for the size of fND particles. Together with fluorescence measurement from fND, we observed a correlation between the fluorescent signal and the size of fND. Our results showed that the axial pattern of iSCAT contrast provides sufficient information for the size of spherical particles. Our method enables us to measure the size of nanoparticles from tens of nanometres and beyond the Rayleigh limit with nanometre precision, making a versatile all-optical nanometric technique.

4.2 Theoretical model development

To understand the scattering from nanoparticles and extract the information about them, we need to use an appropriate model to describe our system. A successful theoretical model should reproduce the PSF of an NP. Such a PSF model could be derived using either a vectorial or scalar approach. Scalar models derived from the diffraction theory of light use the approximation of the Fresnel-Kirchhoff integral to describe the propagation

of a spherical wave through an aperture.[72] The scalar diffraction model by Gibson and Lanni (G-L) is computationally simpler and practically convenient as it directly introduces the experimental conditions as input parameters.[82], [83] It calculates the imaging aberration from the OPD between the design and experimental conditions of the layers between the objective and the sample.[79]

On the contrary, the vectorial model by Richards and Wolf (R-W) is rather complicated, but it provides an accurate ray tracing method for a radiating dipole in a focused beam.[73], [74] Their vectorial approach is based on Maxwell's equations and calculates the electromagnetic field vectors,[72], [84], [85] the *x*, *y*, and *z* components of which need to satisfy the corresponding wave equation.[85] The R-W model was later reformulated by Török and Varga[75] (T-V) for more general use when the electromagnetic waves are focused through a stratified medium with mismatched refractive indices. Haeberlé[82], [151] then demonstrated that such vectorial models could be used together with the G-L OPD, which provides an accurate and convenient way to model the PSF for optical microscopy. Therefore, we chose to simulate a fitting function for our experimental data with the T-V model using the G-L expression for OPD as a phase term.

4.2.1 Point spread function model for iSCAT imaging

The electric field at the observation space (focal region over the detector) can be expressed in the form of the R-W integral with the additional OPD term as follows[76], [89]

$$\vec{E}(\vec{r}) = -\frac{ik}{2\pi}\int_0^{2\pi}\int_0^{\theta_{\max}} \vec{E}_\infty(\theta_d, \phi) e^{ik\vec{s}\cdot\vec{r}} e^{ik\Lambda_{OPD}} f(\theta_d) \sin\theta_d \, \mathrm{d}\theta_d \, d\phi \,, \qquad (38)$$

where $\vec{E}_\infty(\theta_d, \phi)$ is the electric strength vector at the pupil of the imaging lens (far away from the focus of the lens, hence called 'far-field'), $\vec{s}$ the unit vector of field propagation, $\vec{r}$ the vector of the observation point, Λ_{OPD} the optic path difference responsible for spherical aberration, $f(\theta_d)$ the apodization factor, θ_d the zenith angle of the ray focused by the imaging lens, and $\theta_{d,max}$ the semi-aperture angle of θ_d. k is the wavenumber of the ray in the observation space, which is the same as the value in a vacuum. ϕ is the azimuthal angle in the optical system and defines the azimuthal direction of a ray. θ is the angle of a ray made with respect to the optic axis, and here it defines the polar direction of a ray in

the sample space (immersion oil), which is related to θ_d by the following equation: $n_i \sin\theta = M n_{\text{air}} \sin\theta_d$, where M is the magnification of the imaging system. The reference (E_R) and scattered (E_S) fields at the focal region of the imaging lens (over the detector) from the respective 'far-field' electric strength vectors are calculated using Eq. (38).

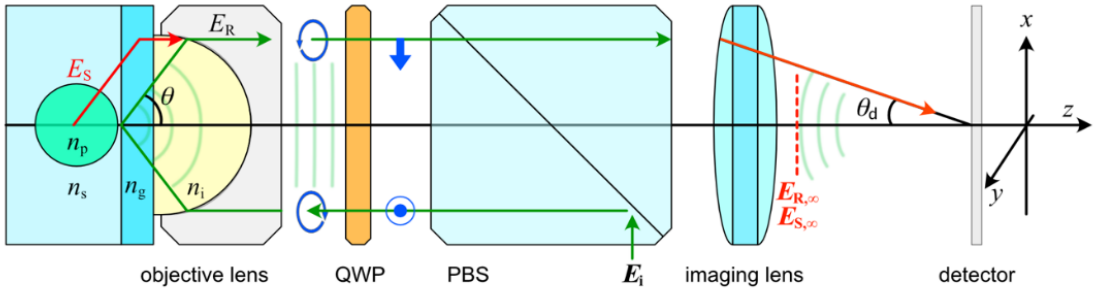

Figure 11: Illustration of the optical components of the iSCAT microscopy.[23]

To derive $\vec{E}_\infty(\theta_d, \phi)$ for reference and scattered fields, we start with a plane wave with linear polarization ($\vec{E}_i$) and trace the vectorial components of the reference and scattered electric fields by the generalized Jones matrix formalism, as illustrated in Figure 11.

A generalized Jones matrix describes the effect of an optical element on ray propagation. The system used in this work consists of a polarizing beam splitter (PBS), a quarter-wave plate (QWP), several lenses, and transmitting/reflecting interfaces for which the relevant Jones matrices are used.[87] The matrices were applied in order to trace the polarization state of light. It is considered that the incident beam impinges on the PBS. By the PBS, the beam becomes 45° linearly polarized with respect to the optic axis of the subsequent QWP and circularly polarized at the back focal plane of the objective by the QWP. The beam shines at the sample through the objective lens, and the reflected and scattered fields propagate all the way to the dotted line after the imaging lens as illustrated in Figure 11, passing through the objective lens, QWP, PBS, and the imaging lens. The R-W integral is then applied to those fields to find out the field at the focal region (detector).

Reference field: The reference field E_R is the light reflected at the glass and water/sample interface. The reference field at the pupil of the imaging lens ($\vec{E}_{R,\infty}$) is given as:

$$\begin{aligned}\vec{E}_{R,\infty}(\theta_d,\phi) = \mathbb{R}_z^{-1}(\phi)\cdot\mathbb{L}(\theta_d)\cdot\mathbb{R}_z(\phi)\cdot\mathbb{P}(0°)\cdot\mathbb{W}(90°,45°)\cdot\mathbb{R}_z^{-1}(\phi)\cdot\mathbb{F}_R \\ \cdot\mathbb{R}_z(\phi)\cdot\mathbb{W}(90°,45°)\cdot\mathbb{P}(90°)\cdot\vec{E}_i\,,\end{aligned} \tag{39}$$

where $\mathbb{P}(0°)$, $\mathbb{P}(90°)$, $\mathbb{W}(90°,45°)$, $\mathbb{R}_z(\phi)$, $\mathbb{L}(\theta_d)$, and $\mathbb{F}_R$ are the Jones matrices for polarizing beam splitters for transmission and reflection, quarter-wave plate, coordinates rotation by ϕ about the optic axis for local p-/s-wave decomposition, imaging lens with the zenith angle θ_d, and Fresnel field transformation by reflection, respectively. The incident field is given by $\vec{E}_i = (E_x, E_y) = (0,1)$.

The strength vector of the 'far-field' reference field can be expressed as follows:

$$\begin{aligned}\vec{E}_{R,\infty}(\theta_d,\phi) &= C_R\cdot i(r_p+r_s)\begin{bmatrix}-(1-\cos\theta_d)\cos\phi\sin\phi \\ \cos^2\phi+\sin^2\phi\cos\theta_d\end{bmatrix} \\ &= \frac{1}{2}C_R\cdot i(r_p+r_s)\begin{bmatrix}-(1-\cos\theta_d)\sin 2\phi \\ (1+\cos\theta_d)+(1-\cos\theta_d)\cos 2\phi\end{bmatrix},\end{aligned} \tag{40}$$

where C_R is just an overall numerical factor, r_p and r_s are the Fresnel reflection coefficients at the glass-water interface and the incident field ($\vec{E}_i$) is linearly polarized along the *x*-axis.

Scattered field: The strength vector of the scattered field by an NP is usually described by the Rayleigh scattering theory, which is only valid for particles smaller than the Rayleigh scattering limit. Thus, we consider the Mie theory[70] instead, for accurate modelling of the scattered field from NPs whose size is beyond the Rayleigh regime.

In this work, it is only considered scattering by a spherical particle. The scattered field by a spherical scatterer ($\vec{E}_s$) takes a complex form, as shown below. The scattered field at the pupil of the imaging lens ($\vec{E}_{S,\infty}$) is expressed in terms of $\vec{E}_s$ defined in local spherical coordinates:

$$\vec{E}_{S,\infty}(\theta_d,\phi) = \mathbb{R}_z^{-1}(\phi).\mathbb{L}(\theta_d).\mathbb{R}_z(\phi).\mathbb{P}(0°).\mathbb{W}(90°,45°).\mathbb{R}_z^{-1}(\phi).\mathbb{F}_T.\vec{E}_s\,, \tag{41}$$

where $\mathbb{F}_T$ is the Fresnel transmission matrix at the interface. If the incident field at the sample is circularly polarized, the scattered field given by $\vec{E}_S = \hat{\theta}E_{S\theta} + i\hat{\phi}E_{S\phi}$. $\vec{E}_S$ is described in terms of the spherical coordinates (r,θ,ϕ) defined in the sample chamber with the origin at the centre of the spherical particle. θ is the angle of a ray made with respect to the optic axis, and thus, it defines the polar direction of a ray in the sample space (immersion oil). The scattered field from a spherical scatterer is acquired by the Mie-scattering theory; $E_{S\theta}$ and $E_{S\phi}$, the polar and azimuthal components of the scattered electric field, respectively, shall be expanded as a linear combination of $\pi_n = \frac{P_n^1}{\sin\theta}$ and $\tau_n = \frac{dP_n^1}{d\theta}$

$$E_{S\theta} = \frac{1}{\sqrt{2}}\frac{e^{ikr}}{-ikr}e^{i\phi}S_2(\theta,\phi) \propto e^{i\phi}\sum\frac{2n+1}{n(n+1)}(a_n\tau_n + b_n\pi_n), \tag{42}$$

$$E_{S\phi} = \frac{1}{\sqrt{2}}\frac{e^{ikr}}{-ikr}e^{i\phi}S_1(\theta,\phi) \propto e^{i\phi}\sum\frac{2n+1}{n(n+1)}(a_n\pi_n + b_n\tau_n), \tag{43}$$

where S_1 and S_2 are some functions defined in terms of π_n and τ_n, and a_n and b_n are the coefficients of π_n and τ_n.[70]

The final form of the scattered field is simplified as follows:

$$\begin{aligned}\vec{E}_{S,\infty}(\theta_d,\phi) &= C_S \cdot i\left(S_2t_p + S_1t_s\right)\begin{bmatrix}-(1-\cos\theta_d)\cos\phi\sin\phi \\ \cos^2\phi + \sin^2\phi\cos\theta_d\end{bmatrix} \\ &= \frac{1}{2}C_S \cdot i\left(S_2t_p + S_1t_s\right)\begin{bmatrix}-(1-\cos\theta_d)\sin 2\phi \\ (1+\cos\theta_d) + (1-\cos\theta_d)\cos 2\phi\end{bmatrix},\end{aligned} \tag{44}$$

where t_p and t_s are Fresnel transmission coefficients at the glass and sample/water interface for p- and s-polarized light, and C_S is the overall numerical pre-factor including collection efficiency $\eta = (1/\pi)\sin^{-1}(\min(NA/n_s, 1))$ of the objective lens along the angular extent of aperture and S_1 and S_2 are functions of θ found in the scattering field components from a spherical particle obtained by the Mie theory.[70]

The electric field at the focal region of an imaging lens is calculated by the R-W integral, where $\vec{E}_{R,\infty}(\theta_d,\phi)$ and $\vec{E}_{S,\infty}(\theta_d,\phi)$ are inserted in Eq. (38) in the place of $\vec{E}_\infty(\theta_d,\phi)$ to get $\vec{E}_R$ and $\vec{E}_S$, respectively. As a ray propagates through a series of optical

systems, the (polar) angle made by the ray with respect to the optic axis changes. To compute the electric field via the R-W integral, the polar angle (θ_d) defined with respect to the focus of the imaging lens is converted to the polar angle (θ) defined with respect to the focus of the objective lens by using Snell's law and equation of magnification, $n_i \sin\theta = Mn_a \sin\theta_d$, where M is the effective magnification of a microscope.[86] For an imaging system with large M, $\sin\theta_d$ can be approximated to θ_d because the semi-aperture angle of the imaging lens in such a system is very small. Thus, the following angular relations are useful in the above equation: $d\theta_d = (n_i/M)\cos\theta\, d\theta$ and $\sin\theta_d\, d\theta_d = (n_i/M)^2(\sin 2\theta\,/2)d\theta$ where n_a is set to be 1.[152] In the microscope setup described in this work, the magnification of the objective lens is 62 if the tube lens with a focal length of 180 mm is used as recommended. In fact, a tube lens with a focal length of 500 mm was used and thus, the effective magnification of the microscope is 170.

$$\vec{E}(r) = -\frac{ik}{2\pi}\int_0^{\tilde{\theta}_{\max}}\int_0^{2\pi}\vec{E}_\infty(\theta_d,\phi)e^{ikz_d\cos\theta_d}e^{ikr\sin\theta_d\cos(\phi-\phi_d)}e^{ik\Lambda_{\mathrm{OPD}}}\sqrt{\frac{n_i\cos\theta_d}{n_a\cos\theta}}\left(\frac{n_i}{M}\right)^2\left(\frac{\sin 2\theta}{2}\right)\mathrm{d}\phi d\theta\,, \qquad (45)$$

where θ_{max} is the semi-aperture angle of θ and related to $\theta_{d,max}$ by $n_i \sin\tilde{\theta}_{\max} = Mn_a \sin\theta_{\max}$.

To simplify this integral, the azimuthal angle (ϕ) is integrated first by using the following relations:

$$\int_0^{2\pi}\cos n\phi\, e^{ix\cos(\phi-\varphi)}d\phi = 2\pi(i^n)J_n(x)\cos n\varphi\,, \qquad (46)$$

$$\int_0^{2\pi}\sin n\phi\, e^{ix\cos(\phi-\varphi)}d\phi = 2\pi(i^n)J_n(x)\sin n\varphi\,, \qquad (47)$$

The electric field is then simplified as follows:

$$\vec{E}(r) = -\frac{ik}{2}\left(\frac{n_i}{M}\right)^2\int_0^{\tilde{\theta}_{\max}}\vec{E}_a e^{ikz_d\cos\theta_d}e^{ik\Lambda_{\mathrm{OPD}}}\sqrt{\frac{n_i\cos\theta_d}{n_a\cos\theta}}\sin 2\theta d\theta\,, \qquad (48)$$

where the strength vectors $\vec{E}_a$ for reference and scattered fields are

$$\vec{E}_{a,\mathrm{ref}} = \frac{1}{2} C_R \cdot i\left(r_p + r_s\right) \begin{bmatrix} (1-\cos\theta_d) J_2(kr\sin\theta_d)\sin 2\phi_d \\ (1+\cos\theta_d) J_0(kr\sin\theta_d) - (1-\cos\theta_d) J_2(kr\sin\theta_d)\cos 2\phi_d \end{bmatrix}, \quad (49)$$

$$\vec{E}_{a,\mathrm{scat}} = \frac{1}{2} C_S \cdot i\left(S_2 t_p + S_1 t_s\right) \begin{bmatrix} (1-\cos\theta_d) J_2(kr\sin\theta_d)\sin 2\phi_d \\ (1+\cos\theta_d) J_0(kr\sin\theta_d) - (1-\cos\theta_d) J_2(kr\sin\theta_d)\cos 2\phi_d \end{bmatrix}, \quad (50)$$

where $\sin\theta_d = (1/M) n_i \sin\theta_i$ and $\cos\theta_d = \sqrt{1-(n_i \sin\theta\,/M)^2}$.

The iSCAT contrast depends on the phase difference between E_R and E_S, which is determined by the size and geometry of a scattering object, illumination wavelength, refractive index mismatch in the optical path, and NA.[24], [26], [27] The phase term, according to the G-L model, accounts for the aberration caused by index mismatch and finite thickness of multiple layers along the optical path.[83] The aberration can be described by considering the OPD (Λ) between the real (experimental) and ideal (design) beam paths (Eq. (11)), as illustrated in Figure 2 and modelled in Figure 12.[79], [83]

In the axial scan, the sample stage moves while the objective lens stays stationary, which results in changing the distance between the stage and the objective and therefore altering the thickness of the immersion oil layer. In that case, t_i should be expressed as in Eq. (13).[72], [79] Thus, the minimum point of the experimental axial profile is positioned at $z_f = 0$ as shown in Figure 12 (j).

To express the OPD in terms of the parameters of the relevant layers (immersion oil, cover glass, sample), Eq. (12) was used.

The OPD of the reference field ($\Lambda_{\mathrm{OPD,Ref}}$) is given by those of the normally incident and reflected rays with respect to ideal rays along the same path:

$$\Lambda_{\mathrm{OPD,Ref}} = 2\left(n_i t_i - n_i^* t_i^* + n_g t_g - n_g^* t_g^*\right). \quad (51)$$

The scattered field depends on the height of the dipole (centre position of the spherical scatterer) and thus the OPD of the field ($\Lambda_{\mathrm{OPD,Scat}}$) can be calculated using the ray geometry considered by the G-L formalism. The OPD of the scattered light is given as:

$$\Lambda_{\mathrm{OPD,Scat}} = \Lambda\left(\theta, z_f, z_p, \tau\right) + n_s z_p + n_i t_i - n_i^* t_i^* + n_g t_g - n_g^* t_g^*. \quad (52)$$

The reference (Eq. (40)) and scattered (Eq. (44)) fields are inserted in the R-W integral (Eq. (38)) with the aforementioned OPD terms and the integral is evaluated over Φ, which leads to the simplified form (Eq. (48-50)). Then, the iSCAT contrast is computed by subtracting the background from the signal and normalizing the difference with the background as:

$$I_{\text{sim}} = \frac{\left|\vec{E}_S\right|^2 + 2\left|\vec{E}_R\right|\left|\vec{E}_S\right|\cos\phi}{\left|\vec{E}_R\right|^2}. \tag{53}$$

To reproduce experimental results by computation, the reference field by reflection and the scattered field from a dielectric particle was calculated as a function of the relative position of the focal plane (z_f) and the axially stacked horizontal profiles of the reference and scattered fields (real part, phase, and amplitude) and of iSCAT (I_{sim}) were visualized in Figure 12 (b-h).

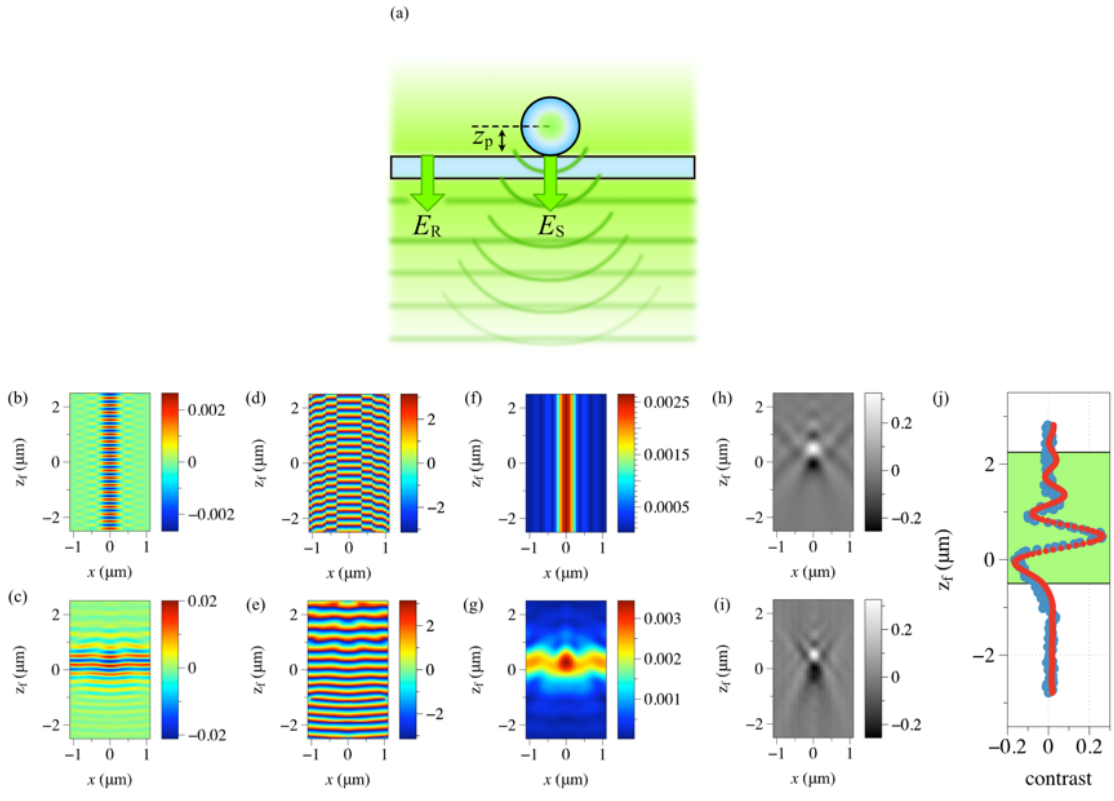

Figure 12: (a) Propagation of the scattered field (E_S*) from a nanoparticle and the reference field (*E_R*) from the sample-surface interface. (b-i) Images of axially (as a function of* z_f*) stacked horizontal profiles of various field quantities: (b-c) Real part of the electric field of (b) the reflected light* E_R *and (c) the scattered light* E_S*. (d-e) Phase of the electric field of (d) the reflected light* E_R *and (e) the scattered light* E_S*. (f-g) Amplitude of (f) the reflected light,* $|E_R|$ *and (g) the scattered light,* $|E_S|$*. (h-i) SHIP image of iSCAT PSF (h) by simulation and (i) by experimental measurement. (j) Axial intensity profiles at the center of a nanobead,* i.e. x = *0 (experimental: blue dots; simulation: red dots). The range of* z_f *used to compare the two profiles is shown in green.*[23]

As shown in Figure 12 (b-g), the reference and scattered fields propagate with the planar and quasi-spherical wavefronts, respectively. Moreover, the SHIP images and their axial cuts (axial variation of iSCAT signal at the centre of an NP) from the actual measurement and numerical computation look almost identical, as illustrated in Figure 12 (h) and (i). This analysis showed that it is possible to produce simulation results highly similar to experimental observations with only a specific set of parameters, indicating that the approach presented in this work is robust and reliable (Figure 12 (j)).

4.2.2 Strong dependence of dipole's iSCAT signal on its height

The interferometric signal between reference and scattered fields critically depends on the OPD variation, which originates from the axial location of the NP relative to the reference interface. Thus, the location of the scattering source would affect the shape of the wavefront and thus the spatial variation of the phase. It is well known that the incident field induces and drives the dipole moment in a dielectric nanoparticle. Therefore, the propagation of fields using the PSF model discussed above was simulated in order to understand how the height of the dipole, equivalently, the radius of the spherical NP affects the phase variation or the whole signal profiles. The numerical results as a function of the height of the dipole (z_p) are displayed in Figure 13 (a-c), together with the axial profiles for three representative values of z_p (0, 50, and 100 nm) shown in Figure 13 (d-f). As shown in Figure 13 (a) and (d), E_R has no dependence on the size of a nanoparticle as expected. On the contrary, the modulation of the scattered field slightly shifts along the axial direction (z_f) as z_p changes as shown in Figure 13 (e) (see inset). This phase shift is responsible for the axial variation of the iSCAT signal shown in Figure 13 (f) as well as in Figure 14 and Figure 15, which show that a small change in n_i influences the phase variation of E_S significantly, indicating that n_i needs to be precisely determined for accurate measurement of z_p.

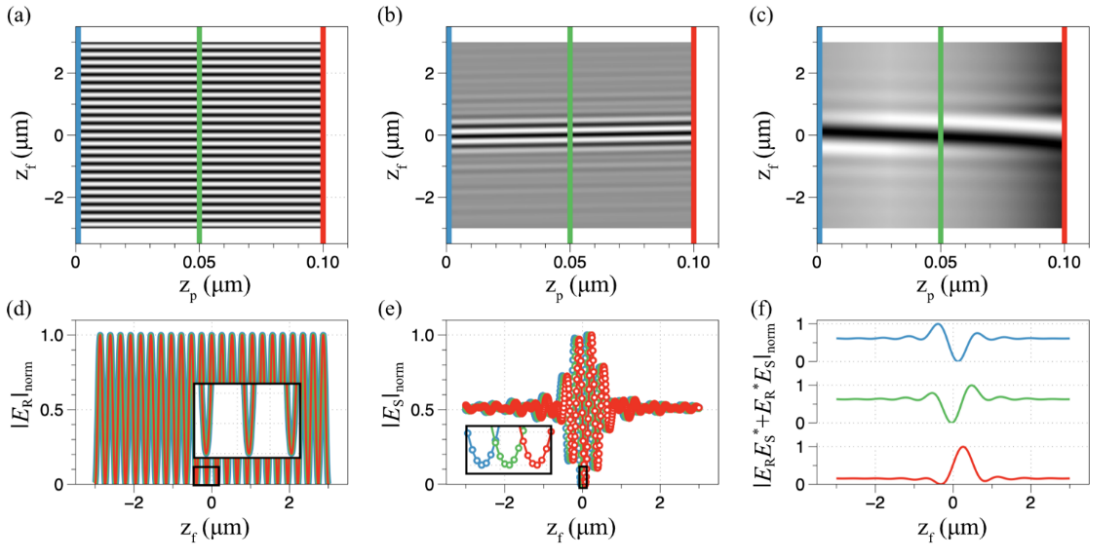

Figure 13: Stacked axial contrast profile as a function of z_p. (a) $|E_R|$, (b) $|E_S|$ and (c) $|E_R E_S^* + E_R^* E_S|$ calculated in the range of $z_p = 0 \sim 100$ nm with $n_i = 1.52$. All calculated values are normalized and scaled to fit to [0,1] and displayed in grey scale (hence, labelled as $|E_R|_{norm}$, $|E_S|_{norm}$, and $|E_R E_S^* + E_R^* E_S|_{norm}$ in (d-f), respectively). The blue, green and red coloured lines indicate $z_p = 0$, 50, and 100 nm. (d-f) Cross-sections of the reference field (d), the scattered field (e), and the interference term (f). Insets in (d) and (e) show the phase variation of the fields and highlight the sensitivity of the fields to different values of z_p. The axial intensity profile by the interference term exhibits more pronounced variation with z_p, accounting for sensitive detection of the size of nano-objects by iSCAT. In this figure, z_f is the computational input parameter before the offset (δz) is adjusted.[23]

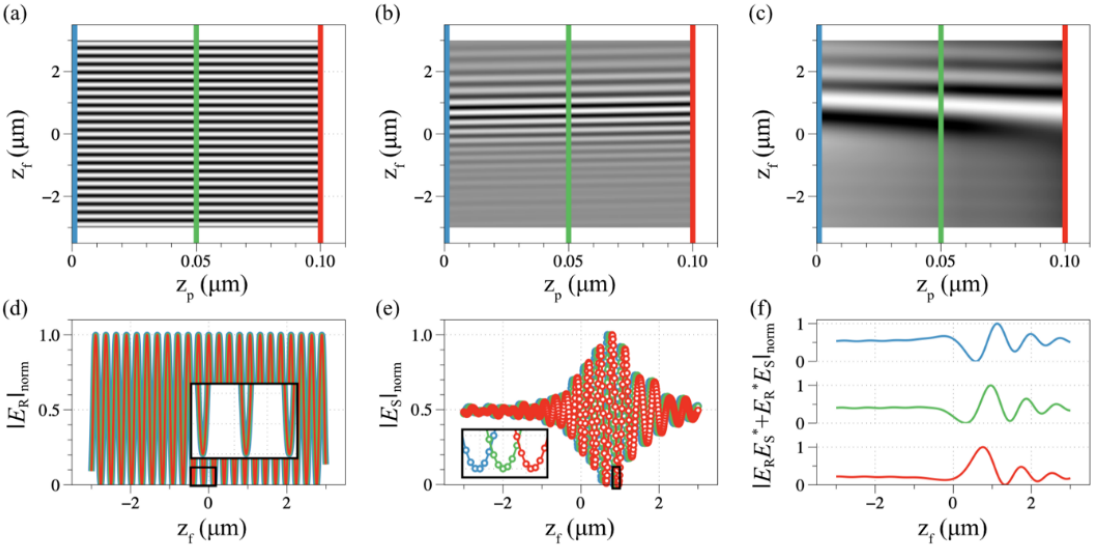

Figure 14: Simulations performed and results displayed identically to Figure 13 except for $n_i = 1.51$.[23]

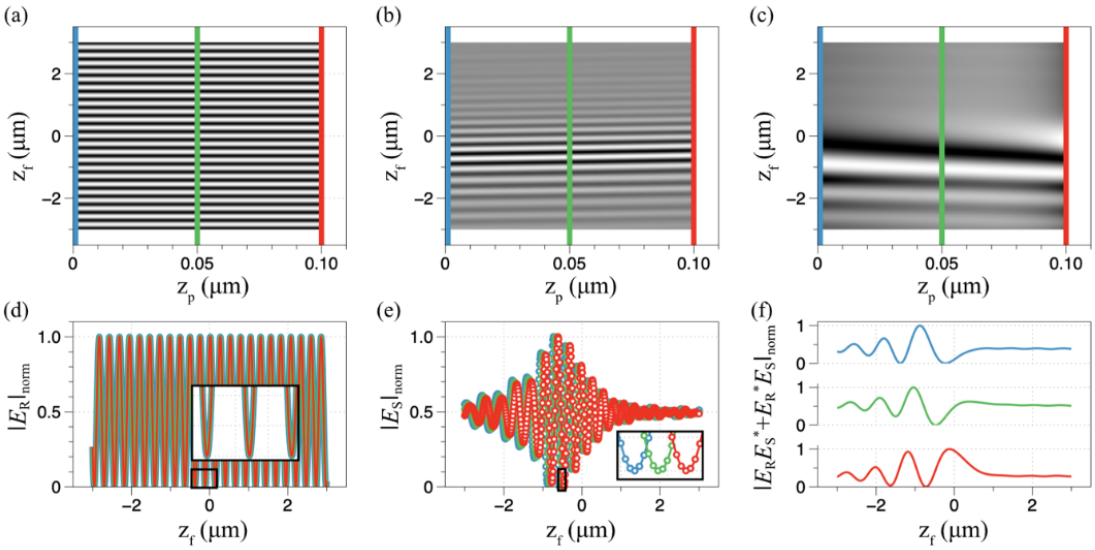

Figure 15: Simulations performed and results displayed identically to Figure 13 except for $n_i = 1.53$.[23]

Thus, a small change in z_p results in a notable change in the axial profile, which warrants a reliable and unambiguous analysis of experimental data. The scattering signal itself varies in amplitude, but due to its interference with the reference field, the change in the shape and amplitude of the interferometric signal becomes more pronounced. Therefore, the axial profile of the iSCAT signal significantly enhances the sensitivity to particle size. It becomes clear that our approach based on the quantitative fitting analysis of the axial pattern of the iSCAT signal can be an incisive tool for distinguishing NPs with different sizes.

4.2.3 Reconstruction of axial PSF variation

The realistic model and accurate fitting of experimental data can be achieved only with fitting parameters close to reality. In the computation of PSF, the wavelength of illumination and the NA used were 532 nm and 1.35, respectively. The refractive indexes and thicknesses used were: n_s = 1.33 (for water), n_p = 1.59 (for polystyrene and latex nanoparticles) or 2.4 (for nano-diamond particles), $n_g = n_g^* = 1.52$ (for cover glass), $n_i^* = 1.52$ (for immersion oil), $t_g = t_g^* = 170$ µm (for cover glass), and $t_i^* = 100$ µm (for immersion oil). Symbols with and without asterisk represent parameters in real (experimental) and ideal (design) conditions as used in the G-L model (Eq. (12), (13)).[79] The t_i, 'real' parameter of oil thickness, is a parameter to be adjusted in the G-L model.

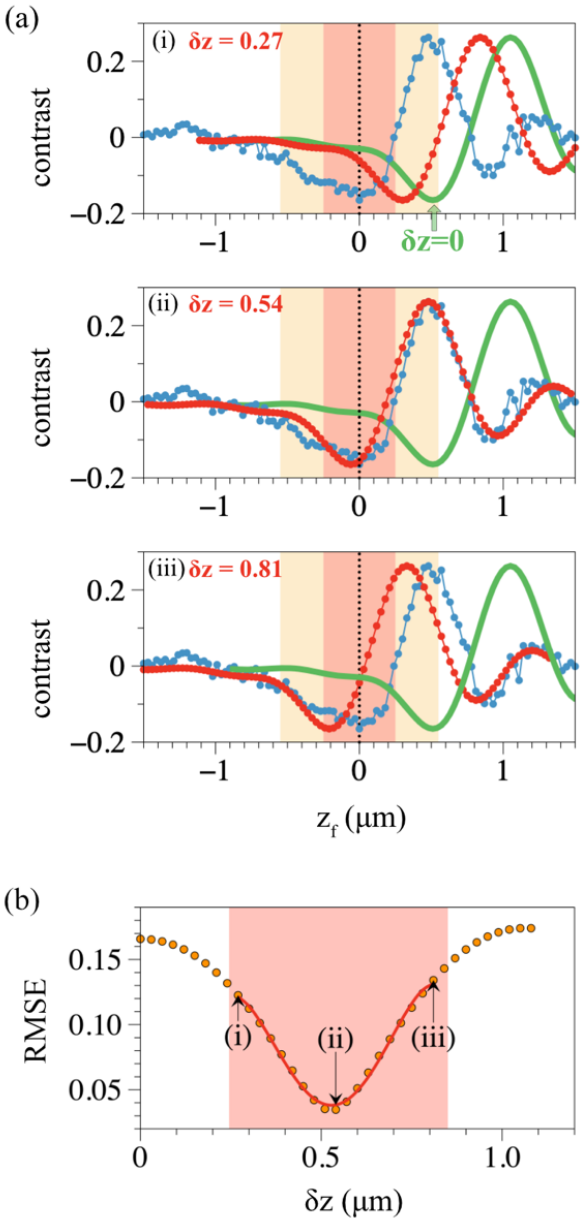

Figure 16: Root-mean-squared-error (RMSE) estimation to find the best theoretical axial intensity profile (I_{sim}) with a given set of n_i and z_p as a function of the relative focal position (z) that matches the experimental (I_{exp}) profile with the highest similarity. (a) Demonstration of the profile matching procedure via translation of the simulated profile (I_{sim}) along z_f by δz. The RMSE value is computed from I_{exp} (blue line with dots) and I_{sim} (red line with dots) over the shaded region with good overlap. (b) RMSE values as a function of δz, which is the offset applied to I_{sim}. Once the value of δz to yield the least RMSE is found, the offset is denoted as δz. (i) δz = 0.27 μm, (ii) δz = 0.54 μm = δz*, and (iii) δz = 0.81 μm with respect to the δz = 0 μm (green solid line in (a)). We fitted the RMSE values to a 4th polynomial function to determine the representative RMSE for the given set of n_i an z_p.*[23]

Parameters n_i and z_p were varied to describe the spherical aberration in the axial profile. Numerical values of these fitting parameters were determined by the root mean square error (RMSE) evaluation. First, the parameter space for n_i and z_p was defined. For each set of n_i and z_p values, the PSF (equivalently, I_{exp}) at the focal space of the imaging lens (equivalently, on the detector surface) with various depths of the focal plane of the

objective (*i.e.*, z_f in Eq. (13) or z in the definition of z_f) was generated from the R-W integral in Eq. (38, 45, 48-50). Typically, z was varied within a few μm from $z = 0$. Since only the centre value $I_{exp}(x_0,y_0)$ was of interest, it is possible to get the axial profile of the centre of the PSF by setting $r = 0$ in the R-W integral. This simulated PSF (I_{sim}) is likely to be off with respect to I_{exp} due to the non-ideal experimental parameters (causing spherical aberration) and the finite size of scatterers, thus I_{sim} was shifted by δz to find the optimal I_{sim} with the lowest RMSE for the given n_i and z_p by compensating for a potential offset (the compensating offset giving the least RMSE is denoted as δz^*). By sequentially varying δz (distance translated for I_{sim} with respect to I_{exp} as illustrated in Figure 16 (a)) with a fine increment within a reasonable range, one would find the least RMSE with the best δz^* (Figure 16 (b)) and obtain I_{sim} that best matches I_{exp} under the given set of n_i and z_p. This least RMSE is called the representative RMSE value for the given n_i and z_p.

4.3 Determination of nanoparticle size by axial profiling of the PSF

The RMSE estimation was carried out for axial intensity profiles generated with various values of n_i and z_p as shown in Figure 17 (a). From the minimization of RMSE, it was possible to determine the values of n_i and z_p as shown in Figure 17 (b). To validate this approach, polystyrene (PS) and latex beads were tested because they are highly uniform in size and shape (spherical), not to mention that they are homogeneous.

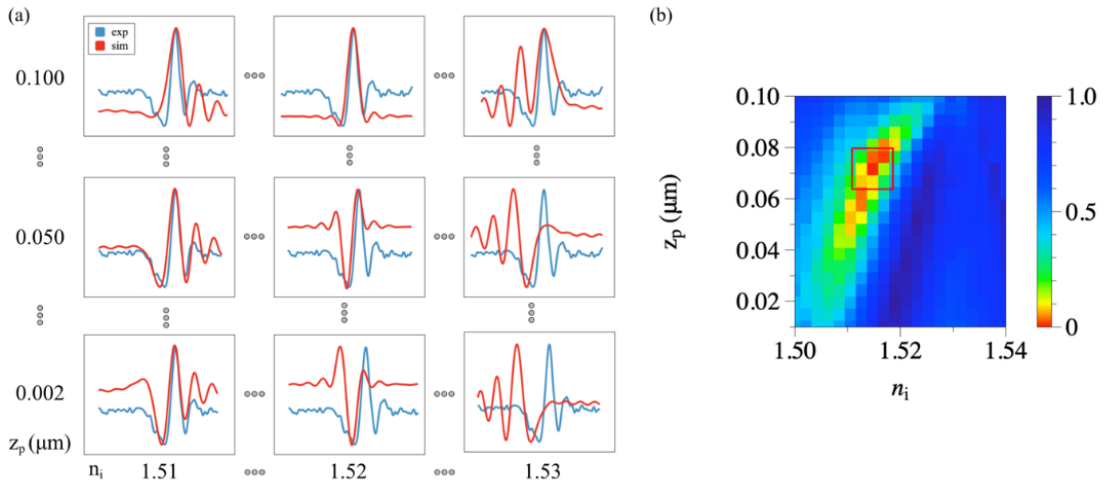

Figure 17: RMSE estimation to determine the model parameters, n_i and z_p for a 60-nm latex bead. (a) Illustration of the parameter-finding procedure by minimizing the RMSE between the measured axial contrast profile (blue line: experimental) and the computed axial contrast profile over the whole parameter space of n_i and z_p (red line: simulated). (b) Pseudo-colour maps of RMSE re-scaled to fit to [0,1] for various n_i and z_p. The minimum RMSE marked by a red box represents the best fit of the PSF modelling for the measured axial contrast profile. The n_i and z_p at the minimum RMSE are used as the parameters to generate the PSF with the highest similarity.[23]

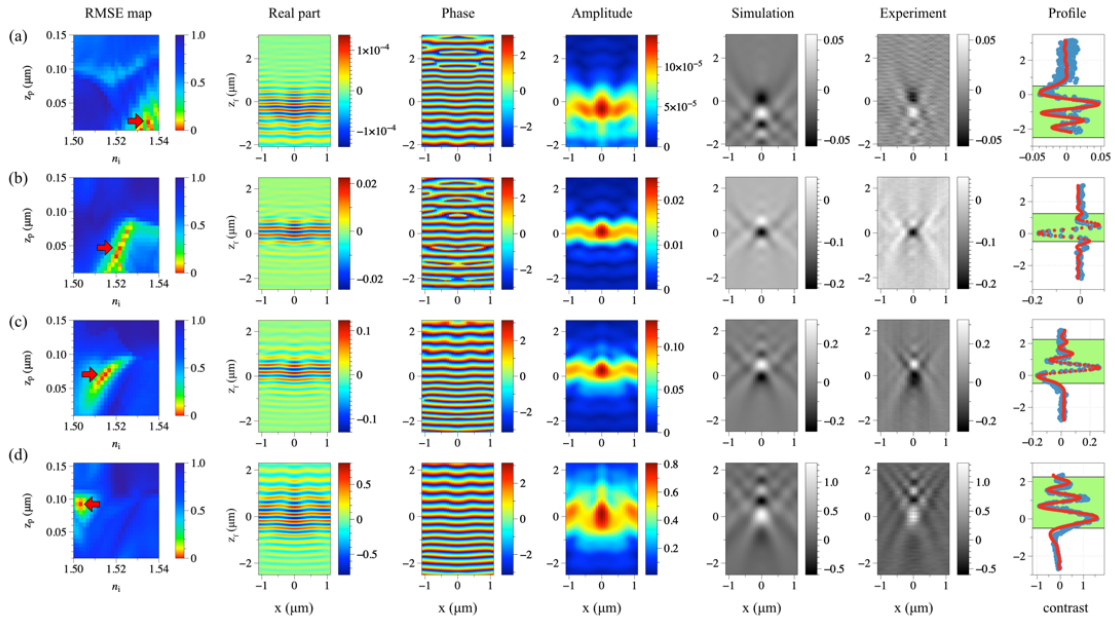

Figure 18: Representative results of PSF modelling analysis for different-sized dielectric nanoparticles ((a) R_{nom} = 20 nm, (b) 50 nm, (c) 60 nm, and (d) 100 nm). First column: The RMSE map shows the representative RMSE values for the whole parameter space of n_i *and* z_p*, trying to find the best fit (marked by a red arrow). Second column: Real part of the electric field of the scattered light,* E_S*. Third column: Phase of the electric field of the scattered light,* E_S*. Fourth column: Amplitude of the scattered light,* $|E_S|$*. The SHIP images, one by simulation (fifth column) and one by experiment (sixth column) with the best parameter values [(a)* (n_i, z_p) *= (1.538, 0.022 μm), (b)* (n_i, z_p) *= (1.519, 0.039 μm), (c)* (n_i, z_p) *= (1.515, 0.052 μm), (d)* (n_i, z_p) *= (1.503, 0.093 μm) with design parameters* $(n_s, n_p, n_i^*, n_g^*, t_i^*, t_g^*)$ *= (1.33, 1.59, 1.52, 1.52, 100 μm, 170 μm)], exhibit clear similarity, indicating the reliability of the parameters obtained here. The axial contrast profile in the seventh column shows the best simulation curve (red line with dots) for each experimental curve (blue line with dots). Green highlighted area defines the iSCAT features for final fitting and error calculation.*[23]

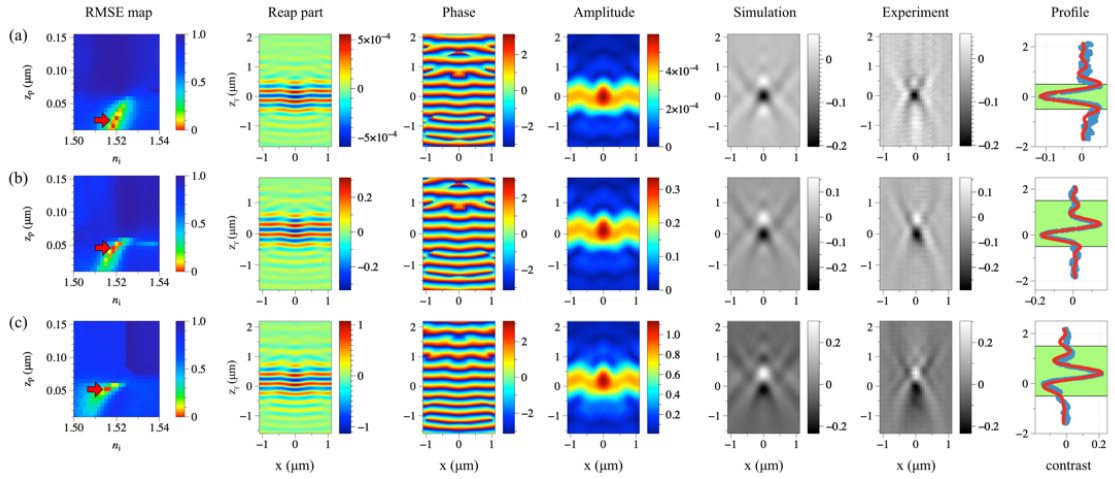

Figure 19: Representative results of PSF modelling analysis for different-sized fluorescent nanodiamonds (fND) particles from the same product number (900172, Sigma-Aldrich). This figure is presented in the same manner as Figure S7. First column: The RMSE map shows the representative RMSE values for the whole parameter space of n_i *and* z_p*, trying to find the best fit (marked by a red arrow). Second column: Real part of the electric field of the scattered light,* E_S*. Third column: Phase of the electric field of the scattered light,* E_S*. Fourth column: Amplitude of the scattered light,* $|E_S|$*. The SHIP images, one by simulation (fifth column) and one by experiment (sixth column) with the best parameter values [(a)* (n_i, z_p) *= (1.521, 0.012 μm), (b)* (n_i, z_p) *= (1.518, 0.045 μm), (c)* (n_i, z_p) *= (1.516, 0.055 μm), with design parameters* $(n_s, n_p, n_i^*, n_g^*, t_i^*, t_g^*)$ *= (1.33, 2.4, 1.52, 1.52, 100 μm, 170 μm)], exhibit clear similarity, indicating the reliability of the parameters obtained here. It is also notable that the size of fND is highly heterogeneous. The axial contrast profile in the seventh column shows the best simulation curve (red line with dots) for each experimental curve (blue line with dots). Green highlighted area defines the iSCAT features for final fitting and error calculation.*[23]

Using the PSF model and adjusting the parameters carefully, it was possible to make the computational results nearly identical to the corresponding experimental data: the experimental and theoretical SHIP images are remarkably similar for different-sized beads as shown in Figure 18. The size uniformity of beads was confirmed by our NTA and TEM measurements shown in Figure 20 (a-c). Interestingly, the results from those NPs showed that z_p determined by our method is in excellent agreement with the expected radius of those NPs. From the model fitting, the sizes of PS and latex beads were obtained, which closely match their R_{nom}'s in Figure 21 (a): (i) for 20-nm PS beads, z_p ~ 17 (± 7) nm; for this PS bead, the NTA method failed to give reasonable results because it is substantially smaller than the size limit for reliable measurements by NTA (dia. ~ 60 nm with 642 nm excitation)[153] but TEM provided R ~ 23(± 2.8) nm, consistent with the result from the PSF modelling; (ii) for 50-nm latex beads, we got z_p ~ 40 (± 1.2) nm while NTA and TEM gave R ~ 50 (± 18) nm and ~ 50 (± 3.2) nm, respectively, both supporting the result from PSF modelling; (iii) for 60-nm latex beads, we got z_p ~ 56 (± 10) nm while NTA and TEM gave R ~ 55 (± 21) nm and ~ 61 (± 2.5) nm, respectively, supporting the result from PSF modelling again; (iv) for 100-nm PS beads, we got z_p ~ 93 (± 10) nm while NTA gave R ~ 102 (± 20) nm, supporting the result from PSF modelling. As shown here, TEM is a reliable and accurate tool to measure the size of NP by direct visualization, but the limited accessibility of TEM and the low throughput and technical difficulty of the technique hampers easy and wide applications to samples in the condensed phases. This dipole-modelling-based result is consistent with our view that the dipole of those scatterers is located near the centre of the particles and the particles are in good contact with the interface.

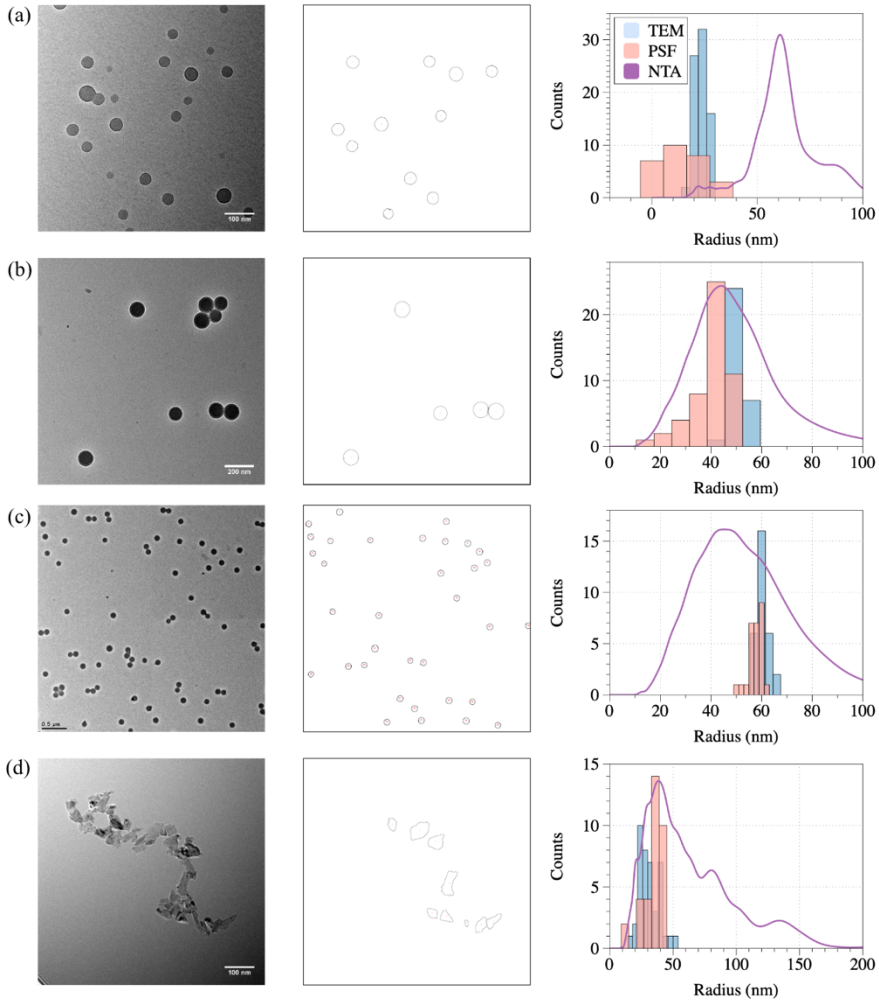

Figure 20: (First column) Representative TEM images that were analysed to obtain the size of PS (a), latex ((b) and (c)) and fND (d) particles. (Second column) Outlines of detected particles used for calculation of the Feret diameter. (Third column) Histograms of size of particles measured by different techniques (TEM, PSF (iSCAT), and NTA analysis – see graph legend in (a)). Nominal radius (R_{nom}): (a) 20 nm PS beads, (b) 50 nm latex beads, (c) 60 nm latex beads, and (d) 40 nm for commercial fNDs. Radius deduced from TEM images was obtained by measuring the Feret diameter. Scale bar: (a) 100 nm, (b) 200 nm, (c) 500 nm, (d) 100 nm.[23]

Next, the size of fND was estimated using the PSF model. fNDs have drawn much attention for their remarkable properties and wide applications in biological imaging and sensing.[154], [155] Theoretical SHIPs of fNDs with carefully adjusted parameters were generated, which are in good agreement with the experimental SHIPs as shown in Figure 19. The measured sizes (z_p) of fNDs were broadly distributed, as shown in Figure 21(b), consistent with the TEM result shown in Figure 20 (d). It, however, turned out that the size of an fND estimated by our approach was correlated with the fluorescence intensity of the fND. This issue is discussed in the next section.

Although NTA is a well-known and popular tool for size determination of NPs, it has several technical pitfalls,[156] which the method presented here could overcome. First, the size distribution measured by NTA was considerably broader than that acquired by

this work's axial profile-fitting method. It is likely because the single-particle method presented here enables us to choose individual NPs and avoid clusters, significantly larger NPs, and impurities in the sample, which is intrinsically impossible with the NTA method. Second, the NTA is less straightforward in measuring the size of small NPs because instrumental settings and user inputs are critical for such NPs. While NTA could be of some use for measuring NPs of size below 60 nm, the uncertainty would be large, as exhibited in Figure 20. In contrast, the sensitivity of this method is high, so the presented approach enables accurate measurements of the size of PS beads as small as R=20 nm and that of fNDs down to 15 nm in radius (Figure 21). Although several potentially useful methods have been recently developed such as iNTA that combines the advantages of NTA and iSCAT[157] and holoNTA that uses holographic imaging for larger sample volume and higher sensitivity,[158] they have not been commonly used yet.

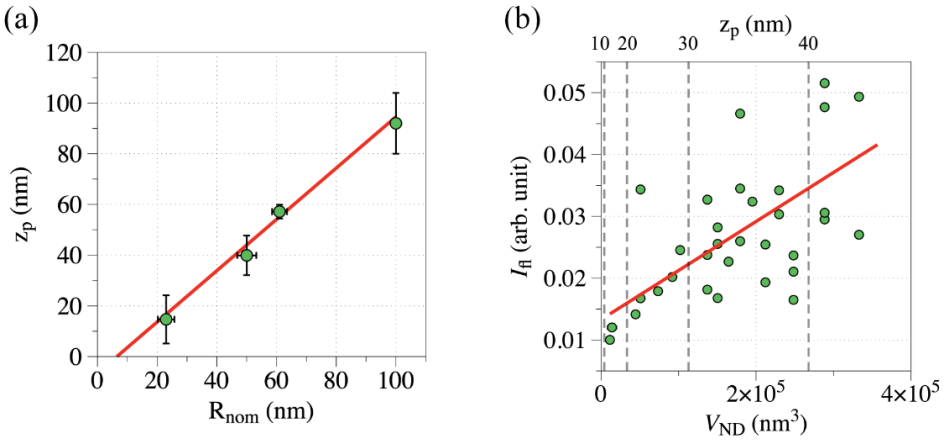

Figure 21: Representative results of particle size determination by PSF analysis. (a) Accuracy of the axial profile method to determine the size of spherical nanoparticles (PS and latex bead). z_p, radius of bead acquired by the axial profile method, is not only linearly correlated with but also nearly identical to 'Nominal radius (R_{nom})' provided by manufacturers. Linear fit $y = 1.0114 \cdot x - 6.657$. (b) Correlation of the fluorescence intensity (I_{fl}) and volume (V_{ND}) of '40 nm' fND together with a linear fit of the data. For a better idea about the fND size, the upper x-axis shows the value of z_p determined by iSCAT. Several values of z_p are indicated by vertical dashed lines. Correlation coefficient: $\rho(V_{fl},V_{ND})_{40}=0.57$.[23]

4.4 Correlation of fND volume and fluorescence intensity

fNDs are fluorescent owing to the negatively charged NV^- centres in their diamond lattice. The fluorescence intensity I_{fl} is proportional to the number of NV^- centres in a given fND. From $N_{NV} = c_{NV} \cdot V_{ND}$ (c_{NV}: concentration of NV^- centres, V_{ND}: volume of fND), the fluorescence intensity should also increase linearly with the volume of fND. Regarding the correlation between them, we shall consider the following degrading factors: (i) inhomogeneous incorporation of NV^- centres throughout nanodiamond lattice, (ii) the inaccurate assumption that the fNDs have a spherical shape, in fact, our fNDs appear

significantly jagged as confirmed by TEM (Figure 20 (d)), (iii) weaker fluorescence emission by NV^- centres placed near the particle surface than in the centre of the particle,[159] and (iv) batch-to-batch variation of the number of NV^- centres in the fabrication process.

Figure 21 (b) shows the relationship between the volume of fND, V_{ND}, calculated from its radius, z_p, determined by iSCAT, and the fluorescence intensity I_{fl} of fND. To describe the correlation between the fluorescence intensity and fND volume, the Pearson correlation coefficient was used and the correlation $\mathcal{R}(V_{fl},V_{ND})_{40} = 0.57$ was obtained, which signifies only a moderate correlation. There are several particles that deviate considerably from this correlation. The main reasons for scattered points would be, as assumed above, non-uniform incorporation of NV^- centres in the diamond lattice and the non-spherical shape of the nanoparticles. This implies that the size of fNDs cannot be deduced accurately from their fluorescence intensity alone. On the other hand, it was found that the distributions of fND size obtained by different methods (PSF, TEM, NTA) were well overlapped, supporting that the value of z_p (or the size of NP) acquired by the PSF model analysis is valid. From this, it can be assumed that the PSF analysis proposed here can even determine the size of NPs of non-spherical shape such as fNDs with reasonable accuracy.

4.5 Conclusions

The iSCAT microscopy has evolved into a useful label-free optical technique that enables both imaging and tracking nanoscopic objects with high precision. Here, it was demonstrated that it could be used to characterize the size of NPs all-optically even beyond the Rayleigh scattering regime. A technique useful to measure the size of individual NPs by acquiring the axial variation of the iSCAT signal and fitting the theoretical PSF model to the axial profile of the iSCAT signal was developed, which provides the information on the scattering dipole position, *i.e.*, size of NPs in the present case.

The theoretical model used to fit the experimental data is a modified Török and Varga's vectorial PSF theory. This model accounts well for the factors that contribute to the iSCAT signal resulting from the interference between the scattered and reference fields. The developed method turns out to be sensitive to small changes (within a few nanometres) in the size of NPs, which surpasses other optical methods such as NTA or

DLS (Dynamic Light Scattering) in size sensitivity and single-particle characterization capability, not just ensemble size distribution. It also stands out amongst other size determination techniques for its instrumental simplicity and all-optical, contactless, non-destructive, and non-contaminating approach. The results presented here demonstrate that the axial profile-fitting method is a useful approach not only because it can be used to measure the size of NP covering a broader range from ~ 10 nm to several hundred nanometres, well-beyond Rayleigh scattering limit[21], [22] but also because it can be applied to NPs made of various materials. All taken together, it is anticipated that the technique presented in this work would be useful for characterizing NPs and stratified media.

5 Nanodiamonds for cellular imaging in iSCAT microscopy

5.1 Introduction

As a fully optical microscopic method with resolution reaching under the diffraction limit, iSCAT has a lot of potential in life cell imaging and SPT. When using iSCAT in bioimaging, there is no need for fluorescent dyes and there are almost no limitations on duration of the imaging. iSCAT offers to monitor both the probe or the object of interest and the surrounding environment at the same time. Using suitable filtering method, it is possible to obtain many information from only one data set.

In this study, the fluorescence combined iSCAT microscopy is used for SPT of fNDs in living cells to study their interaction. Particularly, it is of interest to establish a universal method to monitor fNDs of various sizes through different stages of nanoparticle-cell interaction and uncover different cell behaviour depending on nanoparticle size using that method.

The following chapters introduce SPT of fNDs in living cells from 100 nm down to 10 nm size. The differences of cell-fND behaviour between 100 nm and 10 nm fNDs are studied at different stages of their interaction. Specifically, interaction with plasma membrane, diffusion in cell cytosol and interaction with the nucleus were investigated.

Fluorescent nanodiamonds were chosen as highly suitable probe for imaging nanoparticle interaction with living cells with iSCAT. As diamond has high index of refraction, even very small particles are good scatterers and easier to detect with iSCAT technique. Especially when imaging nanoparticles in a busy and complex environment like living cell, it is important to distinguish the probe well. For complete unambiguity, fluorescence imaging was used as a reference to iSCAT to confirm the fNDs location.

5.2 Imaging nanodiamonds in cells

The iSCAT image reflects diffraction patterns of every shape and surface in the cell hence the image can appear very busy at times and 3D movement of the nanoparticle can be challenging to detect. However, by using highly refractive fNDs in combination with fluorescence detection it was possible to detect fNDs from 100 nm down to 10 nm size.

Figure 22 and Figure 23 are examples of fNDs inside the U2OS cell. The left side of the images is iSCAT image and the right side is the corresponding area detected simultaneously by fluorescence channel. Figure 22 is an image with ~100 nm fND and

Figure 23 image contains ~10 nm fND. It is apparent that the 100 nm fND is very clear in both iSCAT and fluorescence image and 10 nm fND not as much, yet both are detectable and traceable. The fluorescence channel with 10 nm fND shows a lot of background noise which is caused by high illumination power needed to detect a fluorescence from such small particle with week fluorescence. The dependence of size and iSCAT strength and fluorescence intensity was already discussed in previous chapter.

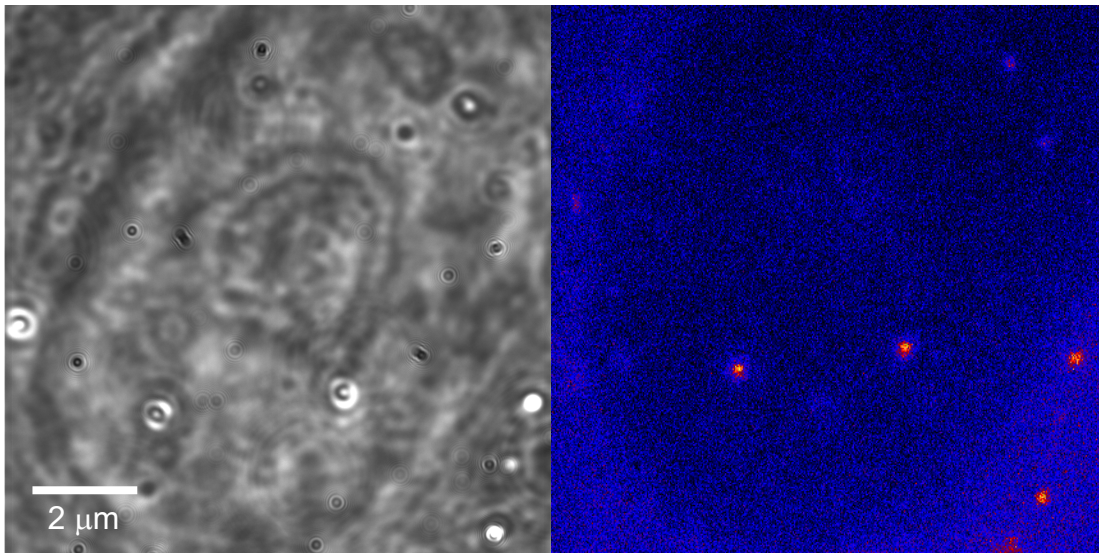

Figure 22: U2OS cell with internalized 100 nm fNDs imaged by iSCAT (left), and fluorescence detection (right), the cell nucleus area taking up most of the image is distinguished by darker fringe outline in iSCAT image and by less fluorescent area in fluorescence image.[160]

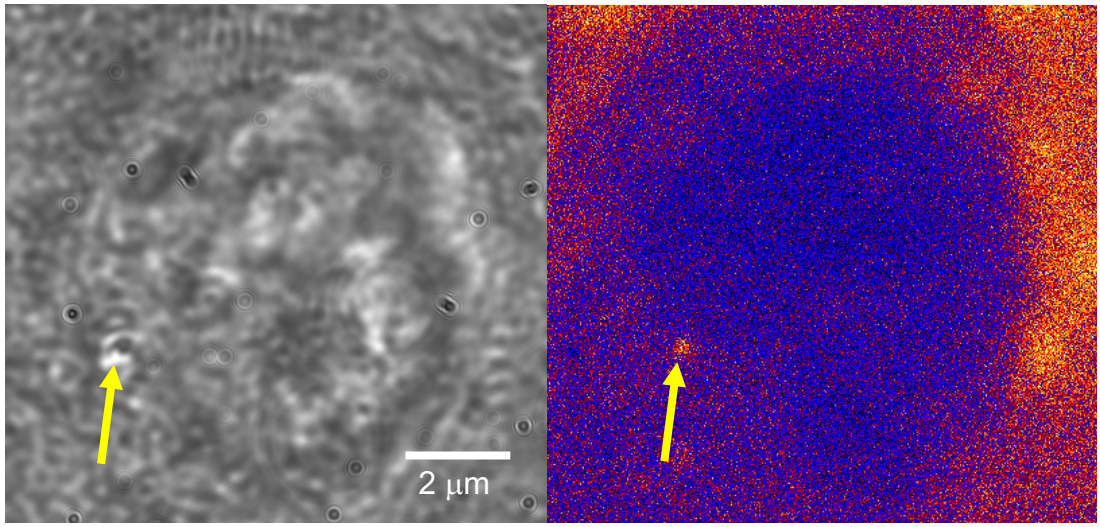

Figure 23: U2OS cell with internalized 10 nm fND (marked by yellow arrow) imaged by iSCAT (left), and fluorescence detection (right), the cell nucleus can be distinguished by darker fringe outline in iSCAT image and by less fluorescent area in fluorescence image.

The excitation wavelength was 532 nm and the detection window was defined by emission filter to be 540 – 600 nm for the fluorescence channel. In this range of

wavelengths, we are able to detect the emitted signal of fND well while minimum fluorescence from the living cell is coming through. However, we are still detecting a weak fluorescence from some cell proteins at cytoplasm. The cell nucleus is free of any fluorescence hence it is clearly visible in each image as the darkest area. On the other hand, in iSCAT image, we can distinguish more structures and their clear boundaries (Figure 24) such as nucleus, nucleolus, endoplasmic reticulum, cytoskeleton[66] or vesicles. Some studies also aim to image Golgi apparatus or mitochondria.[65] Especially in the case of imaging ~10 nm fNDs, the fluorescence reference image comes in handy when distinguishing the fND from natural cell vesicles since their iSCAT image can look almost identical.

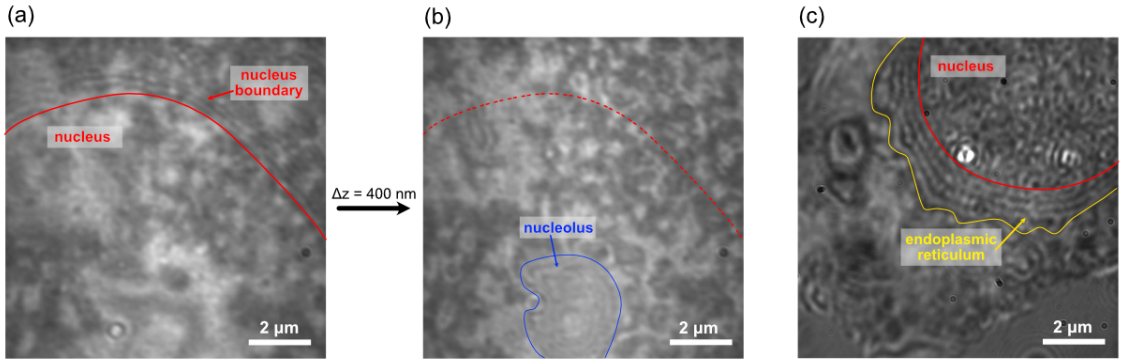

Figure 24: Cell structures visible by iSCAT: (a) upper surface of U2OS cell with visible fringe bordering the nucleus, (b) internal structure of the same cell with focus at nucleolus, (c) internal structure of another U2OS cell with endoplasmic reticulum surrounding nucleus. The focus difference between (a) and (b) is 400 nm. The bright scattering spots in (c) are internalized 10 nm fNDs.

Figure 24 is example of U2OS cell with some visible structures. Figure 24 (a) and (b) are images of the same cell captured at different heights with difference 400 nm. Image (a) is captured at the upper surface of the cell where the nucleus boundary is recognized by diffraction fringe signalizing steeper slope of the cell surface. When the focus is moved down closer to the cover glass, the internal structures appear more clearly a we can observe nucleolus in the image (b). In Figure 24 (a), the nucleus is clearly visible at the top right quarter of the image. When focused inside the cell, the nucleus always appears as the part of the cell with the densest structure in iSCAT. Around the nucleus border, endoplasmic reticulum is well visible in this image. The border of the cell can be seen at the bottom right of the image. The smooth areas are the surface of the culture dish.

5.3 Assessment of ideal duration of incubation before observation

At first, the ideal time of cell incubation together with fNDs was tested. Several criteria had to be considered (i) cell density, (ii) amount of internalized fNDs, and (iii) vitality of cells. It was important to find a good balance between said criteria to reach the best quality of data later. The cells density had to be sufficiently high to be easily find cells with the iSCAT microscope which had very small (40 x 40 μm) observation area while the cells had to be spread in one layer and not overlap each other. Next, for observing the interaction of cells and fNDs it was required that some fNDs are already internalized inside the cell or right before internalization. Maximum number of internalized fNDs was ten, higher number already caused difficult observation of separate nanoparticles and their behaviour, overlapping signals and disturbances inside the cell. Too many internalized fNDs can have effect on cell vitality as well as too long incubation in general. Too long incubation could also result in fNDs being already excreted by cells after their uptake.

The cell culture medium containing freely diffused fNDs was taken out and replaced with fresh medium free of fNDs to ensure that the observed fNDs were internalized. The confocal image was captured as a 3D stack where the fNDs were observed only in areas inside the cells (Figure 25). This was later supported by iSCAT imaging, where the position of the fND can be determined more precisely due to better axial resolution of iSCAT than that of a confocal microscope, making it simpler to determine whether the focus is above the cell, on its surface, or inside the cell.

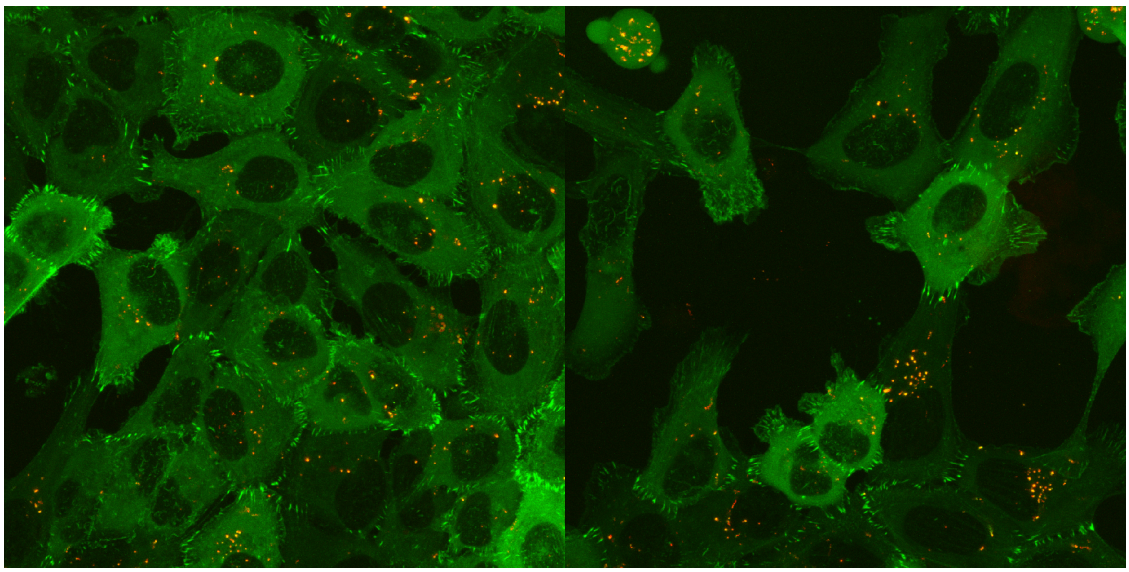

Figure 25: Fluorescence confocal microscope image of cells labelled by GFP and cultured together with fNDs after 1 day of incubation.

The incubation times initially tested were 1, 2, 3 and 4 days. After set time of incubation, the culture medium with fNDs was exchanged for new medium without fNDs so that no more fNDs interact with cells during evaluation. The evaluation was performed on fluorescence confocal microscope. The cells were also labelled with GFP (green fluorescent protein) for this particular evaluation.

It is the best to observe fND after 1 day of incubation – fND is mostly internalized and travels inside the cells

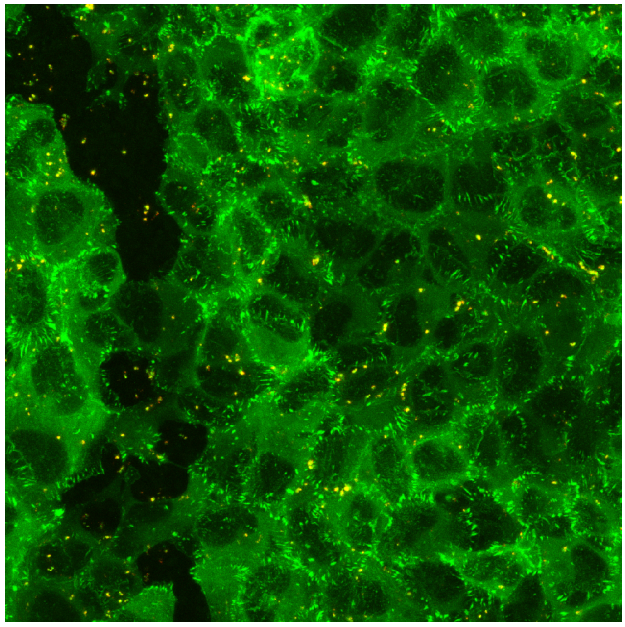

Figure 26: Fluorescence confocal microscope image of cells cultured together with fNDs after 4 days of incubation.

The duration of incubation considering the cell density, internalized fNDs and cell vitality gave the best results after one day. The state of the sample after 24 hours of incubation is shown in Figure 25. After more than 1 day the cells were usually overgrown overlapping each other. On the fourth day of incubation the cells were stacked in multiple layers and most of the fNDs were very clustered inside the cells or excreted out of the cells together with some debris. The sample incubated for four days is shown in Figure 26 for comparison.

5.4 Internalization rate of fND

As a next step, the internalization rate of fNDs was observed more closely. The initial incubation time test showed that internalization of the first fNDs occurs in a range of first few hours of introducing the fNDs into the cell media. Hence the internalization rate was studied more closely with shorter time range.

First, the test was carried out with uncoated 100 nm fNDs in U2OS cells as it is the target material in this study. The number of internalized fNDs was observed under the iSCAT microscope. Before each evaluation, the medium surrounding the cells was exchanged for a new medium to remove non-internalized fNDs from the sample. Then, twenty cells throughout the sample were evaluated for each incubation time. The number of internalized fNDs was counted in each individual cell.

The check-up after one and two hours showed no internalized fNDs yet. First internalized fNDs were found after three hours of incubation. The next evaluation was carried out every hour until six hours and then after one day. The internalized fND counts are in Table 1 and the data are visualized in Figure 27. There is a first peak visible after five hours of incubation and after six hours the number of internalized fNDs decreased. This indicates that after six hours the first fNDs were excreted from the cells. Although the internalization rate kept increasing, meaning the internalization was faster than excretion, the slope after six hours was slower due to fND excretion. This effect was observed repeatedly when carrying out this experiment.

The same experiment was carried out with 100 nm fNDs coated with PEG (PEG-fND) which was reported to accelerate the internalization rate[127]. The internalized PEG-fND count is in Table 2 and the data are visualized in Figure 28. The internalization occurred earlier as expected. The first internalized particles were detected after two hours of incubation. Interestingly, the first excretion of PEG-fNDs also transpired after six hours as for bare fNDs. However, the number of internalized PEG-fNDs was significantly higher than in case of bare fNDs.

Table 1: Number of bare 100 nm fNDs internalized after stated incubation times.

Incubation time (h)	3	4	5	6	24
Number of fNDs per cell	0.5 ± 1	4 ± 2	13 ± 6	9 ± 3	122 ± 43

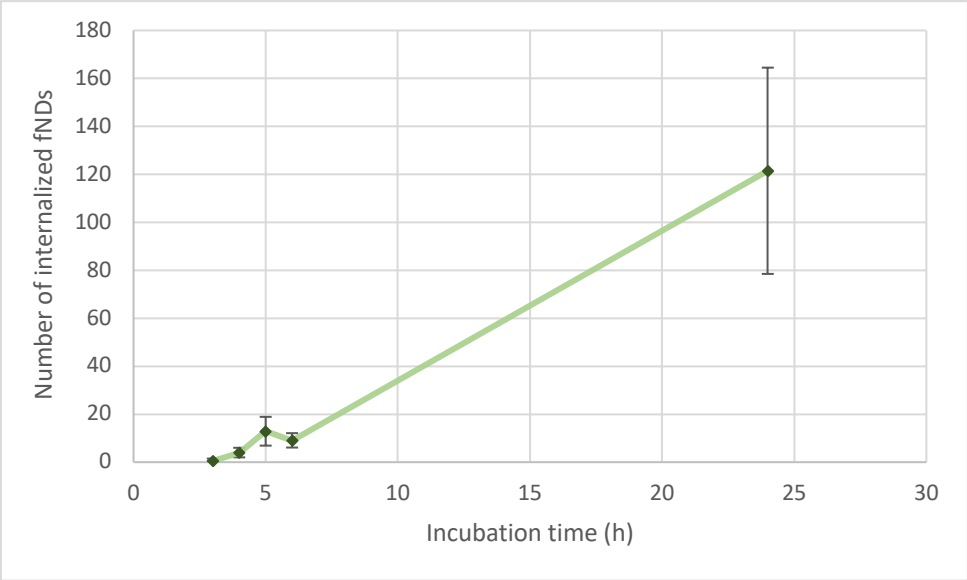

Figure 27: Evolution of number of bare 100 nm fNDs internalized in U2OS cells throughout the first 6 hours and after 24 hours of incubation.

In the first six hours of incubation, Figure 27 and Figure 28 show that the internalization rate is increasing exponentially and the fact that after 24 hours the number of internalized fNDs counts hundreds fNDs means that the excretion rate is significantly slower. This could also mean that the particles inside the cell undergo different pathways and not all particles are or can be excreted by the cell.

According to these results, the most convenient time to observe the interaction of fND with U2OS cell from the moment of interaction with outer membrane through the uptake process is four to five hours of incubation.

Table 2: Number of 100 nm PEG-fNDs internalized after stated incubation times.

Incubation time (h)	2	3	4	5	6	24
Number of PEG-fNDs per cell	4 ± 3	10 ± 5	30 ± 18	63 ± 15	31 ± 12	400 ± 46

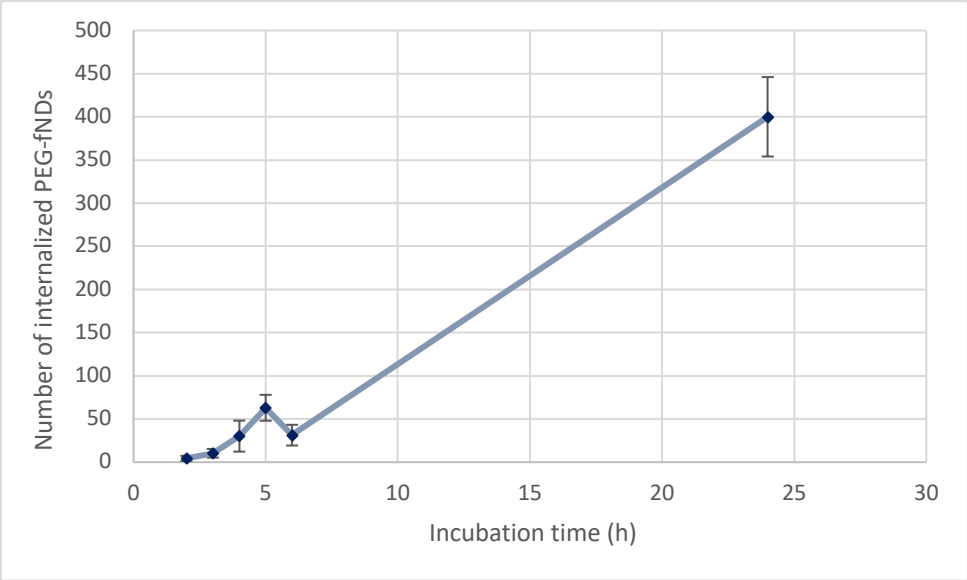

Figure 28: Evolution of number of 100 nm PEG-fNDs internalized in U2OS cells throughout the first 6 hours and after 24 hours of incubation.

5.5 Development of nanoparticle tracking software for iSCAT imaging

There is some tracking software freely accessible, for example tracking add-in for ImageJ, however, these are meant for localizing fluorescence or absorption imaging data and are not suitable for the complex iSCAT images presented in this work. Therefore, an appropriate tracking software had to be developed specifically for our type of data. The tracking software was made using MATLAB graphical user interface (GUI). The main features of the software are particle detection, automatic particle tracking, image processing and data processing.

The tracking interface is shown in Figure 29. This software enables data postprocessing after the acquisition of the data. First, the source video, in this case iSCAT recording, is opened which is visualized in the top left corner. By clicking the particle that we want to track, we select the position of ROI. The size of ROI can be adjusted to the size of the nanoparticle PSF size. The particle PSF is then fitted by gaussian function and it is cantered in the ROI for each frame. The image of the particle PSF and gaussian fitting can be seen below the main video. Additional parameters of the gaussian fit of ROI, i.e. number of particles in ROI, how many frames are accumulated for the fitting and the tolerable RMSE threshold, can be adjusted. Next, the image is normalized and static background is removed by subtracting consecutive images. Figure 30 shows the iSCAT image corresponding to the frame in Figure 29 before the normalization and background

subtraction. After such filtering we get much clearer image of the moving particle. In case the particle stops moving or escapes from the frame by rapid moving in z-axis direction, we are able to maintain the trajectory by gap-filling with the simultaneously recorded fluorescence detection which has broader detection depth than iSCAT. Although the software was developed for iSCAT data processing, any other type of imaging, like fluorescence in this case, can be analysed by it as well.

While this software is able to track the nanoparticle only in x-y plane, the z-axis data can be additionally extracted either from the particles PSF image[161] or it can be recorded by remote focusing[17] while maintaining the particle in focus in real time. Nevertheless, the data presented in this work are only 2D x-y trajectories whilst 3D tracking is still in development.

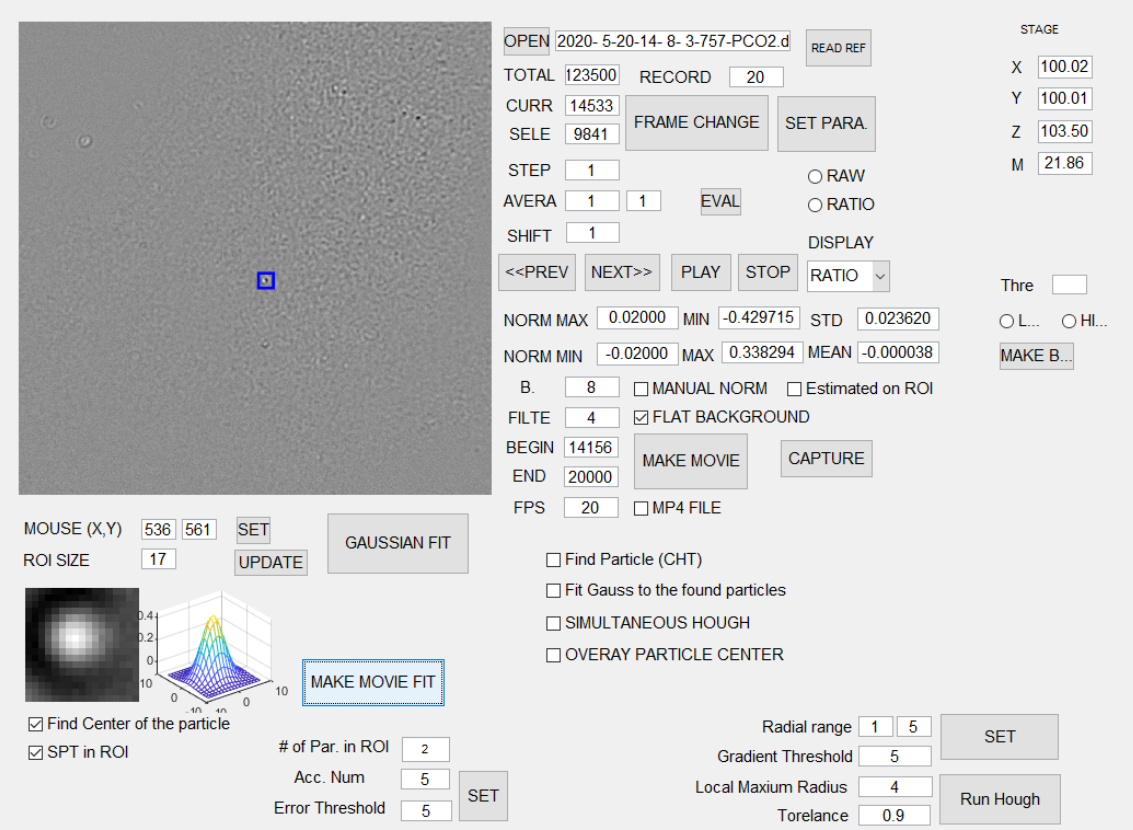

Figure 29: Particle tracking software made in MATLAB graphical user interface (GUI). The GUI involves display of the source recording, controls for preview of the recording, the particle detection window and fitting, filtering options and analysis controls.

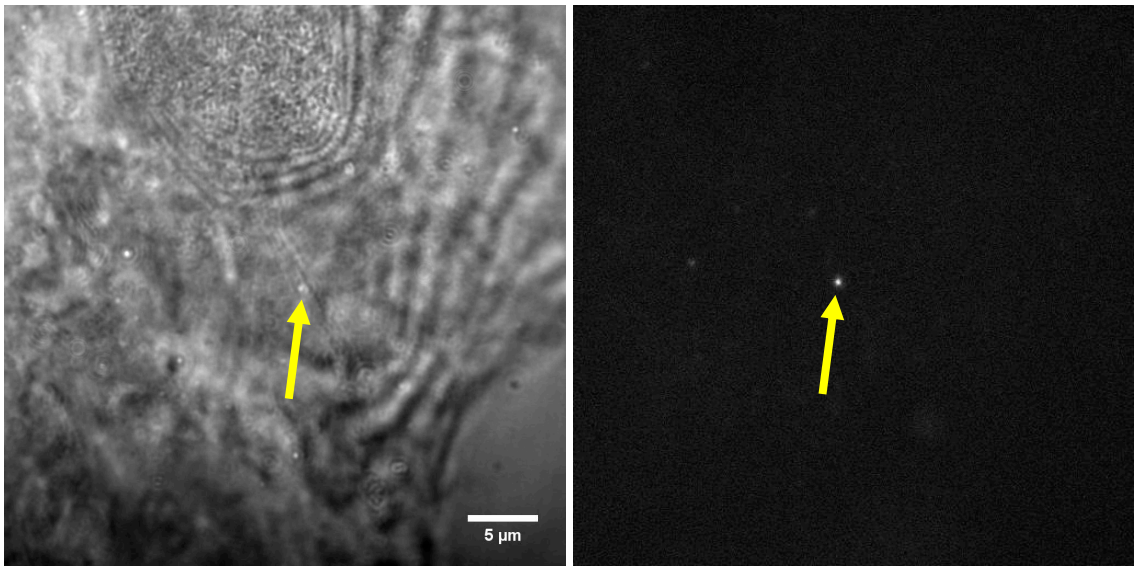

Figure 30: The iSCAT source recording used for the analysis example in Figure 29 before filtering out the background (left) and the complementary fluorescence recording (right). Yellow arrow marks the position of the tracked fND.

5.5.1 3D tracking via iSCAT remote focusing

There is possibility to track nanoparticles in 3D space by iSCAT remote focusing. This technique combines classical 2D SPT with remote focusing to obtain *z*-axis data. Remote focusing enables axial scanning by translation of reference mirror while objective lens and sample stage stay stationary[17]. This practically means that x-y data are recorded without disturbance or without frame rate limitation and additional images are recorded at different depths beyond the depth of field on additional camera.

The *z*-axial data can be recorded for each frame or every given number of frames. The process is schematically described by Figure 31. Each remote focusing axial scan (Figure 31 (b)) is analysed to find the nanoparticle`s focus point (Figure 31 (c)) which is the point that corresponds to particle`s exact position. Once obtaining the *z* position data (Figure 31 (d)), it can be plotted with the *x*-*y* data resulting in 3D trajectory.

This technique was only tested on short trajectories so far. It still requires several hardware and software improvements to be ready to use for large stacks of data, and long measurements.

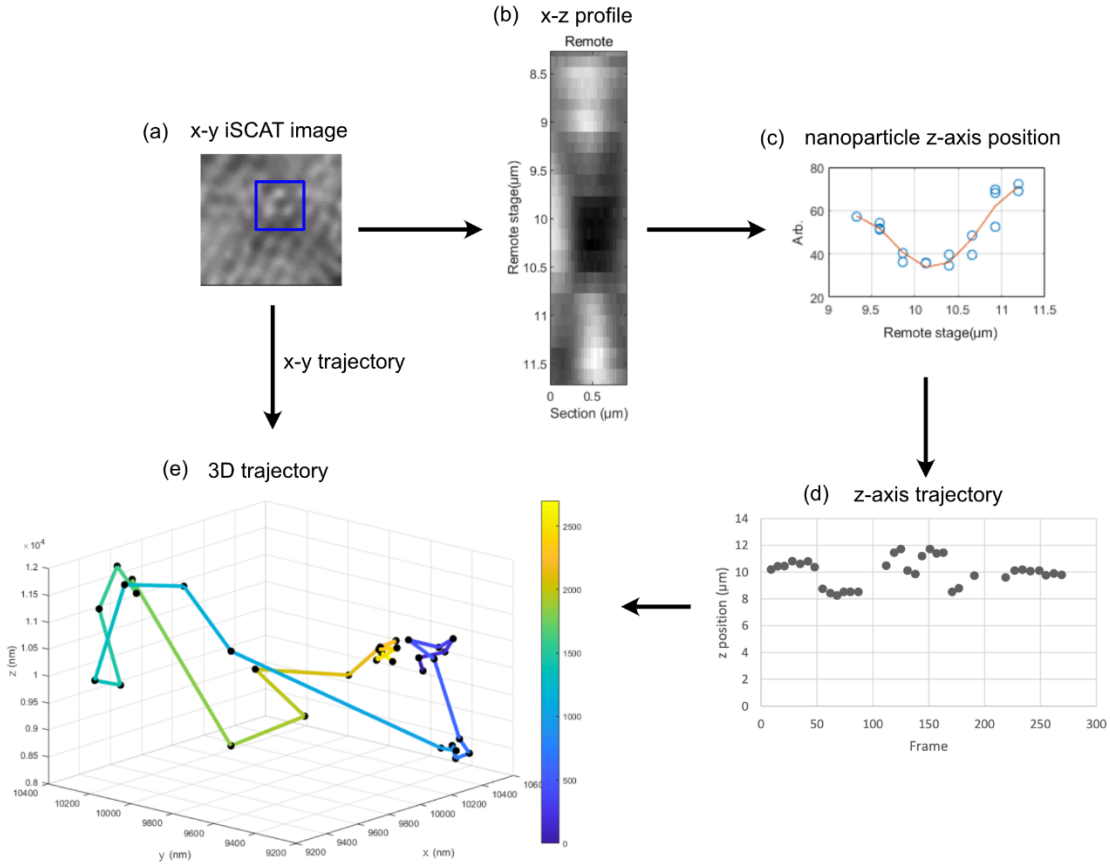

Figure 31: Recreation of 3D trajectory by remote focusing iSCAT (a) The source iSCAT data in x-y coordinates, (b) z-axial scan of the particle ROI, (c) fitting the minimum value of the z-axial scan to find the precise position of the nanoparticle, (d) detected z-positions of the nanoparticle by remote focusing, (e) 3D trajectory made by combining x-y and z trajectory data.

5.6 Diffusion of fNDs in cytosol

Different sizes of nanoparticles should exhibit different speed and types of motion. Here, two sizes of fNDs were tested, the smallest possible to detect with iSCAT, 10 nm fNDs, and 100 nm fNDs which are larger enough and should be well received by cell uptake mechanism.

The trajectory of fND was recorded first and analysed afterwards. The analysis involved plotting an MSD curve, fitting the short time-lag data (the first linear section of the MSD curve) and the long time-lag data (second linear section of the MDS curve). The rest of the data was excluded from the analysis to minimize the error because less data is collected for long time-lags and the uncertainty of MSD analysis is therefore higher, as explained in the theoretical section 2.4.

5.6.1 10 nm fND diffusion

Twenty 10 nm fND particles were analysed in total. The types of motion detected can be sorted into four different categories of motion: (i) normal diffusion, (ii) anomalous diffusion, (iii) confined diffusion and (iv) directed motion. Additionally, each type of diffusion seemed to be typical for different parts of the cell. In general, the closer to the nucleus the more confined the motion seemed to be. One of the reasons can be the fact that the cell is more occupied by organelles and intrinsic structures towards the nucleus opposed to the outskirt areas.

The diffusion of 10 nm fND near the nucleus is typically closely confined. Figure 32 demonstrates two cases of such motion. Pictured fND #1 diffuses right along the border of the nucleus in anomalous manner. Both from the trajectory and MSD curve it is recognizable that the particle diffuses in a confined prolonged area, but it is not completely trapped. Such particle can be for example confined in between organelles surrounding the nucleus, *e.g.*, Golgi apparatus. While fND #2 is enclosed in much smaller area. Such particles exhibiting minimal motion and slow diffusion are typically found right on the surface of the nucleus. While it is believed that particle of this size cannot enter the nucleus itself, it can enter the perinuclear area. The shape of the MSD curve clearly shows a confinement that can be recognized by the second segment having lower slope than the first segment.

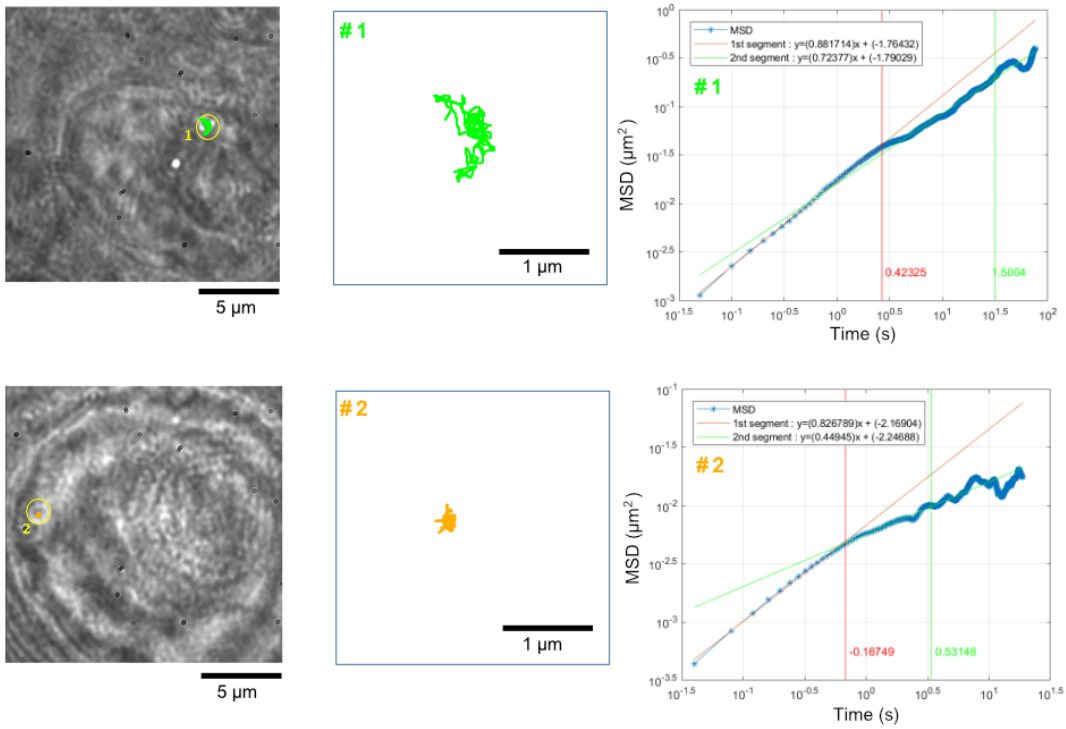

Figure 32: 10 nm fND diffusion in the area surrounding the nucleus and corresponding MSD analysis. (a) image of the position of the fND #1 and #2 inside the cell. (b) 2D Trajectories of the fNDs #1 and #2. (c) MSD curves (blue) corresponding to the trajectories #1 and #2. The red fitting line fits the short time-lag (1st segment) data and the green fitting line fits the long time-lag (2nd segment) data. Each of the time-lag section is designated by the vertical line of the corresponding colour. Legend: fND #1 1st segment: y = 0.88 x – 1.76, 2nd segment: y = 0.72 x – 1.79. fND #2 1st segment: y = 0.83 x – 2.17, 2nd segment: y = 0.45 x – 2.25.

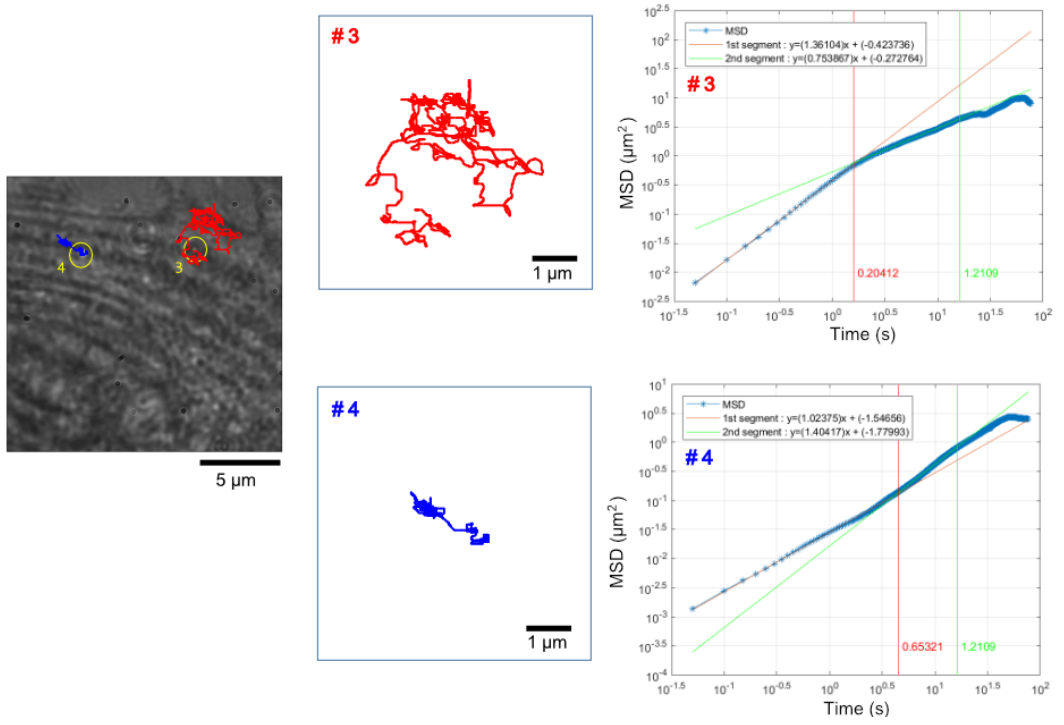

Figure 33: 10 nm fND diffusion in cytosol and corresponding MSD analysis. (a) image of the position of the fND #3 and #4 inside the cell. (b) Trajectories of the fNDs #3 and #4. (c) MSD curves (blue) corresponding to the trajectories #3 and #4. The red fitting line fits the short time-lag (1st segment) data and the green fitting line fits the long time-lag (2nd segment) data. Each of the time-lag section is designated by the vertical line of the corresponding colour. Legend: fND #3 1st segment: y = 1.36 x – 0.42, 2nd segment: y = 0.75 x – 0.27. fND #4 1st segment: y = 1.02 x – 1.55, 2nd segment: y = 1.40 x – 1.78.

The particles fND #3 and #4 in the Figure 33 represent typical motions of 10 nm fNDs in the cytosol. fND #3 is diffusing freely in the cytoplasm right at the outskirt of the cell. The range of the motion of #3 is the largest and its diffusion is the fastest of all pictured examples. fND #3 is the closest to the Brownian motion while the MSD curve still indicates that the motion was, in fact, confined in the long-time scale. Last but not least, fND #4 is an example of the consecutive confined motion areas with fast somewhat directional transitions in between them, which is called corralled diffusion. A particle can undergo this kind of diffusion either when it diffuses in between cellular organelles by itself or when it is trapped in a vesicle which can be transported by active transport mechanism of the cell. In this particular case, the MSD curve shape suggests the active transport involvement since the second segment of the curve has higher slope than the first meaning fast diffusion in long time scale.

5.6.2 100 nm fND diffusion

Fifty 100 nm fND particles were analysed in total. The detected types of motion were confined diffusion, anomalous diffusion and directed motion. In comparison to 10 nm fNDs, no free diffusion was observed. The most common type of motion for 100 nm fNDs was the corralled diffusion. It can be detected both in cytosol and near the nucleus.

In the Figure 34 all three pictured fNDs are in the vicinity of the nucleus. The fNDs #5 and #6 both exhibit the corralled diffusion. Meanwhile, fND #7 undergoes confined diffusion very similar to 10 nm fND #1 in scale, placement and shape of the MSD curve. It is important to note, that the timescale for these three particles is the same. All three MSD curves suggest the anomalous diffusion, which is distinguished in the long-time scale, for #5 and #7 it becomes confined diffusion, for #6 it is confined transitioning to directed diffusion.

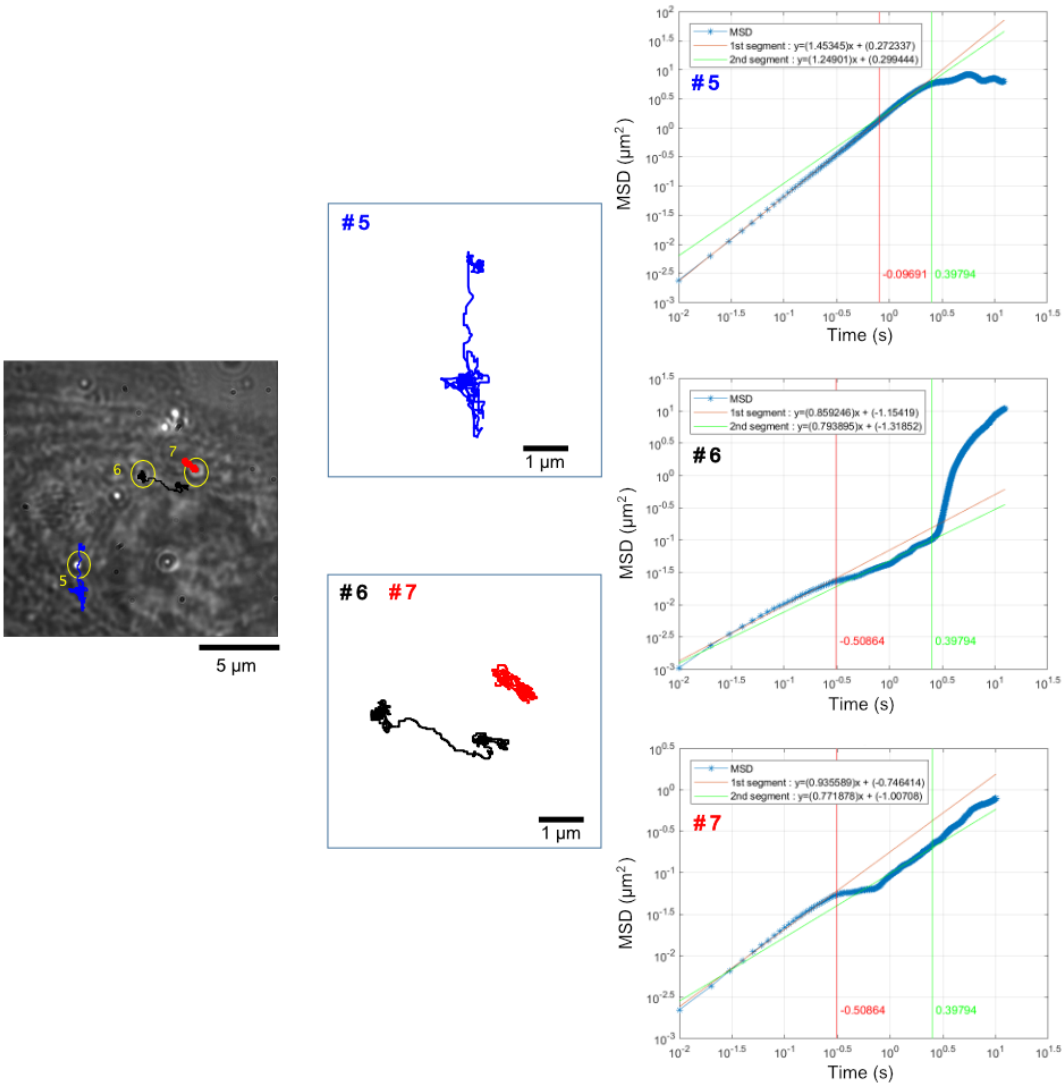

Figure 34: 100 nm fND diffusion near the nucleus and corresponding MSD analysis. (a) image of the position of the fND #5, #6 and #7 inside the cell. (b) Trajectories of the corresponding fNDs. (c) MSD curves (blue) corresponding to the trajectories. The red fitting line fits the short time-lag (1st segment) data and the green fitting line fits the long time-lag (2nd segment) data. Each of the time-lag section is designated by the vertical line of the corresponding colour. Legend: fND #5 1st segment: y = 1.45 x + 0.27, 2nd segment: y = 1.25 x + 0.30. fND #6 1st segment: y = 0.86 x – 1.15, 2nd segment: y = 0.79 x – 1.32, fND #7 1st segment: y = 0.94 x – 0.75, 2nd segment: y = 0.77 x – 1.01.

The fND #8 in the Figure 35 is diffusing inside the cytosol and it is exhibiting fast directional motion with very few confinements along the way. Both the trajectory and the MSD curve show typical shapes for the directed motion. #9 is an example of the corralled diffusion with directional motion in the cytosol. fND #10 is located on top of the nucleus and same as the 10 nm fND #2 it exhibits very confined motion which brings us to believe that even 100 nm fND can be trapped in the perinuclear space.

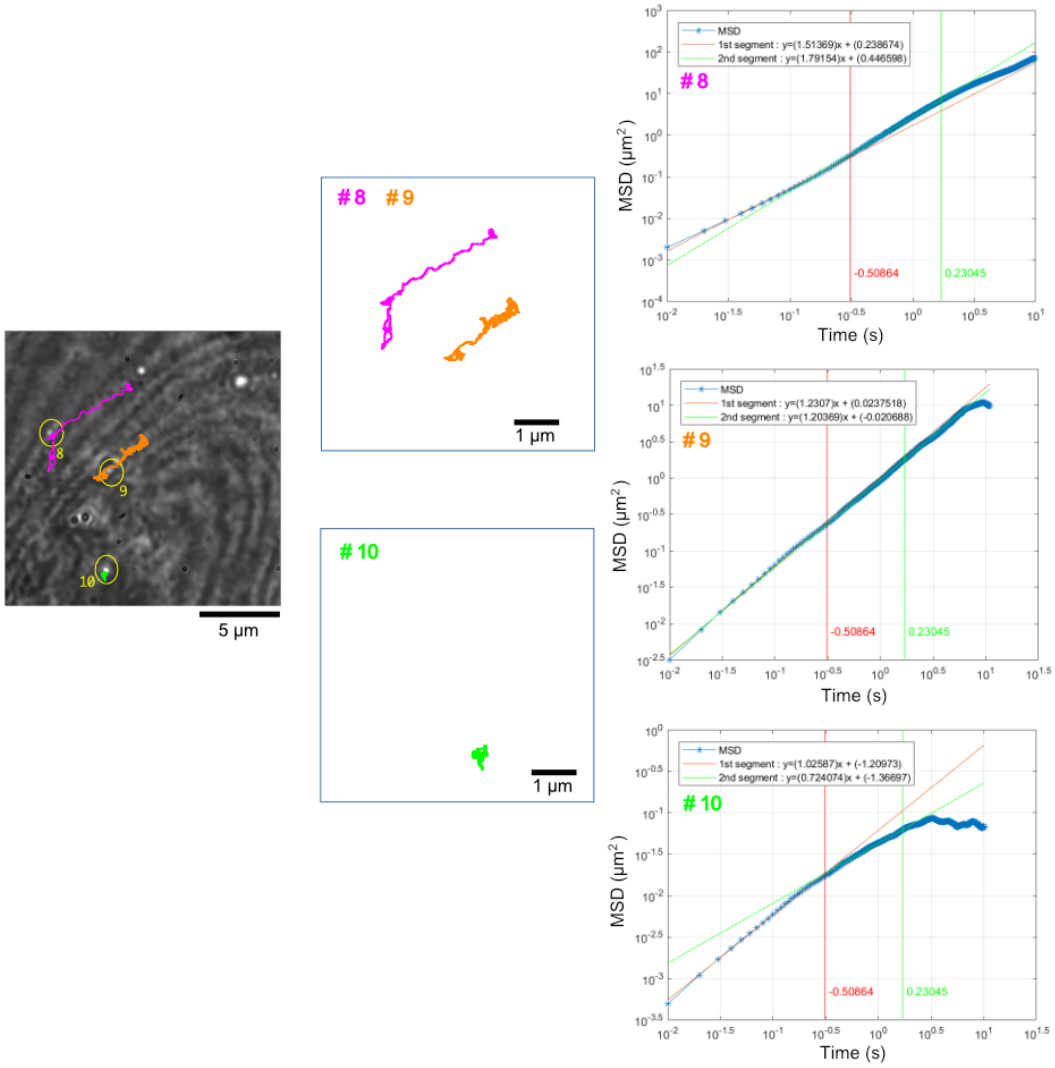

Figure 35: 100 nm fND diffusion and corresponding MSD analysis. (a) image of the position of the fND #8, #9 and #10 inside the cell. (b) Trajectories of the corresponding fNDs. (c) MSD curves (blue) corresponding to the trajectories. The red fitting line fits the short time-lag (1st segment) data and the green fitting line fits the long time-lag (2nd segment) data. Each of the time-lag section is designated by the vertical line of the corresponding colour. Legend: fND #8 1st segment: y = 1.51 x + 0.23, 2nd segment: y = 1.79 x + 0.45. fND #9 1st segment: y = 1.23 x + 0.02, 2nd segment: y = 1.20 x – 0.02, fND #10 1st segment: y = 1.03 x – 1.21, 2nd segment: y = 0.72 x – 1.37.

Overall, it seems that 100 fNDs are undergoing corralled diffusion often combined with some directed motion. This suggests that 100 nm fNDs are enclosed in intracellular vesicles and those vesicles can be part of the active transport of the cell. This behaviour is different from the 10 nm fNDs where we observed confined diffusion in a very tight spaces or Brownian motion in a larger space with obstructions which leads us to believe that 10 nm fNDs are not trapped in a vesicle but more likely diffuse by themselves.

5.6.3 Diffusion coefficient of fND in the U2OS cell

The diffusion coefficient of fND examples above is in the Table 3. The diffusion coefficients were calculated from the first segment of the MSD curves for short time-lags using the formula for anomalous diffusion (Eq. (32)).

Table 3: Typical values of 2D diffusion coefficient of 10 and 100 nm large fNDs diffusing in the cell cytosol and nucleus. Particle number corresponds to the numbering in Figure 32 - Figure 35.

Particle number	Size	Location	Diffusion type	2D diffusion coefficient (nm^2/s)
1	10	Nucleus	Anomalous	4.05
2	10	Nucleus	Confined	1.69
3	10	Cytosol	Free	9.42
4	10	Cytosol	Corralled	7.10
5	100	Cytosol	Corralled	71.1
6	100	Cytosol	Corralled	67.4
7	100	Cytosol	Confined	24.0
8	100	Cytosol	Directional	433
9	100	Cytosol	Directional	264
10	100	Nucleus	Confined	15.4
11	100	Nucleus	Confined	1.99

The Table 3 represents typical values measured across all seventy analysed fNDs. Particle #11 is not displayed amongst the visual examples above, however, it was included in the table as an important representation of 100 nm fND sample.

The 2D diffusion coefficients show that

i) the diffusion in the proximity of the nucleus is significantly slower,

ii) the 10 nm fND diffuses several times slower in the cell than 100 nm fND,

iii) the directional motion where the active transport is involved can be ten times faster than the other passive diffusion types.

A few principles can explain these behaviours. A particle diffuses slower in an environment with higher mass density which is seen in the case of the particles near the nucleus. Here we have two cases of the diffusion in the nucleus proximity. One, tightly confined particles (#2, #10 and #11) right at the border of the nucleus, which is believed

to be a fND trapped in the perinuclear space. There, besides the small space for the diffusion, the density of the perinuclear cytoplasm is about two times higher[162] than the cytoplasm which makes the diffusion also slower. Second, anomalous diffusion which is confined with wider range of movement at the nucleus proximity (#1). While #1 has higher diffusion coefficient than tightly confined #2 it is still twice slower than fNDs diffusing in the free cytoplasm showing that even with less confinement, the particle is slowed down in the perinuclear environment.

The fact that smaller fNDs had slower diffusion than large fNDs can be, in general, caused by small particles being easily trapped in crevasses and small structures that do not cause any obstruction to the particles that are larger than the possible entrapment. This also results in smoother trajectories for the 100 nm fNDs. Other reason for the fasted diffusion of 100 nm fND is its fate in the cell. As already established, the 100 nm fND can be encapsulated in the vesicle after clathrin or calveolin mediated endocytosis, thus undergoing smoother transport in the cell including active transport.

5.7 Interaction of fNDs with plasma membrane

The interaction with a cell membrane was recorded two hours after introducing the fNDs to the cell culture medium. As internalization rate experiment (Chapter 5.4) showed, no fNDs should be internalized yet. At this point, it was possible to observe free fNDs in the cell culture medium, fNDs attaching and detaching from the cell membrane and fNDs diffusing along the membrane surface which consequently leads to the internalization process. The particles attached to the membrane were the observation target here. The aim was to monitor the events before the internalization and general particle behaviour on top of the membrane for comparison with its behaviour inside the cell.

To capture as many events as possible, the measurement was carried out for as long as possible. The main restriction was the cell vitality. To keep the cell alive and vital for as long as possible, it was placed in small incubation cell which was anchored to the microscope's sample stage. The cell was enclosed and kept atmosphere with 5 % CO_2 and temperature 37 °C. Another condition was to keep the laser power at the lowest level possible. The laser power sufficient to detect the fND was 0.4 – 1.3 mW at the sample. In this setting, the recording time possible was two hours before the cell death. However, changes in cell vitality were usually detectable already after one hour. Therefore, the results presented here are only acquisitions from the first hour of the recordings. The

sample chosen for this experiment were 100 nm fNDs due to their easy detectability in iSCAT and high internalization rate.

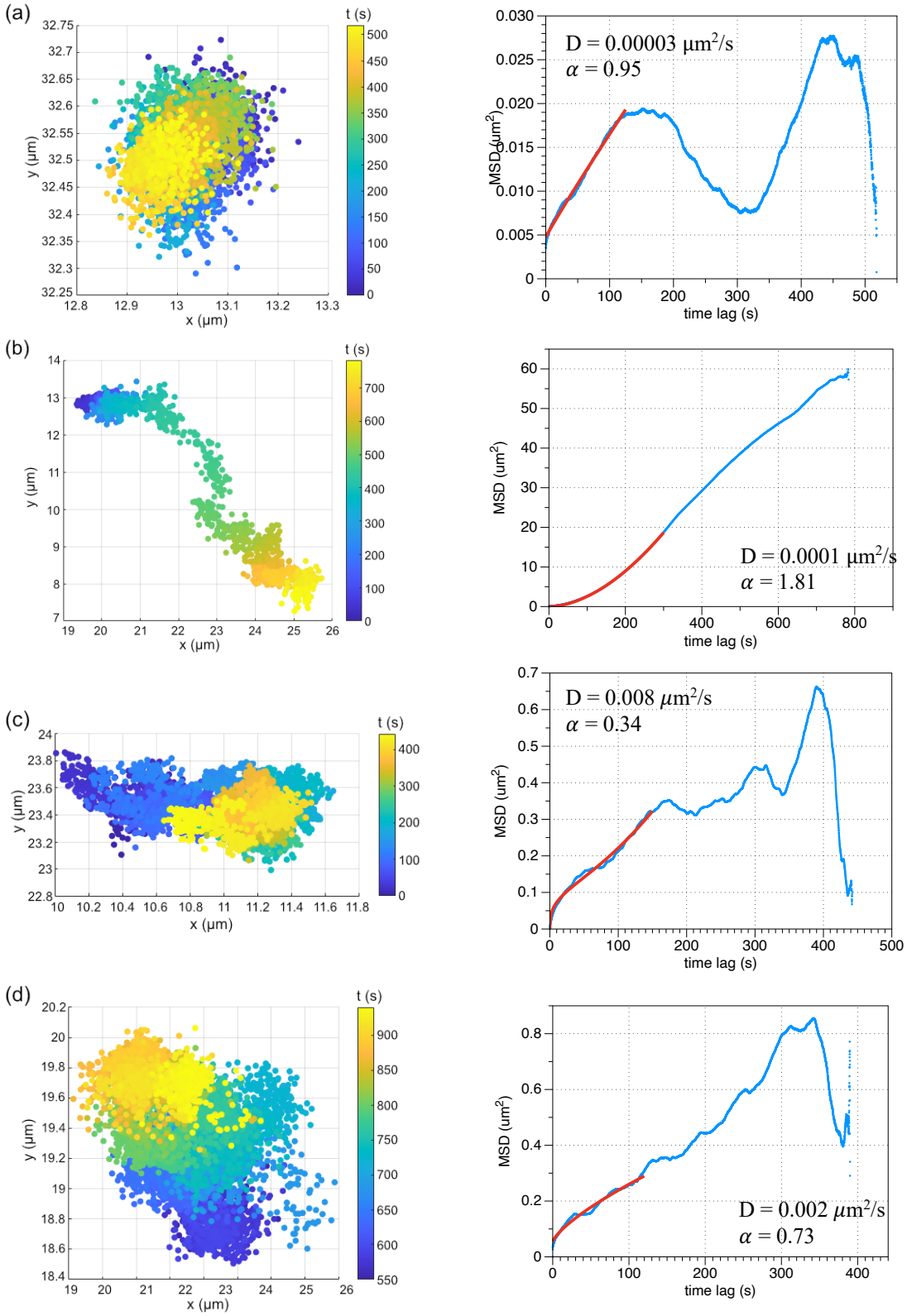

Figure 36: Representing trajectories and corresponding MSD curves of four 100 nm fND particles diffusing on top of the plasma membrane. The x-y coordinates correspond to the original detected image coordinates, the timescale is given by the gradient bar along the right of the plot. The mean square displacement (MSD) curve in time is plotted in blue, the red plot is the fit of the relevant part of the MSD curve used for the 2D diffusion coefficient D and α parameter calculation.

The fNDs motion on top of the cell membrane was typically corralled diffusion. The corrals in this case are the membrane pits with receptors and concentrated charge. The fND gets trapped in such pits for substantial amount of time during its existence on top of the membrane. The trajectory is often condensed in a small area, the particle usually travels a few micrometres in a large scale while the actual length of the trajectory ranges in hundreds of micrometres. Noticeable difference between the diffusion on top of the membrane and inside the cell was the speed of the fND. In average, the diffusion coefficient of fNDs on top of the membrane was ten times slower than of those inside the cell. That is, when excluding the active transport inside the cell which is not present on top of the membrane.

Typical examples of the 100 nm fND diffusion on the plasma membrane are in Figure 36.

5.7.1 Trajectory analysis

In case of complex way of motion where the particle undergoes different events along its trajectory, the spatial and temporal resolution is crucial. Depending on which information we want to acquire, we also need to choose the appropriate range or scale.

An example of a complex trajectory is in Figure 37 (c). The trajectory was recorded at a U2OS cell surface that was relatively flat, which can be assumed from the widely spread fringe pattern around the location of the red rectangle in Figure 37 (a). Despite being focused at the surface of the cell, recognized by the distinct fringe pattern created by the overall shape and slope of the cell surface, the cell dynamics is coming through also which makes the image very busy. To detect a single particle, a static and slow-moving structures were removed (Figure 37 (b)). Still, some cellular dynamics and fast-moving vesicles were left in the image but only fNDs on the cell surface were in the focus plane.

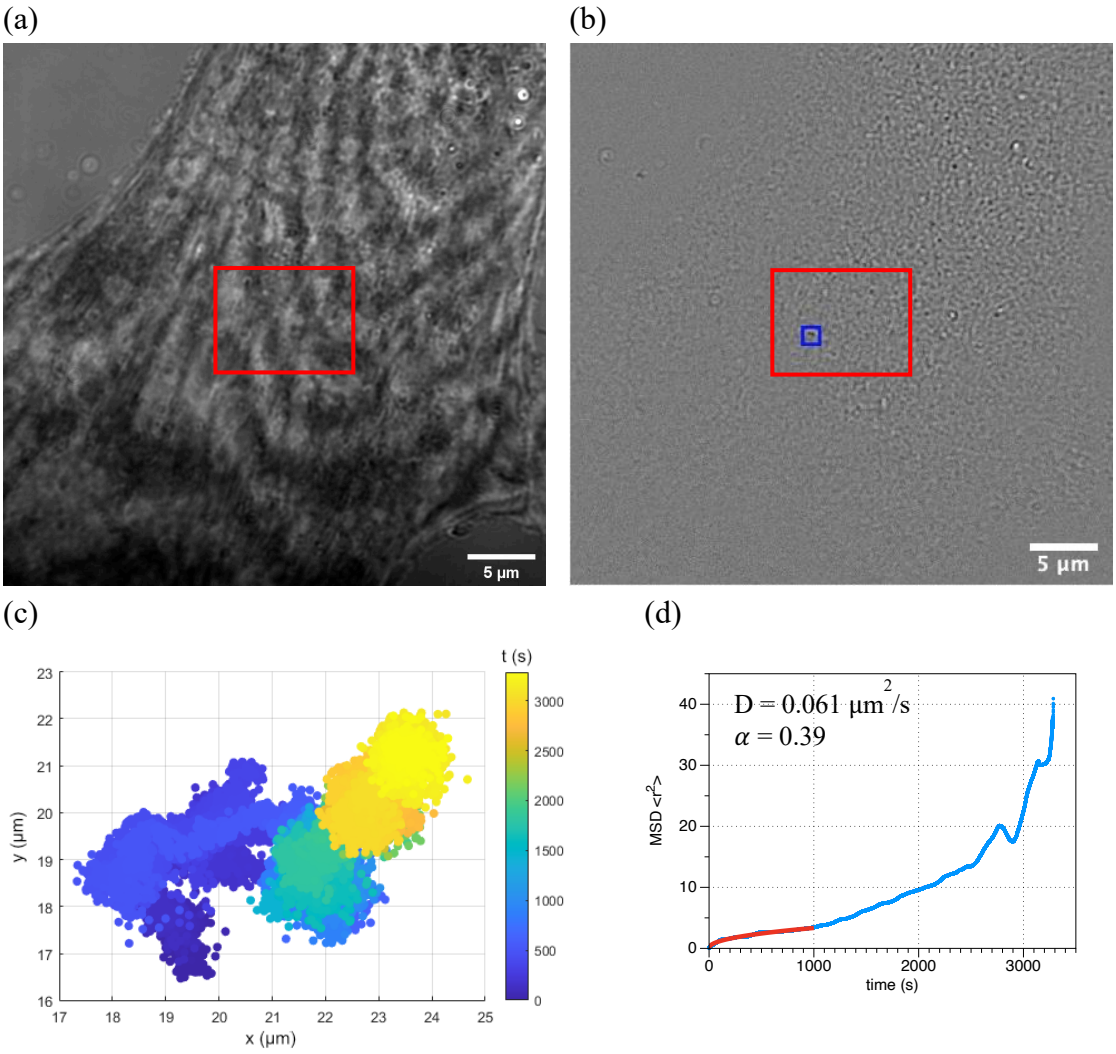

Figure 37: fND diffusing on the membrane of U2OS cell. a) raw image of the recording, (b) filtered image with detected particle marked by a blue rectangle, the red rectangle marks the area displayed in the trajectory plot (c) The x-y coordinates in (c) correspond to the original detected image coordinates, the timescale is given by the gradient bar along the right of the plot., (d) corresponding MSD plot fitted by red line which was used for calculating 2D diffusion coefficient D and α parameter.

The whole trajectory was recorded for 58 minutes. The total trace length was 7134 µm. Overall, according to the D and MSD curve shape, the diffusion would be classified as anomalous diffusion. To specify it better, we can consider α parameter (α = 0.39) and we can call it an anomalous sub-diffusion. To learn more, the trajectory needs to be broken down to parts.

The original trajectory was broken down to four parts (A-D) displaying different behaviours. The timescale in Figure 38 - Figure 41 matches the timescale in Figure 37.

A

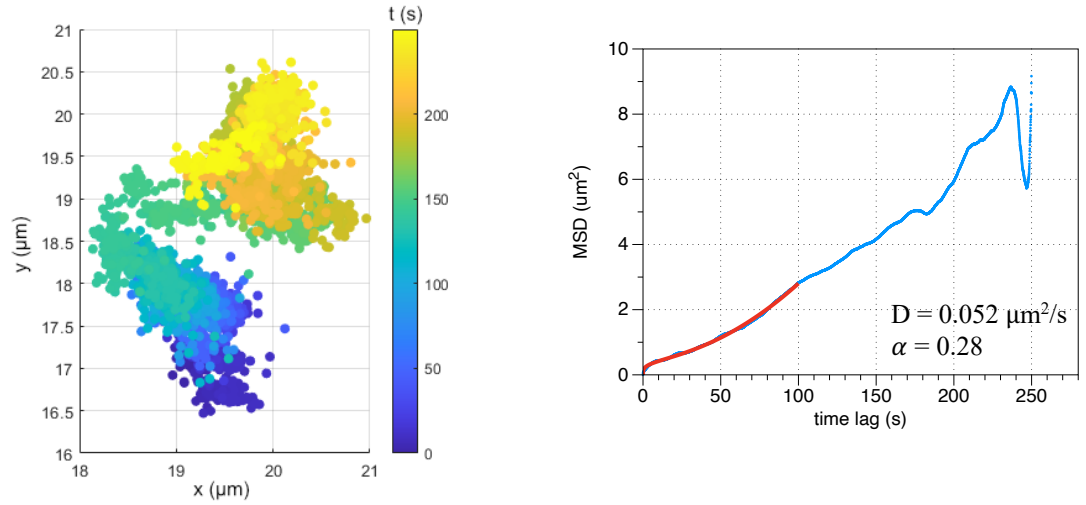

Figure 38: Segment A of the trajectory in Figure 37 (left) and corresponding MSD plot fitted by red line which was used for calculating 2D diffusion coefficient D and α parameter (right).

The fND in the first segment A (Figure 38) was diffusing most sporadically and with highest speed (D = 52 nm^2/s). The MSD plot and its fitting show that the segment A was a case of anomalous sub-diffusion which was closer to normal diffusion than the other following segments. In this case, it could be described as a fND that was not yet tightly attached to the plasma membrane by electrostatic forces. In this stage, the particle gets often detached from the cell and floats away.

B

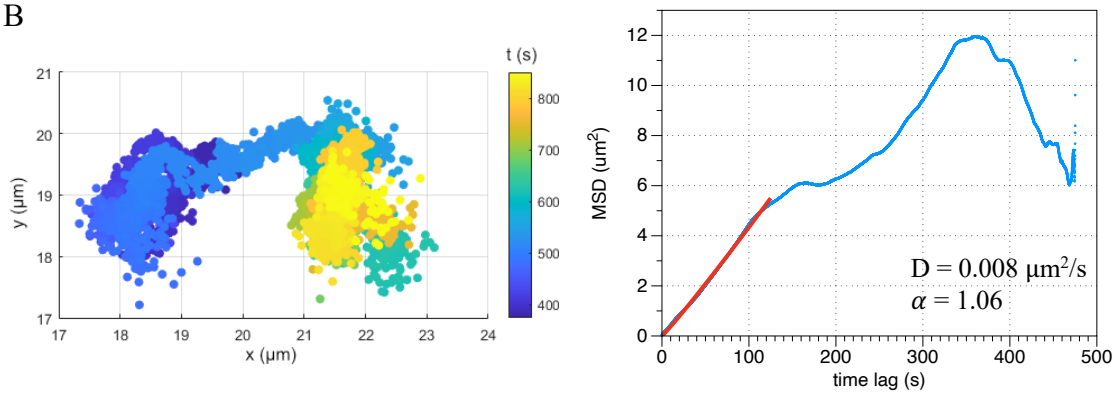

Figure 39: Segment B of the trajectory in Figure 37 (left) and corresponding MSD plot fitted by red line which was used for calculating 2D diffusion coefficient D and α parameter (right).

In the segment B (Figure 39), the fND already diffuses with much slower speed (D = 8 nm2/s), the fND copies the topography of the cell and the trajectory clearly shows two corrals, membrane pits, and passage in between them. When a particle is trapped in the membrane pit and the endocytosis process is not triggered the particle continues moving alongside the membrane and gets trapped in other pits until it eventually gets internalized or detached from the membrane. Segment B therefore exhibits the corralled diffusion.

C

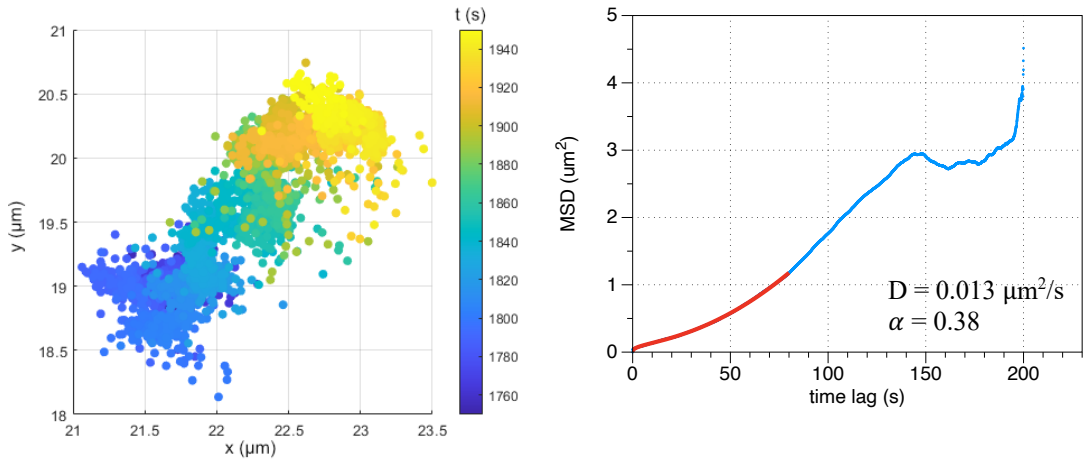

Figure 40: Segment C of the trajectory in Figure 37 (left) and corresponding MSD plot fitted by red line which was used for calculating 2D diffusion coefficient D and α parameter (right).

In the segment C (Figure 40), the fND was moving in a directional motion through the crevasses in the plasma membrane which suggest both the wavy prolonged trajectory and the MDS plot curved upwards.

D

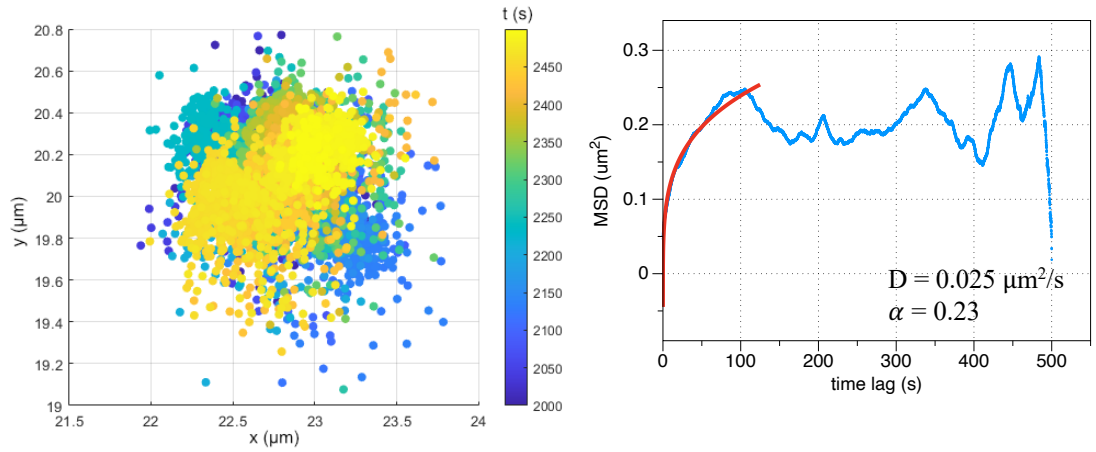

Figure 41: Segment D of the trajectory in Figure 37 (left) and corresponding MSD plot fitted by red line which was used for calculating 2D diffusion coefficient D and α parameter (right).

The last segment D (Figure 41) is a clear example of confinement. Here we can see that the membrane pit is round and about 1.5 µm large in diameter. Interestingly, the diffusion was faster inside the pit (D = 25 nm2/s) than when diffusing along the membrane in the segment C or B.

5.7.2 Importance of timescale

Similarly as the trajectory breakdown, this section shows how the result can change with the increasing timescale. Choosing the right timescale depends on whether we want to observe short-term or long-term events. If we want to capture one specific incident, *e.g.* the exact moment of endocytosis or dynamics inside the membrane pit that occurs in range of micro- to picoseconds, we need to choose not only a short timescale for trajectory analysis but the data need to be recorded with appropriate time resolution shorter than the event itself to collect enough data points for the analysis. Here, in order to record the overall fND diffusion on the membrane the time resolution was in range of milliseconds.

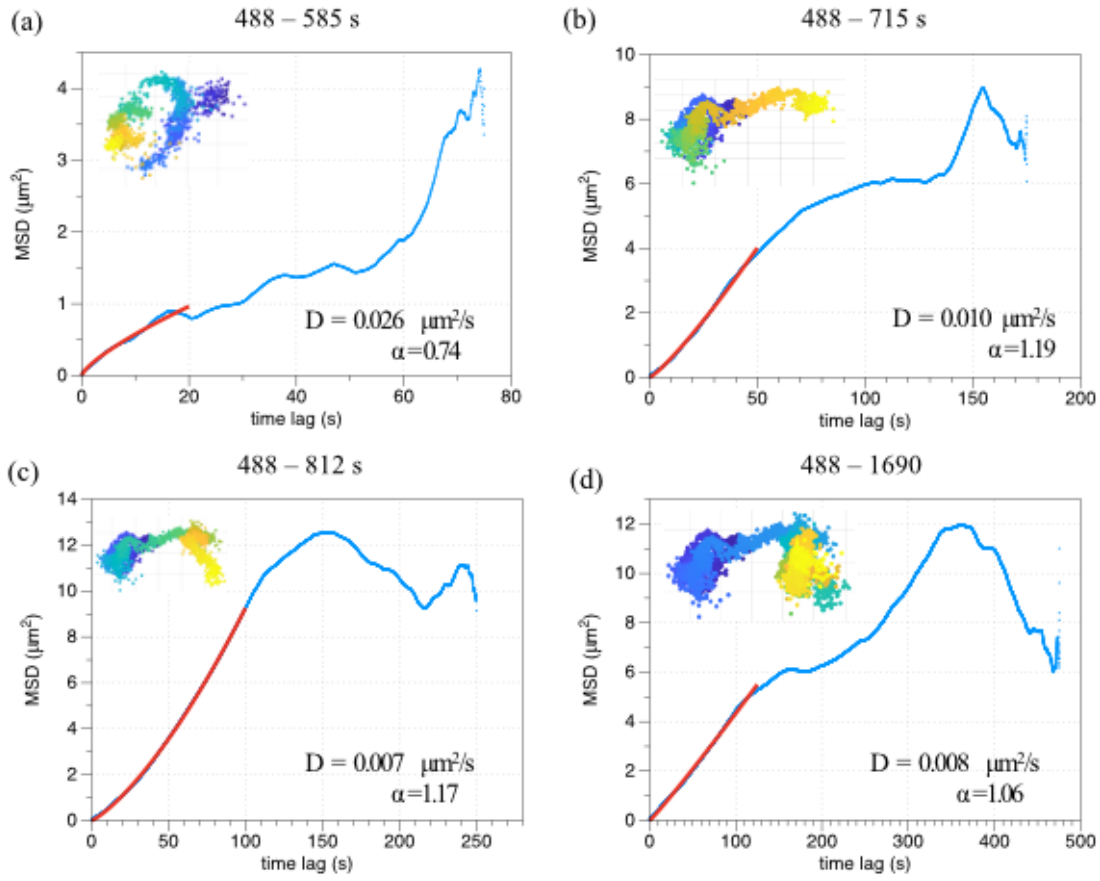

Figure 42: Trajectory development in time and how the MSD analysis changes with progressively longer timescale.

Figure 42 presents a trajectory development in time and how the MSD curve and coefficients D and α can change alongside the increasing timescale. In Figure 42 (a), the MSD curve and its fit are calculated from only one hundred seconds of trajectory recording and it is visibly different from the (b-d) results. In this case the fND diffused faster (D = 26 nm^2/s) and in a confined manner. However, the longer the trajectory gets

the more averaged all the data become, and this short example of confinement gets hidden in the final result. Figure 42 (b-c) already give off similar results and the very clear directional motion, starting at (b), prevails all other events along the track.

5.7.3 iSCAT versus fluorescence tracking precision

In fluorescence microscopy, the particle tracking is fairly easy task thanks to clear distinction between the fluorescent particle and dark background. However, it also has some disadvantages, i.e. blinking and photobleaching, due to which it is not possible to record with high frequencies or for a very long time. On contrary, in purely optical method like iSCAT, we can record long-term measurements at very high frequencies. The downside here are the background signals and noise. The background needs to be filtered out which may be challenging at some cases.

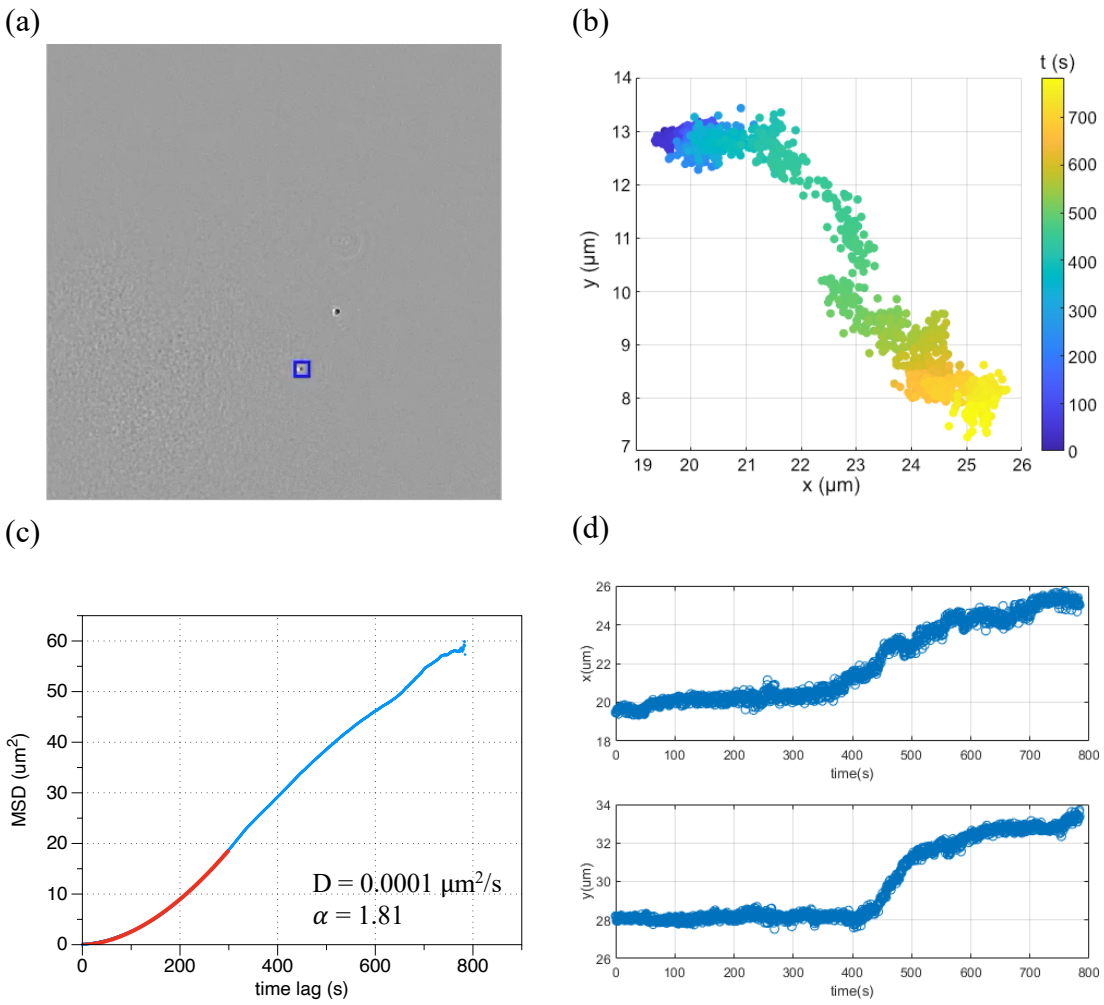

Figure 43: iSCAT tracking: (a) source recording with the tracked fND marked by blue rectangle, (b) obtained trajectory after SPT, (c) MSD curve (blue) corresponding to the trajectory with fitting curve (red) and parameters D and α, (d) 1D trajectories in x- and y-axis.

If we compare the two trajectories (Figure 43 (b, d) and Figure 44 (b, d)) we can clearly see the same features, although the trajectories are not exactly point to point the same which can be related to the different frequencies of the sCMOS (iSCAT) and EMCCD (fluorescence) detectors. Nevertheless, the two MSD curves (Figure 43 (c), Figure 44 (c)) closely resemble each other in shape and trend and their fitting gives off the same results (D = 0.1 nm2/s, α = 1.8).

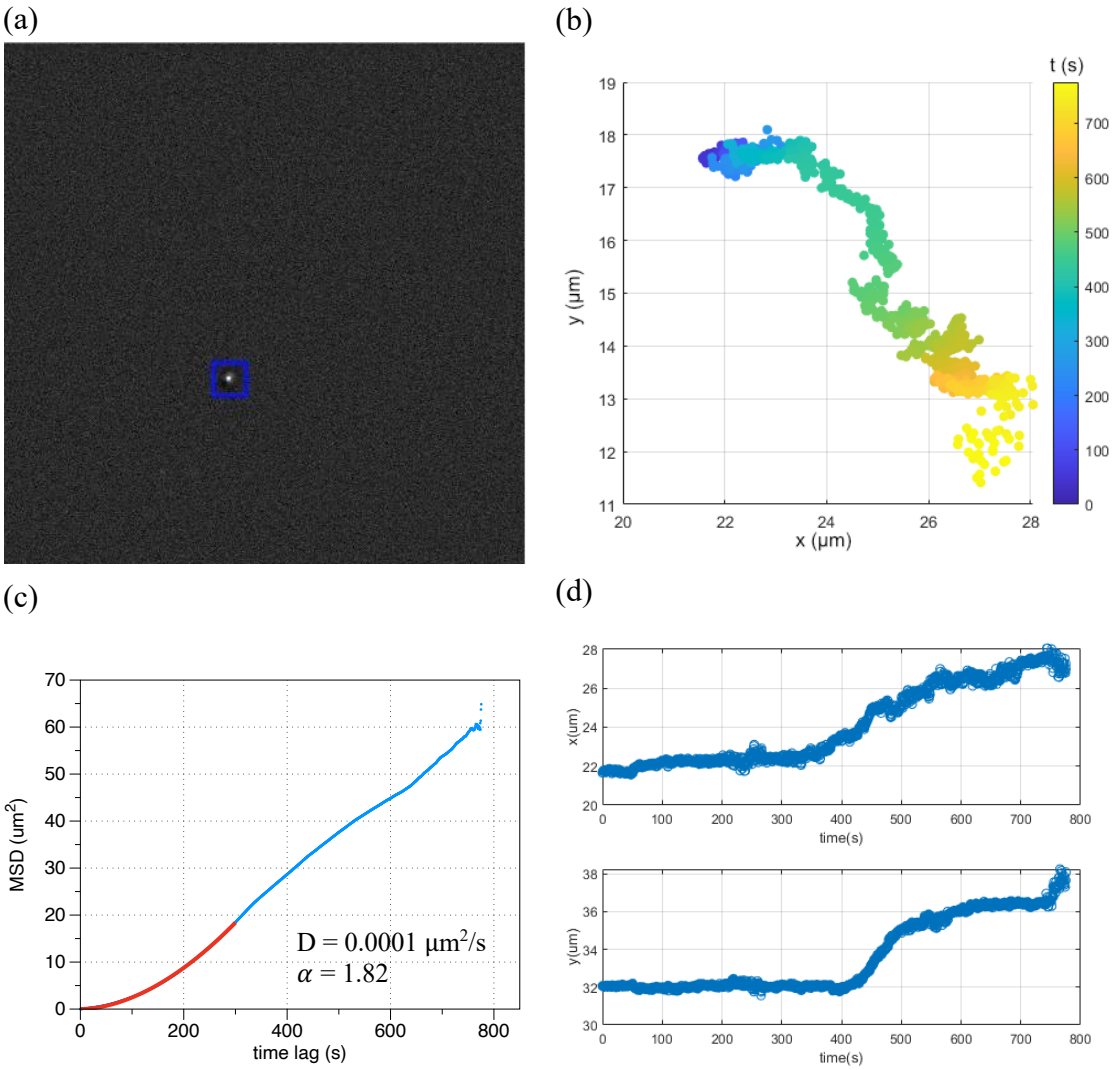

Figure 44: Fluorescence tracking: (a) source recording with the tracked fND marked by blue rectangle, (b) obtained trajectory after SPT, (c) MSD curve (blue) corresponding to the trajectory with fitting curve (red) and parameters D and α, (d) 1D trajectories in x- and y-axis.

This comparison proves that iSCAT tracking can be as reliable as fluorescence tracking and on top of that the advantages of optical imaging can be successfully utilized for precise long-term measurements.

5.7.4 Interaction of PEG coated fND with plasma membrane

The internalization rate of PEG-fNDs proved to be faster than of the uncoated fNDs (Chapter 5.4). Therefore, it can be assumed that the interaction with the plasma membrane will be different as well.

The same 100 nm PEG-fND sample as for the internalization experiment was used for tracking. The incubation time before observation was one hour in this case. The PEG-fNDs were observed from the moment of free diffusion in the culture medium until the moment of interaction with the plasma membrane to make sure that the PEG fND is not already internalized. Typical examples of PEG-fND and plasma membrane interaction are presented in Figure 45 and Figure 46.

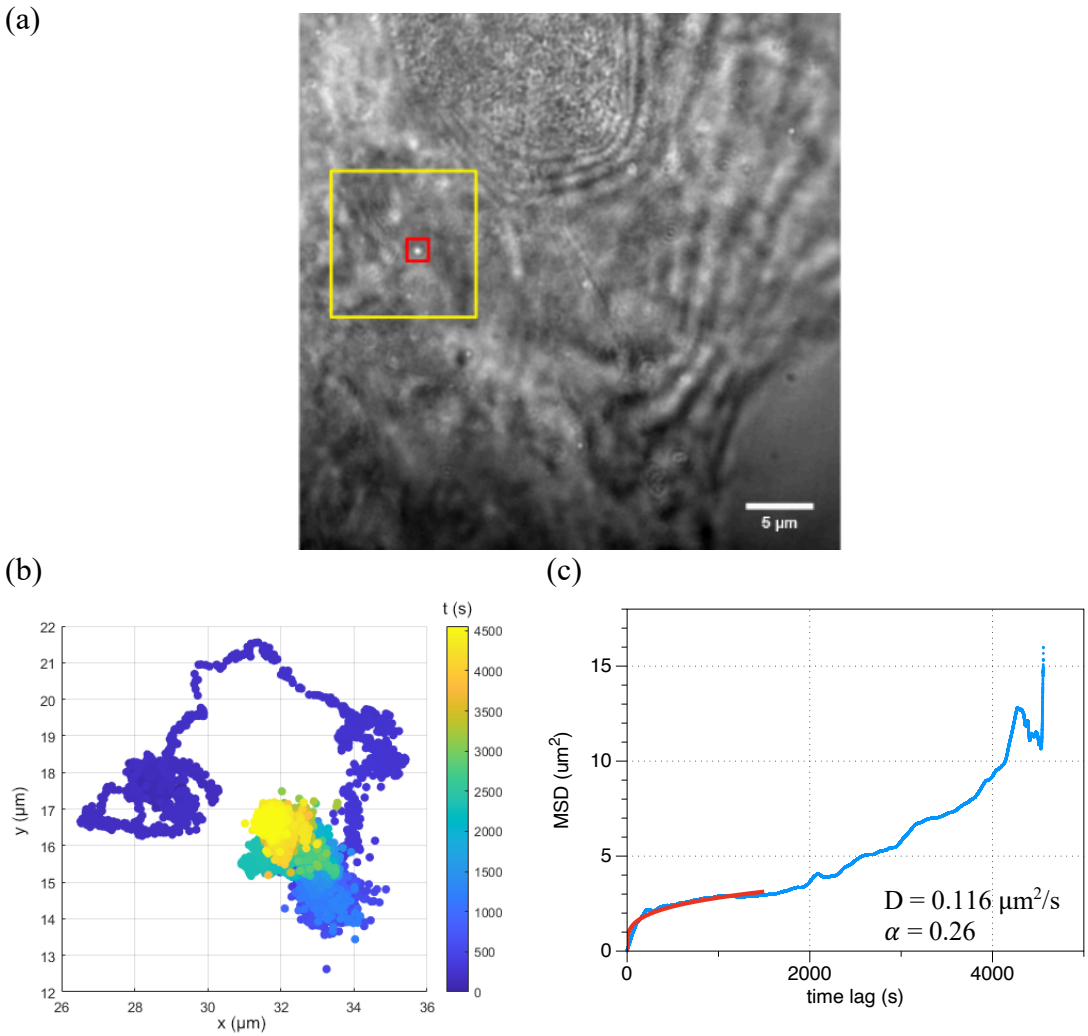

Figure 45: Tracking of PEG coated fND on U2OS cell membrane: (a) source recording with the tracked fND marked by red rectangle, yellow rectangle marks the area of the fND diffusion corresponding to the area in (b), (b) obtained trajectory after SPT, (c) MSD curve (blue) corresponding to the trajectory with fitting curve (red) and parameters D = 116 nm²/s and α = 0.26.

The first example in Figure 45 shows trajectory with very fast diffusion at start and PEG-fND traveling long distance without much entrapment at membrane pits. Subsequently, it gets trapped in several pits in a row for the majority of the recording. As a result, both the trajectory and the MSD curve suggest confined diffusion. However, the difference from the bare fND diffusion is the fast almost free diffusion along the membrane captured at the beginning of the trajectory and consequently significantly higher diffusion coefficient D = 116 nm2/s.

The second example in Figure 46 captures another PEG-fND in a shorter timescale. This time the entrapment in any pit is not very significant, the particle travels along the membrane in a directional manner in the long timescale. The MSD curve suggests anomalous diffusion in this case. Additionally, the diffusion coefficient (D = 29 nm2/s) is again higher than for bare fNDs.

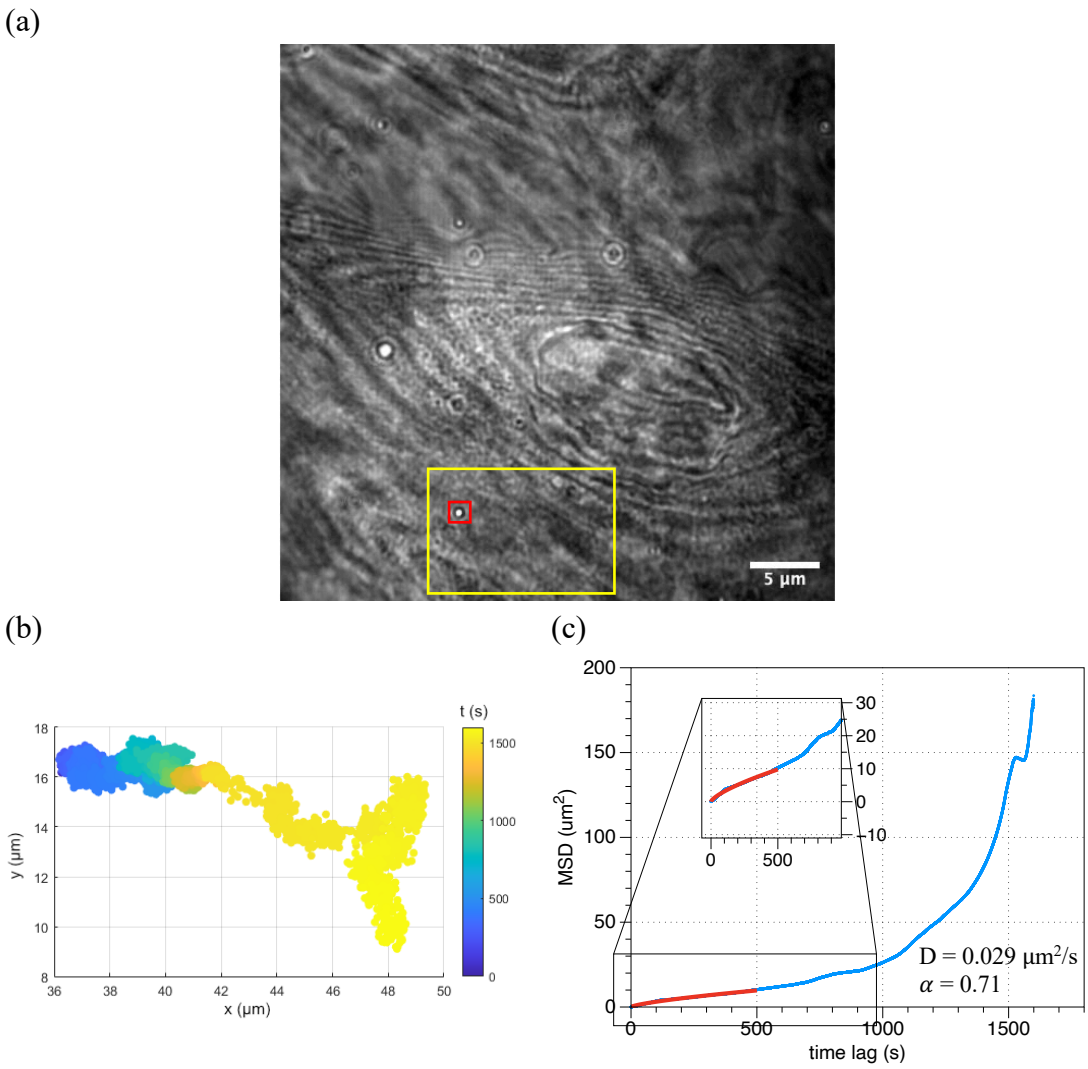

Figure 46: Tracking of PEG coated fND on U2OS cell membrane: (a) source recording with the tracked fND marked by red rectangle, yellow rectangle marks the area of the fND diffusion corresponding to the area in (b), (b) obtained trajectory after SPT, (c) MSD curve (blue) corresponding to the trajectory with fitting curve (red) and parameters D = 29 nm²/s and α = 0.71.

5.8 Diffusion dynamics of natural cell vesicles

As a complementary experiment, the natural cell vesicles of U2OS cells were monitored. The general observations were that

i) most of the vesicles are diffusing under the cell membrane and above the cell organelles,
ii) vesicles are moving along the cell filaments or freely
iii) their sizes range from tens to hundreds of nanometres and
iv) there is higher number of vesicles in cellular cytosol than in the nucleus.

Several types of diffusion were observed: free, confined, and directional. All three types were detected in the cytosol where majority of vesicles had similar diffusion coefficient independent of the type of motion. The average 2D diffusion coefficient was D(cytosol)avg = 13.8 nm2/s. Near the nucleus, confined or directional diffusion was detected, again with similar diffusion coefficients D(nucleus)avg = 0.9 nm2/s.

Comparing these findings to the results obtained for fNDs, the vesicle diffusion closer to the 10 nm fND diffusion than 100 nm fNDs.

5.9 Conclusions

As a promising technique for bioimaging, iSCAT was used to monitor the interaction between fNDs and living cells. The interaction was investigated for different sizes of fNDs, 100 nm and 10 nm, as well as different parts of the cell, membrane, cytosol and nucleus. First, it was observed that fNDs can be spontaneously internalized even by nonphagocytic cells like U2OS cells. Then, combining iSCAT and fluorescence detection enabled an unambiguous detection of very small particles down to size 10 nm and track them in real time on a long timescale. Based on these facts, the research proceeded to development of a tracking method and data evaluation.

The tracking in the cytosol showed differences between 10 and 100 nm fNDs. While 10 nm fNDs inclined more towards the free and confined diffusion, the 100 nm seemed to move notably faster and in more directional and confined motion. This signifies that particles of different size undergone different internalization mechanism to begin with and that larger fNDs are enclosed in vesicles whereas the smallest fNDs can diffuse through membrane without the need of active endocytosis process. Both sizes of fND also showed that they are able to enter the perinuclear space, however, they do not penetrate into the nucleus.

At the plasma membrane surface, all fNDs display corralled diffusion before entering the cell. Here, the importance of spatial and temporal resolution of SPT was demonstrated. Besides, the difference between bare and PEG coated fNDs interaction with plasma membrane was examined which revealed faster diffusion of PEG-fNDs along the membrane. Less affinity to irrelevant membrane pits of PEG-fND can be one of the reasons for the faster internalization rate of coated nanoparticles.

Lastly, the investigation of natural cell vesicles showed many similarities with fND diffusion in cytosol.

6 Thesis conclusions and outlook

This thesis presents a development of two consecutive methods, nanoparticle detection and characterization by axial profiling and theoretical modeling and nanoparticle tracking in living cells, as versatile tools for iSCAT microscopy. Those methods were then utilized for size characterization of fNDs that were used as probes for investigation of cell interaction with fNDs.

The size characterization by axial profiling consists of two parts. First is a practical part where the axial data of a single nanoparticle are collected by fluorescence combined iSCAT microscope that was especially upgraded for this purpose. The second part is the development of the theoretical model and data processing in MATLAB. In principle, this method uses the variation of scattering signal along the z focus range and fits the experimental data with a theoretical model. This enables to extract quantitative information about individual nanoparticles with nanometer accuracy. Additionally, considering it is a fully optical approach and compatible with aqueous environment, this technique stands out amongst the nanoparticle characterization techniques like TEM or AFM.[23]

This axial profiling technique can also be used for 3D bioimaging and tracking. Again, the investigation of fND-cell interaction was divided into two parts, the computational and the practical measurement. SPT software was written in MATLAB. The fluorescence combined iSCAT setup was modified for long-term measurement of living cells, methodology was established, and data collected. Finally, the trajectory data had to be analyzed to evaluate the fND diffusion behavior. The fND behavior and its differences inside and outside the cell are presented and discussed in great length in this work since there was many factors to unravel. Some of the main findings are that the large (100 nm) fNDs undergo an active endocytosis process and most often are transported in vesicles inside the cell. While the small (10 nm) fNDs enter the cell by passive uptake mechanism and diffuse without encapsulation inside the cell. However, both large and small fND travel in the direction of nucleus and both can enter the perinuclear area but not the nucleus itself. Additionally, the uptake rate and speed of diffusion was investigated for bare fNDs and functionalized fNDs. The results were also compared to the diffusion of natural cell vesicles that surprisingly resemble 10 nm fND diffusion in the cell. These findings can be useful in many areas of bioimaging or nanoparticle study, biosensors development, drug delivery or toxicity studies. One of the planned future projects is

mapping the internal structure of a nucleus with 10 nm fNDs. This method opens new possibilities in mapping biological structures, it enables direct observation of the mechanism of endocytosis or other biological mechanisms and offers SPT with nanometric accuracy and long-term measurement in general.

The main goal of this thesis was to develop a rigorous method for characterization of fNDs and studying their interaction with living cells. This goal was fulfilled together with all the partial objectives, i.e., construction of fluorescence combined iSCAT microscope, development of theoretical model for nanoparticle characterization, establishing a method for SPT in living cell by iSCAT and studying the endocytosis of fND and its fate in the cell. In addition to that, correlation of fND fluorescence intensity with its size was investigated, the effect of fND functionalization on the interaction with cell was analyzed, cell structures were identified by iSCAT and behavior of natural cell vesicles were explored.

List of publications

Articles in journals

[1] K. Žambochová, I.-B. Lee, J.-S. Park, S.-C. Hong, and M. Cho, 'Axial profiling of interferometric scattering enables an accurate determination of nanoparticle size', *Opt Express*, vol. 31, no. 6, p. 10101, Mar. 2023, doi: 10.1364/OE.480337.

[2] I.-B. Lee, H.-M. Moon, J.-S. Park, K. Zambochova, S.-C. Hong, and M. Cho, 'Three-dimensional interferometric scattering microscopy via remote focusing technique', *Opt Lett*, vol. 45, no. 9, p. 2628, May 2020, doi: 10.1364/OL.386172.

Conference contributions

Oral presentation + article in conference proceedings

[3] K. Žambochová, A. Patrochová, and D. Pánek, 'Physical stability of small unilamellar vesicles probed by fluorescence correlation spectroscopy'. In *Instruments and Methods for Biology and Medicine 2017*, p. 30–37, Kladno, 2017.

[4] K. Žambochová, J. Šimůnek, H. Sechovcová, H. and T. Jarošíková, 'Proteomic approach to extracellular enzymes of anaerobic xylanolytic bacteria'. in *Instruments and Methods for Biology and Medicine 2015*, Kladno, 2015.

Poster presentation

[5] K. Žambochová, J.-S. Park, I.-B. Lee, S.-C. Hong, and M. Cho, 'Diffusion dynamics of fluorescent nano-diamonds in living cells detected by fluorescence-combined iSCAT system', in *IBS conference on Advanced Optical Imaging*, Seoul, Jun. 2019.

References

[1] G. B. Airy, 'On the Diffraction of an Object-glass with Circular Aperture', *Transactions of the Cambridge Philosophical Society*, vol. 5, pp. 283–291, 1835.

[2] E. Abbe, 'Beiträge zur Theorie des Mikroskops und der mikroskopischen Wahrnehmung', *Archiv für Mikroskopische Anatomie*, vol. 9, no. 1, pp. 413–468, Dec. 1873, doi: 10.1007/BF02956173.

[3] J. W. Rayleigh, 'On the Theory of Optical Images, with Special Reference to the Microscope', *Philos. Mag. Ser. 5*, vol. 42, no. 255, pp. 167–195, 1896.

[4] J. W. Rayleigh, 'On the manufacture and theory of diffraction-gratings', *Philos. Mag. Ser. 4*, vol. 47, no. 310, pp. 81–93, 1874.

[5] M. A. Lauterbach, 'Finding, defining and breaking the diffraction barrier in microscopy – a historical perspective', *Opt Nanoscopy*, vol. 1, no. 1, p. 8, 2012, doi: 10.1186/2192-2853-1-8.

[6] S. W. Hell and J. Wichmann, 'Breaking the diffraction resolution limit by stimulated emission: stimulated-emission-depletion fluorescence microscopy', *Opt Lett*, vol. 19, no. 11, p. 780, Jun. 1994, doi: 10.1364/OL.19.000780.

[7] S. W. Hell and M. Kroug, 'Ground-state-depletion fluorscence microscopy: A concept for breaking the diffraction resolution limit', *Appl Phys B*, vol. 60, no. 5, pp. 495–497, May 1995, doi: 10.1007/BF01081333.

[8] E. Rittweger, K. Y. Han, S. E. Irvine, C. Eggeling, and S. W. Hell, 'STED microscopy reveals crystal colour centres with nanometric resolution', *Nat Photonics*, vol. 3, no. 3, pp. 144–147, Mar. 2009, doi: 10.1038/nphoton.2009.2.

[9] E. Rittweger, D. Wildanger, and S. W. Hell, 'Far-field fluorescence nanoscopy of diamond color centers by ground state depletion', *EPL (Europhysics Letters)*, vol. 86, no. 1, p. 14001, Apr. 2009, doi: 10.1209/0295-5075/86/14001.

[10] J. Enderlein, 'Breaking the diffraction limit with dynamic saturation optical microscopy', *Appl Phys Lett*, vol. 87, no. 9, Aug. 2005, doi: 10.1063/1.2034116.

[11] E. Betzig *et al.*, 'Imaging Intracellular Fluorescent Proteins at Nanometer Resolution', *Science (1979)*, vol. 313, no. 5793, pp. 1642–1645, Sep. 2006, doi: 10.1126/science.1127344.

[12] S. T. Hess, T. P. K. Girirajan, and M. D. Mason, 'Ultra-High Resolution Imaging by Fluorescence Photoactivation Localization Microscopy', *Biophys J*, vol. 91, no. 11, pp. 4258–4272, Dec. 2006, doi: 10.1529/biophysj.106.091116.

[13] M. J. Rust, M. Bates, and X. Zhuang, 'Sub-diffraction-limit imaging by stochastic optical reconstruction microscopy (STORM)', *Nat Methods*, vol. 3, no. 10, pp. 793–796, Oct. 2006, doi: 10.1038/nmeth929.

[14] X. Zhuang, 'Nano-imaging with STORM', *Nat Photonics*, vol. 3, no. 7, pp. 365–367, Jul. 2009, doi: 10.1038/nphoton.2009.101.

[15] R. Sharma, M. Singh, and R. Sharma, 'Recent advances in STED and RESOLFT super-resolution imaging techniques', *Spectrochim Acta A Mol Biomol Spectrosc*, vol. 231, p. 117715, Apr. 2020, doi: 10.1016/j.saa.2019.117715.

[16] Z. Chu *et al.*, 'Unambiguous observation of shape effects on cellular fate of nanoparticles', *Sci Rep*, vol. 4, no. 1, p. 4495, Mar. 2014, doi: 10.1038/srep04495.

[17] I.-B. Lee, H.-M. Moon, J.-S. Park, K. Zambochova, S.-C. Hong, and M. Cho, 'Three-dimensional interferometric scattering microscopy via remote focusing technique', *Opt Lett*, vol. 45, no. 9, p. 2628, May 2020, doi: 10.1364/OL.386172.

[18] J. Ortega Arroyo, D. Cole, and P. Kukura, ‘Interferometric scattering microscopy and its combination with single-molecule fluorescence imaging’, *Nat Protoc*, vol. 11, no. 4, pp. 617–633, Apr. 2016, doi: 10.1038/nprot.2016.022.
[19] J. Ortega-Arroyo and P. Kukura, ‘Interferometric scattering microscopy (iSCAT): new frontiers in ultrafast and ultrasensitive optical microscopy’, *Physical Chemistry Chemical Physics*, vol. 14, no. 45, p. 15625, 2012, doi: 10.1039/c2cp41013c.
[20] M. Piliarik and V. Sandoghdar, ‘Direct optical sensing of single unlabelled proteins and super-resolution imaging of their binding sites’, *Nat Commun*, vol. 5, no. 1, p. 4495, Jul. 2014, doi: 10.1038/ncomms5495.
[21] G. Young *et al.*, ‘Quantitative mass imaging of single biological macromolecules’, *Science (1979)*, vol. 360, no. 6387, pp. 423–427, Apr. 2018, doi: 10.1126/science.aar5839.
[22] K. Holanová, M. Vala, and M. Piliarik, ‘[INVITED] Optical imaging and localization of prospective scattering labels smaller than a single protein’, *Opt Laser Technol*, vol. 109, pp. 323–327, Jan. 2019, doi: 10.1016/j.optlastec.2018.08.014.
[23] K. Žambochová, I.-B. Lee, J.-S. Park, S.-C. Hong, and M. Cho, ‘Axial profiling of interferometric scattering enables an accurate determination of nanoparticle size’, *Opt Express*, vol. 31, no. 6, p. 10101, Mar. 2023, doi: 10.1364/OE.480337.
[24] R. Gholami Mahmoodabadi *et al.*, ‘Point spread function in interferometric scattering microscopy (iSCAT). Part I: aberrations in defocusing and axial localization’, *Opt Express*, vol. 28, no. 18, p. 25969, Aug. 2020, doi: 10.1364/OE.401374.
[25] M. Selmke, M. Braun, and F. Cichos, ‘Photothermal Single-Particle Microscopy: Detection of a Nanolens’, *ACS Nano*, vol. 6, no. 3, pp. 2741–2749, Mar. 2012, doi: 10.1021/nn300181h.
[26] M. Selmke, ‘Photothermal Single Particle Detection in Theory & Experiments’, Ph.D. thesis, Leipzig University, 2013.
[27] O. Avci, R. Adato, A. Y. Ozkumur, and M. S. Ünlü, ‘Physical modeling of interference enhanced imaging and characterization of single nanoparticles’, *Opt Express*, vol. 24, no. 6, p. 6094, Mar. 2016, doi: 10.1364/OE.24.006094.
[28] G. Young and P. Kukura, ‘The Annual Review of Physical Chemistry is online at’, *Annu. Rev. Phys. Chem*, vol. 70, pp. 301–322, 2019, doi: 10.1146/annurev-physchem-050317.
[29] J. Andrecka *et al.*, ‘Interferometric Scattering Microscopy for the Study of Molecular Motors’, 2016, pp. 517–539. doi: 10.1016/bs.mie.2016.08.016.
[30] W. Neuhauser, M. Hohenstatt, P. E. Toschek, and H. Dehmelt, ‘Localized visible Ba+ mono-ion oscillator’, *Phys Rev A (Coll Park)*, vol. 22, no. 3, pp. 1137–1140, Sep. 1980, doi: 10.1103/PhysRevA.22.1137.
[31] W. E. Moerner and L. Kador, ‘Optical detection and spectroscopy of single molecules in a solid’, *Phys Rev Lett*, vol. 62, no. 21, pp. 2535–2538, May 1989, doi: 10.1103/PhysRevLett.62.2535.
[32] H. Siedentopf and R. Zsigmondy, ‘Uber Sichtbarmachung und Größenbestimmung ultramikoskopischer Teilchen, mit besonderer Anwendung auf Goldrubingläser’, *Ann Phys*, vol. 315, no. 1, pp. 1–39, 1902, doi: 10.1002/andp.19023150102.
[33] A. Straube, ‘How to Measure Microtubule Dynamics?’, 2011, pp. 1–14. doi: 10.1007/978-1-61779-252-6_1.

[34] B. Redding, M. A. Choma, and H. Cao, ‘Speckle-free laser imaging using random laser illumination’, *Nat Photonics*, vol. 6, no. 6, pp. 355–359, Jun. 2012, doi: 10.1038/nphoton.2012.90.
[35] E. Abbe, ‘Beiträge zur Theorie des Mikroskops und der mikroskopischen Wahrnehmung’, *Archiv für Mikroskopische Anatomie*, vol. 9, no. 1, pp. 413–468, Dec. 1873, doi: 10.1007/BF02956173.
[36] G. Janke, C. Larivé, and A. Tailland, ‘Measurements of Instantaneous Flow Angles by Optical Detection of the Thermal Wake of a Hot Wire’, in *Advances in Turbulence 2*, Berlin, Heidelberg: Springer Berlin Heidelberg, 1989, pp. 298–303. doi: 10.1007/978-3-642-83822-4_46.
[37] G. Nomarski, ‘Microinterféromètre différentiel à ondes polarisées’, *J. Phys. Radium*, vol. 16, pp. 9S-11S, 1955.
[38] R. D. Allen, G. B. David, and G. Nomarski, ‘The zeiss-Nomarski differential interference equipment for transmitted-light microscopy.’, *Z Wiss Mikrosk*, vol. 69, no. 4, pp. 193–221, Nov. 1969.
[39] T. Kim *et al.*, ‘White-light diffraction tomography of unlabelled live cells’, *Nat Photonics*, vol. 8, no. 3, pp. 256–263, Mar. 2014, doi: 10.1038/nphoton.2013.350.
[40] Y. Cotte *et al.*, ‘Marker-free phase nanoscopy’, *Nat Photonics*, vol. 7, no. 2, pp. 113–117, Feb. 2013, doi: 10.1038/nphoton.2012.329.
[41] A. S. G. Curtis, ‘THE MECHANISM OF ADHESION OF CELLS TO GLASS’, *Journal of Cell Biology*, vol. 20, no. 2, pp. 199–215, Feb. 1964, doi: 10.1083/jcb.20.2.199.
[42] A. Vasicek, *Optics of thin films*. Amsterdam: North-Holland Publishing Company, 1960.
[43] M. Van den Tempel, ‘Distance between emulsified oil globules upon coalescence’, *J Colloid Sci*, vol. 13, no. 2, pp. 125–133, Apr. 1958, doi: 10.1016/0095-8522(58)90015-1.
[44] L. A. AMOS and W. B. AMOS, ‘The bending of sliding microtubules imaged by confocal light microscopy and negative stain electron microscopy’, *J Cell Sci*, vol. 1991, no. Supplement_14, pp. 95–101, Jan. 1991, doi: 10.1242/jcs.1991.Supplement_14.20.
[45] T. J. Filler and E. T. Peuker, ‘Reflection contrast microscopy (RCM): a forgotten technique?’, *J Pathol*, vol. 190, no. 5, pp. 635–638, Apr. 2000, doi: 10.1002/(SICI)1096-9896(200004)190:5<635::AID-PATH571>3.0.CO;2-E.
[46] D. Gingell and I. Todd, ‘Interference reflection microscopy. A quantitative theory for image interpretation and its application to cell-substratum separation measurement’, *Biophys J*, vol. 26, no. 3, pp. 507–526, Jun. 1979, doi: 10.1016/S0006-3495(79)85268-6.
[47] L. Limozin and K. Sengupta, ‘Quantitative Reflection Interference Contrast Microscopy (RICM) in Soft Matter and Cell Adhesion’, *ChemPhysChem*, vol. 10, no. 16, pp. 2752–2768, Nov. 2009, doi: 10.1002/cphc.200900601.
[48] J. Raedler, H. Strey, and E. Sackmann, ‘Phenomenology and Kinetics of Lipid Bilayer Spreading on Hydrophilic Surfaces’, *Langmuir*, vol. 11, no. 11, pp. 4539–4548, Nov. 1995, doi: 10.1021/la00011a058.
[49] J. Rädler and E. Sackmann, ‘Imaging optical thicknesses and separation distances of phospholipid vesicles at solid surfaces’, *Journal de Physique II*, vol. 3, no. 5, pp. 727–748, May 1993, doi: 10.1051/jp2:1993163.

[50] D. Dulin, S. Barland, X. Hachair, and F. Pedaci, ‘Efficient Illumination for Microsecond Tracking Microscopy’, *PLoS One*, vol. 9, no. 9, p. e107335, Sep. 2014, doi: 10.1371/journal.pone.0107335.
[51] K. Lindfors, T. Kalkbrenner, P. Stoller, and V. Sandoghdar, ‘Detection and Spectroscopy of Gold Nanoparticles Using Supercontinuum White Light Confocal Microscopy’, *Phys Rev Lett*, vol. 93, no. 3, p. 037401, Jul. 2004, doi: 10.1103/PhysRevLett.93.037401.
[52] H. Ewers, V. Jacobsen, E. Klotzsch, A. E. Smith, A. Helenius, and V. Sandoghdar, ‘Label-Free Optical Detection and Tracking of Single Virions Bound to Their Receptors in Supported Membrane Bilayers’, *Nano Lett*, vol. 7, no. 8, pp. 2263–2266, Aug. 2007, doi: 10.1021/nl070766y.
[53] P. Kukura, H. Ewers, C. Müller, A. Renn, A. Helenius, and V. Sandoghdar, ‘High-speed nanoscopic tracking of the position and orientation of a single virus’, *Nat Methods*, vol. 6, no. 12, pp. 923–927, Dec. 2009, doi: 10.1038/nmeth.1395.
[54] Y.-H. Lin, W.-L. Chang, and C.-L. Hsieh, ‘Shot-noise limited localization of single 20 nm gold particles with nanometer spatial precision within microseconds’, *Opt Express*, vol. 22, no. 8, p. 9159, Apr. 2014, doi: 10.1364/OE.22.009159.
[55] C.-L. Hsieh, S. Spindler, J. Ehrig, and V. Sandoghdar, ‘Tracking Single Particles on Supported Lipid Membranes: Multimobility Diffusion and Nanoscopic Confinement’, *J Phys Chem B*, vol. 118, no. 6, pp. 1545–1554, Feb. 2014, doi: 10.1021/jp412203t.
[56] S. Spindler *et al.*, ‘Visualization of lipids and proteins at high spatial and temporal resolution via interferometric scattering (iSCAT) microscopy’, *J Phys D Appl Phys*, vol. 49, no. 27, p. 274002, Jul. 2016, doi: 10.1088/0022-3727/49/27/274002.
[57] J. Ortega Arroyo *et al.*, ‘Label-Free, All-Optical Detection, Imaging, and Tracking of a Single Protein’, *Nano Lett*, vol. 14, no. 4, pp. 2065–2070, Apr. 2014, doi: 10.1021/nl500234t.
[58] M. P. McDonald *et al.*, ‘Visualizing Single-Cell Secretion Dynamics with Single-Protein Sensitivity’, *Nano Lett*, vol. 18, no. 1, pp. 513–519, Jan. 2018, doi: 10.1021/acs.nanolett.7b04494.
[59] V. Jacobsen, P. Stoller, C. Brunner, V. Vogel, and V. Sandoghdar, ‘Interferometric optical detection and tracking of very small gold nanoparticles at a water-glass interface’, *Opt Express*, vol. 14, no. 1, p. 405, 2006, doi: 10.1364/OPEX.14.000405.
[60] J. Andrecka, J. Ortega Arroyo, K. Lewis, R. A. Cross, and P. Kukura, ‘Label-free Imaging of Microtubules with Sub-nm Precision Using Interferometric Scattering Microscopy’, *Biophys J*, vol. 110, no. 1, pp. 214–217, Jan. 2016, doi: 10.1016/j.bpj.2015.10.055.
[61] K. J. Mickolajczyk, N. C. Deffenbaugh, J. Ortega Arroyo, J. Andrecka, P. Kukura, and W. O. Hancock, ‘Kinetics of nucleotide-dependent structural transitions in the kinesin-1 hydrolysis cycle’, *Proceedings of the National Academy of Sciences*, vol. 112, no. 52, Dec. 2015, doi: 10.1073/pnas.1517638112.
[62] J. Andrecka *et al.*, ‘Structural dynamics of myosin 5 during processive motion revealed by interferometric scattering microscopy’, *Elife*, vol. 4, Mar. 2015, doi: 10.7554/eLife.05413.

[63] Y.-F. Huang, G.-Y. Zhuo, C.-Y. Chou, C.-H. Lin, and C.-L. Hsieh, 'Label-free, ultrahigh-speed, 3D observation of bidirectional and correlated intracellular cargo transport by coherent brightfield microscopy', *Nanoscale*, vol. 9, no. 19, pp. 6567–6574, 2017, doi: 10.1039/C7NR00604G.
[64] R. W. Taylor, R. G. Mahmoodabadi, V. Rauschenberger, A. Giessl, A. Schambony, and V. Sandoghdar, 'Interferometric scattering microscopy reveals microsecond nanoscopic protein motion on a live cell membrane', *Nat Photonics*, vol. 13, no. 7, pp. 480–487, Jul. 2019, doi: 10.1038/s41566-019-0414-6.
[65] J.-S. Park *et al.*, 'Label-free and live cell imaging by interferometric scattering microscopy', *Chem Sci*, vol. 9, no. 10, pp. 2690–2697, 2018, doi: 10.1039/C7SC04733A.
[66] J.-S. Park *et al.*, 'Fluorescence-Combined Interferometric Scattering Imaging Reveals Nanoscale Dynamic Events of Single Nascent Adhesions in Living Cells', *J Phys Chem Lett*, vol. 11, no. 23, pp. 10233–10241, Dec. 2020, doi: 10.1021/acs.jpclett.0c02103.
[67] I.-B. Lee, H.-M. Moon, J.-H. Joo, K.-H. Kim, S.-C. Hong, and M. Cho, 'Interferometric Scattering Microscopy with Polarization-Selective Dual Detection Scheme: Capturing the Orientational Information of Anisotropic Nanometric Objects', *ACS Photonics*, vol. 5, no. 3, pp. 797–804, Mar. 2018, doi: 10.1021/acsphotonics.7b00890.
[68] Z. Shi, J. Huang, X. Huang, Y. Huang, L. Wu, and Q. Li, 'Resonant scattering enhanced interferometric scattering microscopy', *Nanoscale*, vol. 12, no. 14, pp. 7969–7975, 2020, doi: 10.1039/C9NR10391K.
[69] Y.-F. Huang, G.-Y. Zhuo, C.-Y. Chou, C.-H. Lin, W. Chang, and C.-L. Hsieh, 'Coherent Brightfield Microscopy Provides the Spatiotemporal Resolution To Study Early Stage Viral Infection in Live Cells', *ACS Nano*, vol. 11, no. 3, pp. 2575–2585, Mar. 2017, doi: 10.1021/acsnano.6b05601.
[70] C. F. Bohren and D. R. Huffman, *Absorption and Scattering of Light by Small Particles*. Wiley, 1998. doi: 10.1002/9783527618156.
[71] R. W. Taylor and V. Sandoghdar, 'Interferometric Scattering Microscopy: Seeing Single Nanoparticles and Molecules via Rayleigh Scattering', *Nano Lett*, vol. 19, no. 8, pp. 4827–4835, Aug. 2019, doi: 10.1021/acs.nanolett.9b01822.
[72] F. Aguet, 'Super-Resolution Fluorescence Microscopy Based on Physical Models', EPFL, 2009. [Online]. Available: http://bigwww.epfl.ch/
[73] E. Wolf, 'Electromagnetic diffraction in optical systems - I. An integral representation of the image field', *Proc R Soc Lond A Math Phys Sci*, vol. 253, no. 1274, pp. 349–357, Dec. 1959, doi: 10.1098/rspa.1959.0199.
[74] B. Richards and E. Wolf, 'Electromagnetic diffraction in optical systems II. Structure of the image field in an aplanatic system', *Proc R Soc Lond A Math Phys Sci*, vol. 253, no. 1274, pp. 358–379, 1959.
[75] P. Török and P. Varga, 'Electromagnetic diffraction of light focused through a stratified medium', *Appl Opt*, vol. 36, no. 11, p. 2305, Apr. 1997, doi: 10.1364/AO.36.002305.
[76] P. Török, P. D. Higdon, and T. Wilson, 'On the general properties of polarised light conventional and confocal microscopes', *Opt Commun*, vol. 148, no. 4–6, pp. 300–315, Mar. 1998, doi: 10.1016/S0030-4018(97)00576-2.
[77] P. Török, P. Varga, Z. Laczik, and G. R. Booker, 'Electromagnetic diffraction of light focused through a planar interface between materials of mismatched refractive indices: an integral representation', *Journal of the Optical Society of America A*, vol. 12, no. 2, p. 325, Feb. 1995, doi: 10.1364/JOSAA.12.000325.

[78] S. HELL, G. REINER, C. CREMER, and E. H. K. STELZER, ‘Aberrations in confocal fluorescence microscopy induced by mismatches in refractive index’, *J Microsc*, vol. 169, no. 3, pp. 391–405, Mar. 1993, doi: 10.1111/j.1365-2818.1993.tb03315.x.
[79] S. F. Gibson and F. Lanni, ‘Experimental test of an analytical model of aberration in an oil-immersion objective lens used in three-dimensional light microscopy’, *J. Opt. Soc. Am. A*, vol. 9, no. 1, pp. 154–166, Jan. 1992.
[80] M. Born and E. Wolf, *Principles of Optics*, Sixth ed. London: Pergamon, 1991.
[81] H. H. Hopkins, ‘The frequency response of a defocused optical system’, *Proc R Soc Lond A Math Phys Sci*, vol. 231, no. 1184, pp. 91–103, Jul. 1955, doi: 10.1098/rspa.1955.0158.
[82] O. Haeberlé, ‘Focusing of light through a stratified medium: a practical approach for computing microscope point spread functions. Part I: Conventional microscopy’, *Opt Commun*, vol. 216, no. 1–3, pp. 55–63, Feb. 2003, doi: 10.1016/S0030-4018(02)02282-4.
[83] J. Li, F. Xue, and T. Blu, ‘Fast and accurate three-dimensional point spread function computation for fluorescence microscopy’, *Journal of the Optical Society of America A*, vol. 34, no. 6, p. 1029, Jun. 2017, doi: 10.1364/JOSAA.34.001029.
[84] B. T. Miles, A. B. Greenwood, B. R. Patton, and H. Gersen, ‘All-Optical Method for Characterizing Individual Fluorescent Nanodiamonds’, *ACS Photonics*, vol. 3, no. 3, pp. 343–348, Mar. 2016, doi: 10.1021/acsphotonics.5b00732.
[85] C. A. Mack and C.-B. Juang, ‘ Comparison of Scalar and Vector Modeling of Image Formation in Photoresist’, *Proc. SPIE, Optical/Laser Microlithography VIII*, vol. 2440, pp. 381–394, 1995.
[86] J. Dong, D. Maestre, C. Conrad-Billroth, and T. Juffmann, ‘Fundamental bounds on the precision of iSCAT, COBRI and dark-field microscopy for 3D localization and mass photometry’, *J Phys D Appl Phys*, vol. 54, no. 39, p. 394002, Sep. 2021, doi: 10.1088/1361-6463/ac0f22.
[87] J. Kim, Y. Wang, and X. Zhang, ‘Calculation of vectorial diffraction in optical systems’, *Journal of the Optical Society of America A*, vol. 35, no. 4, p. 526, Apr. 2018, doi: 10.1364/josaa.35.000526.
[88] J. Kim, ‘High-Aperture Optical Microscopy Methods for Super-Resolution Deep Imaging and Quantitative Phase Imaging’, University of California, 2016.
[89] O. Haeberlé, M. Ammar, H. Furukawa, K. Tenjimbayashi, and P. Török, ‘Point spread function of optical microscopes imaging through stratified media’, *Opt Express*, vol. 11, no. 22, p. 2964, Nov. 2003, doi: 10.1364/OE.11.002964.
[90] W. Yang, J. Gelles, and S. M. Musser, ‘Imaging of single-molecule translocation through nuclear pore complexes’, *Proceedings of the National Academy of Sciences*, vol. 101, no. 35, pp. 12887–12892, Aug. 2004, doi: 10.1073/pnas.0403675101.
[91] M. Goulian and S. M. Simon, ‘Tracking Single Proteins within Cells’, *Biophys J*, vol. 79, no. 4, pp. 2188–2198, Oct. 2000, doi: 10.1016/S0006-3495(00)76467-8.
[92] A. D. Mehta, M. Rief, J. A. Spudich, D. A. Smith, and R. M. Simmons, ‘Single-Molecule Biomechanics with Optical Methods’, *Science (1979)*, vol. 283, no. 5408, pp. 1689–1695, Mar. 1999, doi: 10.1126/science.283.5408.1689.
[93] G. de Wit, D. Albrecht, H. Ewers, and P. Kukura, ‘Revealing Compartmentalized Diffusion in Living Cells with Interferometric Scattering Microscopy’, *Biophys J*, vol. 114, no. 12, pp. 2945–2950, Jun. 2018, doi: 10.1016/j.bpj.2018.05.007.

[94] R. Y. Tsien, ‘THE GREEN FLUORESCENT PROTEIN’, *Annu Rev Biochem*, vol. 67, no. 1, pp. 509–544, Jun. 1998, doi: 10.1146/annurev.biochem.67.1.509.
[95] C.-Y. Cheng and C.-L. Hsieh, ‘Background Estimation and Correction for High-Precision Localization Microscopy’, *ACS Photonics*, vol. 4, no. 7, pp. 1730–1739, Jul. 2017, doi: 10.1021/acsphotonics.7b00238.
[96] H.-M. Wu, Y.-H. Lin, T.-C. Yen, and C.-L. Hsieh, ‘Nanoscopic substructures of raft-mimetic liquid-ordered membrane domains revealed by high-speed single-particle tracking’, *Sci Rep*, vol. 6, no. 1, p. 20542, Feb. 2016, doi: 10.1038/srep20542.
[97] S. Watanabe and E. Boucrot, ‘Fast and ultrafast endocytosis’, *Curr Opin Cell Biol*, vol. 47, pp. 64–71, Aug. 2017, doi: 10.1016/j.ceb.2017.02.013.
[98] M. M. Brockmann and C. Rosenmund, ‘Catching Up with Ultrafast Endocytosis’, *Neuron*, vol. 90, no. 3, pp. 423–424, May 2016, doi: 10.1016/j.neuron.2016.04.027.
[99] T. H. Ogunmowo *et al.*, ‘Membrane compression by synaptic vesicle exocytosis triggers ultrafast endocytosis’, *Nat Commun*, vol. 14, no. 1, p. 2888, May 2023, doi: 10.1038/s41467-023-38595-2.
[100] K. M. Spillane *et al.*, ‘High-Speed Single-Particle Tracking of GM1 in Model Membranes Reveals Anomalous Diffusion due to Interleaflet Coupling and Molecular Pinning’, *Nano Lett*, vol. 14, no. 9, pp. 5390–5397, Sep. 2014, doi: 10.1021/nl502536u.
[101] Z. Ye, X. Wang, and L. Xiao, ‘Single-Particle Tracking with Scattering-Based Optical Microscopy’, *Anal Chem*, vol. 91, no. 24, pp. 15327–15334, Dec. 2019, doi: 10.1021/acs.analchem.9b02760.
[102] A. Yildiz, J. N. Forkey, S. A. McKinney, T. Ha, Y. E. Goldman, and P. R. Selvin, ‘Myosin V Walks Hand-Over-Hand: Single Fluorophore Imaging with 1.5-nm Localization’, *Science (1979)*, vol. 300, no. 5628, pp. 2061–2065, Jun. 2003, doi: 10.1126/science.1084398.
[103] J. Liu *et al.*, ‘Single-Particle Tracking Reveals the Sequential Entry Process of the Bunyavirus Severe Fever with Thrombocytopenia Syndrome Virus’, *Small*, vol. 15, no. 6, p. 1803788, Feb. 2019, doi: 10.1002/smll.201803788.
[104] L. Wei, Z. Ye, Y. Xu, B. Chen, E. S. Yeung, and L. Xiao, ‘Single Particle Tracking of Peptides-Modified Nanocargo on Lipid Membrane Revealing Bulk-Mediated Diffusion’, *Anal Chem*, vol. 88, no. 24, pp. 11973–11977, Dec. 2016, doi: 10.1021/acs.analchem.6b03420.
[105] L. Xiao, L. Wei, C. Liu, Y. He, and E. S. Yeung, ‘Unsynchronized Translational and Rotational Diffusion of Nanocargo on a Living Cell Membrane’, *Angewandte Chemie International Edition*, vol. 51, no. 17, pp. 4181–4184, Apr. 2012, doi: 10.1002/anie.201108647.
[106] C. Manzo and M. F. Garcia-Parajo, ‘A review of progress in single particle tracking: from methods to biophysical insights’, *Reports on Progress in Physics*, vol. 78, no. 12, p. 124601, Dec. 2015, doi: 10.1088/0034-4885/78/12/124601.
[107] F. Pinaud, X. Michalet, G. Iyer, E. Margeat, H.-P. Moore, and S. Weiss, ‘Dynamic partitioning of a glycosyl-phosphatidylinositol-anchored protein in glycosphingolipid-rich microdomains imaged by single-quantum dot tracking.’, *Traffic*, vol. 10, no. 6, pp. 691–712, Jun. 2009, doi: 10.1111/j.1600-0854.2009.00902.x.
[108] M. J. Saxton and K. Jacobson, ‘SINGLE-PARTICLE TRACKING: Applications to Membrane Dynamics’, 1997. [Online]. Available: www.annualreviews.org

[109] K. Jaqaman *et al.*, 'Robust single-particle tracking in live-cell time-lapse sequences', *Nat Methods*, vol. 5, no. 8, pp. 695–702, Aug. 2008, doi: 10.1038/nmeth.1237.
[110] Z. Ye, X. Wang, and L. Xiao, 'Single-Particle Tracking with Scattering-Based Optical Microscopy', *Anal Chem*, vol. 91, no. 24, pp. 15327–15334, Dec. 2019, doi: 10.1021/acs.analchem.9b02760.
[111] H. Qian, M. P. Sheetz, and E. L. Elson, 'Single particle tracking. Analysis of diffusion and flow in two-dimensional systems', *Biophys J*, vol. 60, no. 4, pp. 910–921, Oct. 1991, doi: 10.1016/S0006-3495(91)82125-7.
[112] S. Zhang, H. Gao, and G. Bao, 'Physical Principles of Nanoparticle Cellular Endocytosis', *ACS Nano*, vol. 9, no. 9. American Chemical Society, pp. 8655–8671, Sep. 22, 2015. doi: 10.1021/acsnano.5b03184.
[113] J. A. Swanson, 'Shaping cups into phagosomes and macropinosomes', *Nat Rev Mol Cell Biol*, vol. 9, no. 8, pp. 639–649, Aug. 2008, doi: 10.1038/nrm2447.
[114] S. Behzadi *et al.*, 'Cellular uptake of nanoparticles: journey inside the cell', *Chem Soc Rev*, vol. 46, no. 14, pp. 4218–4244, 2017, doi: 10.1039/C6CS00636A.
[115] P. Foroozandeh and A. A. Aziz, 'Insight into Cellular Uptake and Intracellular Trafficking of Nanoparticles', *Nanoscale Research Letters*, vol. 13. Springer New York LLC, 2018. doi: 10.1186/s11671-018-2728-6.
[116] T. F. Roth and K. R. Porter, 'YOLK PROTEIN UPTAKE IN THE OOCYTE OF THE MOSQUITO AEDES AEGYPTI. L', *Journal of Cell Biology*, vol. 20, no. 2, pp. 313–332, Feb. 1964, doi: 10.1083/jcb.20.2.313.
[117] M. Marsh and A. Helenius, 'Virus Entry: Open Sesame', *Cell*, vol. 124, no. 4, pp. 729–740, Feb. 2006, doi: 10.1016/j.cell.2006.02.007.
[118] J. Mercer, M. Schelhaas, and A. Helenius, 'Virus Entry by Endocytosis', *Annu Rev Biochem*, vol. 79, no. 1, pp. 803–833, Jun. 2010, doi: 10.1146/annurev-biochem-060208-104626.
[119] O. Faklaris *et al.*, 'Photoluminescent Diamond Nanoparticles for Cell Labeling: Study of the Uptake Mechanism in Mammalian Cells', *ACS Nano*, vol. 3, no. 12, pp. 3955–3962, Dec. 2009, doi: 10.1021/nn901014j.
[120] G. E. PALADE, 'AN ELECTRON MICROSCOPE STUDY OF THE MITOCHONDRIAL STRUCTURE', *Journal of Histochemistry & Cytochemistry*, vol. 1, no. 4, pp. 188–211, Jul. 1953, doi: 10.1177/1.4.188.
[121] E. Yamada, 'THE FINE STRUCTURE OF THE GALL BLADDER EPITHELIUM OF THE MOUSE', *J Biophys Biochem Cytol*, vol. 1, no. 5, pp. 445–458, Sep. 1955, doi: 10.1083/jcb.1.5.445.
[122] J. Lin and A. Alexander-Katz, 'Cell Membranes Open "Doors" for Cationic Nanoparticles/Biomolecules: Insights into Uptake Kinetics', *ACS Nano*, vol. 7, no. 12, pp. 10799–10808, Dec. 2013, doi: 10.1021/nn4040553.
[123] H. Zhang *et al.*, 'Cooperative Transmembrane Penetration of Nanoparticles', *Sci Rep*, vol. 5, no. 1, p. 10525, May 2015, doi: 10.1038/srep10525.
[124] K. Yang and Y.-Q. Ma, 'Computer simulation of the translocation of nanoparticles with different shapes across a lipid bilayer', *Nat Nanotechnol*, vol. 5, no. 8, pp. 579–583, Aug. 2010, doi: 10.1038/nnano.2010.141.
[125] J. Wong-Ekkabut, S. Baoukina, W. Triampo, I.-M. Tang, D. P. Tieleman, and L. Monticelli, 'Computer simulation study of fullerene translocation through lipid membranes', *Nat Nanotechnol*, vol. 3, no. 6, pp. 363–368, Jun. 2008, doi: 10.1038/nnano.2008.130.

[126] H. Ding, W. Tian, and Y. Ma, 'Designing Nanoparticle Translocation through Membranes by Computer Simulations', *ACS Nano*, vol. 6, no. 2, pp. 1230–1238, Feb. 2012, doi: 10.1021/nn2038862.
[127] Y. Deng *et al.*, 'The effect of hyperbranched polyglycerol coatings on drug delivery using degradable polymer nanoparticles', *Biomaterials*, vol. 35, no. 24, pp. 6595–6602, Aug. 2014, doi: 10.1016/j.biomaterials.2014.04.038.
[128] J. Hu and Y. Liu, 'Cyclic Strain Enhances Cellular Uptake of Nanoparticles', *J Nanomater*, vol. 2015, pp. 1–8, 2015, doi: 10.1155/2015/953584.
[129] P. E. MacDonald, L. Eliasson, and P. Rorsman, 'Calcium increases endocytotic vesicle size and accelerates membrane fission in insulin-secreting INS-1 cells', *J Cell Sci*, vol. 118, no. 24, pp. 5911–5920, Dec. 2005, doi: 10.1242/jcs.02685.
[130] M. Morita, T. Tachikawa, S. Seino, K. Tanaka, and T. Majima, 'Controlled Synthesis of Gold Nanoparticles on Fluorescent Nanodiamond via Electron-Beam-Induced Reduction Method for Dual-Modal Optical and Electron Bioimaging', *ACS Appl Nano Mater*, vol. 1, no. 1, pp. 355–363, Jan. 2018, doi: 10.1021/acsanm.7b00213.
[131] C.-Y. Fang *et al.*, 'The Exocytosis of Fluorescent Nanodiamond and Its Use as a Long-Term Cell Tracker', *Small*, vol. 7, no. 23, pp. 3363–3370, Dec. 2011, doi: 10.1002/smll.201101233.
[132] N. Lewinski, V. Colvin, and R. Drezek, 'Cytotoxicity of Nanoparticles', *Small*, vol. 4, no. 1, pp. 26–49, Jan. 2008, doi: 10.1002/smll.200700595.
[133] R. Hardman, 'A Toxicologic Review of Quantum Dots: Toxicity Depends on Physicochemical and Environmental Factors', *Environ Health Perspect*, vol. 114, no. 2, pp. 165–172, Feb. 2006, doi: 10.1289/ehp.8284.
[134] V. Vaijayanthimala, Y.-K. Tzeng, H.-C. Chang, and C.-L. Li, 'The biocompatibility of fluorescent nanodiamonds and their mechanism of cellular uptake', *Nanotechnology*, vol. 20, no. 42, p. 425103, Oct. 2009, doi: 10.1088/0957-4484/20/42/425103.
[135] M.-F. Weng, B.-J. Chang, S.-Y. Chiang, N.-S. Wang, and H. Niu, 'Cellular uptake and phototoxicity of surface-modified fluorescent nanodiamonds', *Diam Relat Mater*, vol. 22, pp. 96–104, Feb. 2012, doi: 10.1016/j.diamond.2011.12.035.
[136] C.-C. Fu *et al.*, 'Characterization and application of single fluorescent nanodiamonds as cellular biomarkers', *Proceedings of the National Academy of Sciences*, vol. 104, no. 3, pp. 727–732, Jan. 2007, doi: 10.1073/pnas.0605409104.
[137] Y. Y. Hui, C.-L. Cheng, and H.-C. Chang, 'Nanodiamonds for optical bioimaging', *J Phys D Appl Phys*, vol. 43, no. 37, p. 374021, Sep. 2010, doi: 10.1088/0022-3727/43/37/374021.
[138] C. Bradac, T. Gaebel, N. Naidoo, J. R. Rabeau, and Amanda. S. Barnard, 'Prediction and Measurement of the Size-Dependent Stability of Fluorescence in Diamond over the Entire Nanoscale', *Nano Lett*, vol. 9, no. 10, pp. 3555–3564, Oct. 2009, doi: 10.1021/nl9017379.
[139] S.-J. Yu, M.-W. Kang, H.-C. Chang, K.-M. Chen, and Y.-C. Yu, 'Bright Fluorescent Nanodiamonds: No Photobleaching and Low Cytotoxicity', *J Am Chem Soc*, vol. 127, no. 50, pp. 17604–17605, Dec. 2005, doi: 10.1021/ja0567081.
[140] G. Davies, 'Vibronic spectra in diamond', *Journal of Physics C: Solid State Physics*, vol. 7, no. 20, pp. 3797–3809, Oct. 1974, doi: 10.1088/0022-3719/7/20/019.

[141] N. Mohan, C.-S. Chen, H.-H. Hsieh, Y.-C. Wu, and H.-C. Chang, 'In Vivo Imaging and Toxicity Assessments of Fluorescent Nanodiamonds in *Caenorhabditis elegans*', *Nano Lett*, vol. 10, no. 9, pp. 3692–3699, Sep. 2010, doi: 10.1021/nl1021909.
[142] J. Stursa *et al.*, 'Mass production of fluorescent nanodiamonds with a narrow emission intensity distribution', *Carbon N Y*, vol. 96, pp. 812–818, Jan. 2016, doi: 10.1016/j.carbon.2015.09.111.
[143] O. Faklaris *et al.*, 'Detection of Single Photoluminescent Diamond Nanoparticles in Cells and Study of the Internalization Pathway', *Small*, vol. 4, no. 12, pp. 2236–2239, Dec. 2008, doi: 10.1002/smll.200800655.
[144] S. Claveau, J. R. Bertrand, and F. Treussart, 'Fluorescent nanodiamond applications for cellular process sensing and cell tracking', *Micromachines*, vol. 9, no. 5. MDPI AG, May 18, 2018. doi: 10.3390/mi9050247.
[145] A. Alhaddad *et al.*, 'Influence of the Internalization Pathway on the Efficacy of siRNA Delivery by Cationic Fluorescent Nanodiamonds in the Ewing Sarcoma Cell Model', *PLoS One*, vol. 7, no. 12, p. e52207, Dec. 2012, doi: 10.1371/journal.pone.0052207.
[146] M.-F. Weng, B.-J. Chang, S.-Y. Chiang, N.-S. Wang, and H. Niu, 'Cellular uptake and phototoxicity of surface-modified fluorescent nanodiamonds', *Diam Relat Mater*, vol. 22, pp. 96–104, Feb. 2012, doi: 10.1016/j.diamond.2011.12.035.
[147] B. Zhang *et al.*, 'Anchored but not internalized: shape dependent endocytosis of nanodiamond', *Sci Rep*, vol. 7, no. 1, p. 46462, Apr. 2017, doi: 10.1038/srep46462.
[148] W. Pabst and E. Gregorová, 'Characterization of particles and particle systems', 2007.
[149] Henk G. Merkus, *Particle Size Measurements*. Springer, 2009.
[150] X. Zhang *et al.*, 'PEGylation and polyPEGylation of nanodiamond', *Polymer (Guildf)*, vol. 53, no. 15, pp. 3178–3184, Jul. 2012, doi: 10.1016/j.polymer.2012.05.029.
[151] O. Haeberlé, 'Focusing of light through a stratified medium: a practical approach for computing microscope point spread functions', *Opt Commun*, vol. 235, no. 1–3, pp. 1–10, May 2004, doi: 10.1016/j.optcom.2004.02.068.
[152] L. Novotny, R. D. Grober, and K. Karrai, 'Reflected image of a strongly focused spot', *Opt Lett*, vol. 26, no. 11, p. 789, Jun. 2001, doi: 10.1364/OL.26.000789.
[153] 'Standard Guide for Measurement of Particle Size Distribution of Nanomaterials in Suspension by Nanoparticle Tracking Analysis (NTA)', 2018.
[154] R. Schirhagl, K. Chang, M. Loretz, and C. L. Degen, 'Nitrogen-Vacancy Centers in Diamond: Nanoscale Sensors for Physics and Biology', *Annu Rev Phys Chem*, vol. 65, no. 1, pp. 83–105, Apr. 2014, doi: 10.1146/annurev-physchem-040513-103659.
[155] H.-S. Jung, K.-J. Cho, S.-J. Ryu, Y. Takagi, P. A. Roche, and K. C. Neuman, 'Biocompatible Fluorescent Nanodiamonds as Multifunctional Optical Probes for Latent Fingerprint Detection', *ACS Appl Mater Interfaces*, vol. 12, no. 5, pp. 6641–6650, Feb. 2020, doi: 10.1021/acsami.9b19245.
[156] V. Kestens, V. Bozatzidis, P.-J. De Temmerman, Y. Ramaye, and G. Roebben, 'Validation of a particle tracking analysis method for the size determination of nano- and microparticles', *Journal of Nanoparticle Research*, vol. 19, no. 8, p. 271, Aug. 2017, doi: 10.1007/s11051-017-3966-8.

[157] A. D. Kashkanova, M. Blessing, A. Gemeinhardt, D. Soulat, and V. Sandoghdar, ‘Precision size and refractive index analysis of weakly scattering nanoparticles in polydispersions’, *Nat Methods*, vol. 19, no. 5, pp. 586–593, May 2022, doi: 10.1038/s41592-022-01460-z.
[158] U. Ortiz-Orruño, R. Quidant, N. F. van Hulst, M. Liebel, and J. Ortega Arroyo, ‘Simultaneous Sizing and Refractive Index Analysis of Heterogeneous Nanoparticle Suspensions’, *ACS Nano*, vol. 17, no. 1, pp. 221–229, Jan. 2023, doi: 10.1021/acsnano.2c06883.
[159] O. Shenderova *et al.*, ‘Commercial quantities of ultrasmall fluorescent nanodiamonds containing color centers’, Z. U. Hasan, P. R. Hemmer, H. Lee, and A. L. Migdall, Eds., Feb. 2017, p. 1011803. doi: 10.1117/12.2256800.
[160] K. Žambochová, J.-S. Park, I.-B. Lee, S.-C. Hong, and M. Cho, ‘Diffusion dynamics of fluorescent nano-diamonds in living cells detected by fluorescence-combined iSCAT system’, in *IBS conference on Advanced Optical Imaging*, Seoul, Jun. 2019.
[161] L. Gardini, M. Capitanio, and F. S. Pavone, ‘3D tracking of single nanoparticles and quantum dots in living cells by out-of-focus imaging with diffraction pattern recognition’, *Sci Rep*, vol. 5, no. 1, p. 16088, Nov. 2015, doi: 10.1038/srep16088.
[162] K. Kim and J. Guck, ‘The Relative Densities of Cytoplasm and Nuclear Compartments Are Robust against Strong Perturbation’, *Biophys J*, vol. 119, no. 10, pp. 1946–1957, Nov. 2020, doi: 10.1016/j.bpj.2020.08.044.